UNIVERSITY OF CALIFORNIA
RIVERSIDE

Electric Field, Strain, Magnetic Proximity Effect in Two-Dimensional Heterostructures: A Theoretical Study

A Dissertation submitted in partial satisfaction
of the requirements for the degree of

Doctor of Philosophy

in

Electrical Engineering

by

Shanshan Su

June 2017

Dissertation Committee:

Dr. Roger K. Lake, Chairperson
Dr. Alexander Balandin
Dr. Jianlin Liu

The Dissertation of Shanshan Su is approved:

Committee Chairperson

University of California, Riverside

Acknowledgments

I thank my advisor, Professor Roger K. Lake, for giving me the opportunity to work for him and teaching me so much about device modelling and scientific writing. As a member in Dr. Lake's group, I have a lot of chances to discuss research with him, and can always get support from him. I acknowledge support and guidance from Prof. Alexander Balandin, Prof. Mihri Ozkan, Prof. Jing Shi and Prof. Nathaniel Gabor for allowing me to collaborate with their respective groups, valuable discussions on our collaborative research projects.

I am grateful for the opportunity to collaborate and discuss research with Dr. Gen Yin, Dr. Mahesh Neupane, Dr. Darshana Wickramaratne, Dr. Yafis Barlas, Dr. Supeng Ge, Dr. Junxue Li, Dr. Zafer Mutlu, Dr. Yu Chai, Ms. Fatemeh Barati, Mr. Max Grossnickle. A special thanks to the members of the LAboratory for Terascale and Terahertz Electronics (LATTE) for their advice, support and many informal discussions during my Ph.D. life.

On the personal side I would like to thank my family for their continuous support over the past five years. To my parents, Ms. Xuerong Zhang and Dr. Fa Su, I am thankful for their guidance and support of my education throughout these years. With their support, I can finally overcome the difficulties and the frustrated days.

The text of this dissertation, in part or in full, is a reprint of the material as it appears in the following journals:

- Journal Chemical Physics [1]. Reprinted with permission from [1]. ©[2017]. American Institute of Physics

- Physical Review B [2]. Reprinted with permission from [2]. ©[2017]. American Physical Society

The co-author Roger K. Lake, listed in the above publications directed and supervised the research which forms the basis for this dissertation. The remaining co-authors listed provided technical expertise and support as collaborators. This work is supported as part of the Spins and Heat in Nanoscale Electronic Systems(SHINES) an Energy Frontier Research Center funded by the U.S. Department of Energy, Office of Science, Basic Energy Sciences under Award DE-SC0012670, and the National Science Foundation EFRI-1433395. Ab-initio calculations were supported by FAME, one of the six centers of STARnet, a Semiconductor Research Corporation program sponsored by MARCO and DARPA and used the Extreme Science and Engineering Discovery Environment (XSEDE), which is supported by the National Science Foundation Grant No. ACI-1053575.

To my parents for all the support.

ABSTRACT OF THE DISSERTATION

Electric Field, Strain, Magnetic Proximity Effect in Two-Dimensional Heterostructures: A Theoretical Study

by

Shanshan Su

Doctor of Philosophy, Graduate Program in Electrical Engineering
University of California, Riverside, June 2017
Dr. Roger K. Lake, Chairperson

Due to the self-passivated and dangling bond free surfaces of two-dimensional (2D), a variety of vertical heterostructures are designed with a wide range of bandgap and material properties. We use first-principles simulations to investigate the electric field, strain and magnetic proximity effect in 2D heterostructures.

Both monolayer WSe_2/monolayer $MoSe_2$ and bilayer WSe_2/monolayer $MoSe_2$ form intrinsic type II heterojunction. As the electric field is ramped from negative to positive, the band structure of both structures shows a transition from indirect to direct bandgap. The bilayer WSe_2/monolayer $MoSe_2$ even shows a transition from type I heterojunction to type II heterojunction under negative electric field.

$HfSe_2/SnS_2$ is indirect bandgap heterostructure and shows a coherent superposition of the conduction band wavefunctions of the individual layers at conduction band minimum (CBM). The CBM without electric field is weighted towards SnS_2 layer, a vertical electric field of 0.2 V/Å, pointing from $HfSe_2$ to SnS_2 layer, reverses the weights of the conduction band wavefunction. Placing graphene on $HfSe_2/SnS_2$ results in significant

charge transfer from graphene to the heterostructure, and the trilayer system forms a negative Schottky barrier contact for electron injection from graphene into $HfSe_2/SnS_2$. The contact resistance of graphene on $HfSe_2/SnS_2$ calculated from a tunneling Hamiltonian indicates an excellent low-resistance contact.

$PtSe_2/SnS_2$ forms a Mexican hat in the valence bands around $\mathbf{\Gamma}$. The in-plane biaxial strain can significantly tune the band structures of $PtSe_2/SnS_2$. Under tensile strain the height of Mexican hat is more than six times of the value without strain; while under compressive strain, a semiconducting to metallic transition is observed. Graphene in contact with SnS_2 layer of $PtSe_2/SnS_2$ heterostructure forms negative Schottky barrier.

Recent experiments demonstrating proximity induced ferromagnetism in graphene motivate this study of commensurate EuO/graphene/EuO heterostructures. Using insights from lattice symmetries of EuO/graphene/EuO heterostructures, we develop a model Hamiltonian that includes proximity induced exchange splitting, spin-orbit coupling, and intervalley interactions with parameters fitted to ab initio calculations. The intervalley interaction opens up a trivial gap preventing the system from crossing into a non-trivial state. The model Hamiltonian is analyzed to determine the conditions under which the heterostructures can exhibit topologically non-trivial bands.

Contents

List of Figures

List of Tables

Chapter 1

Introduction and Goals

The down-scaling of metal oxide semiconductor field effect transistors (MOSFETs) has followed the Moore's law, making possible the development of modern electronic devices, such as smart-phones and laptops with more functions. After years of development, we are approaching the limit of Moore's law. Many projections have suggested that the ultimate limit of silicon MOSFETs is the 5 nm channel length. [3, 4] There is world-wide effort to identify materials that could compliment Si and extend Moore's law. This dissertation investigates the properties of some of the two-dimensional (2D) materials, their heterostructures, and contacts.

1.1 Zoo of 2D Materials

Since the discovery of graphene [2, 5], the family of 2D materials has grown to include hexagon-boron nitride (hBN) [6], black-phosphorous [7], transition-metal dichalcogenides (TMDCs) [8], III-VI materials [9], transition-metal carbides (MXenes) [10], bismuth

and antimony selenides and tellurides (topological insulators) [11, 12] and non-transition-element chalcogenides, such as SnS_2 [1], etc. All schematic structures for different 2D materials are shown in Fig. 1.1. 2D materials have covalent bonds in-plane to connect the atoms, while van der Waals (vdW) forces connect layers in the direction perpendicular to material plane. Due to the weak bonding between layers, individual layers can be mechanically exfoliated. Furthermore, the surfaces of each layer are self-passivated, since the in-plane bonds account for all of the valence electrons. The chemically inert surfaces free of dangling bonds make the fabrication of atomiclly thin devices possible.

Both graphene and hBN [6] are single-layer materials with hexagonal in-plane atomic arrangement. Graphene is composed of carbon atoms only, while hBN is composed of boron and nitrogen atoms as shown in Fig. 1.1. TMDCs consist of hexagonal-layers of transition-metal atoms (M) sandwiched between two layers of chalcogen atoms (X). The chemical formula can be expressed as MX_2. The chalcogen atoms are typically S, Se, and Te. The transition metal atom can be chosen from Ti, Zr, Hf, V, Nb, Ta, Mo, W, Tc, Re, Pd, Pt and etc. The stacking arrangement of the TMDC crystals can be further categorized as 1T, 2H, 3R phases. Non-transition-element chalcogenides with formula AX_2 crystallize in hexagonal closed packed structure with $P\bar{3}m1$ symmetry. The X, similar to TMDCs, refers to the chalcogen atoms, while A refers to non-transition-element, such as Sn, Pb. Each unit cell contains three atoms, and extends over only one sandwich layer. [13] The stacking arrangement of this type of materials is 1T which has the same shape of the 1T phase of TMDCs. All listed 2D materials have different electronic properties, such as metallic, semiconducting, or wide bandgap insulators.

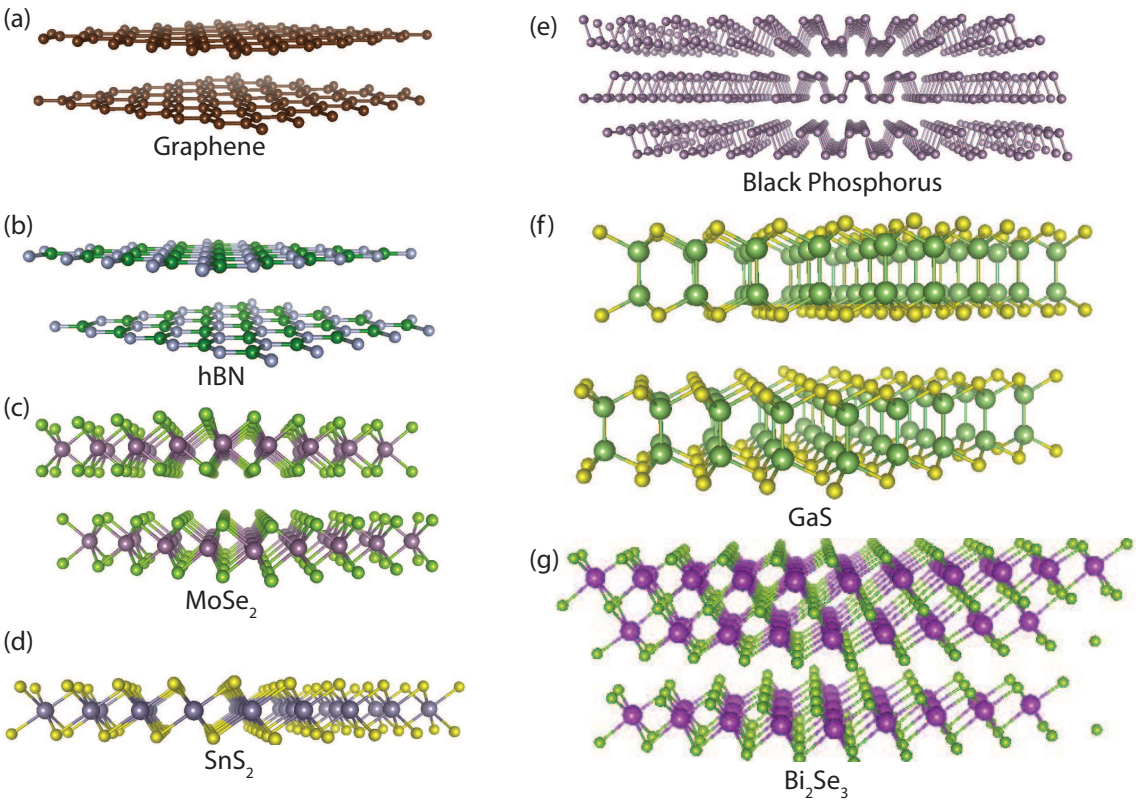

Figure 1.1: The schematic structure of typical 2D materials. (a) Graphene; (b) hBN; (c) $MoSe_2$ (2H phase); (d) SnS_2 (1T phase); (e) black phosphorus; (f) GaS; (g) Bi_2Se_3.

1.2 2D Heterostructures

Due to the excellent surface properties of 2D materials, different types of 2D materials can be easily stacked together. Different properties from different 2D materials can be induced by proximity if they are stacked together. Research has focused on 2D heterostructures experimentally and theoretically, such as MoS_2/SnS_2 [14], MoS_2/black phosphorus [15], and $HfSe_2/SnS_2$ [1]. The types of heterostructures can be categorized in the way they are stacked as vertical or lateral heterostructures. Examples of vertical and lateral heterostructures are shown in Fig. 1.2. This dissertation focuses on the study of different vertical heterostructures.

There have been some interesting observations made on vertical heterostructure. Graphene on hBN leads to the formation of the secondary Dirac points [16–21]; TMDCs can induce a proximity spin-orbit coupling in graphene [16, 22, 23]; graphene on $HfSe_2/SnS_2$ forms a negative Schottky barrier [1], etc.

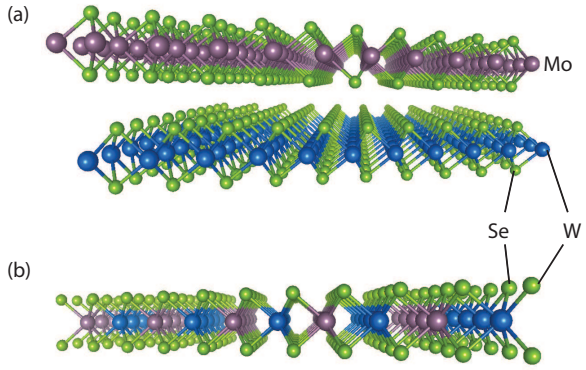

Figure 1.2: The structures of (a) vertical ($MoSe_2/WSe_2$) and (b) lateral ($MoSe_2/WSe_2$) heterostructures.

In this dissertation, I primarily focus on the study of the electrical field, strain and magnetic proximity effect in the 2D heterostructures. The rest of this dissertation is organized as follows. Chapter 2 presents a background of density functional theory (DFT), the LDA+U method and the hybrid functional (HSE) used in this study. Chapter 3 discusses the electric field effect on the electronic structure of a $MoSe_2/WSe_2$ heterostructure. Chapter 4 discusses the electronic properties of $HfSe_2/SnS_2$ under an electric field, as well as the negative Schottky barrier of graphene/$HfSe_2/SnS_2$. More band structures related to this heterostructure are shown in Appendix A. Chapter 5 focuses on the analysis of $PtSe_2/SnS_2$ heterostructures, and studies the strain effect and the electric field effect in the heterostructures, we also discuss the electronic structures of $PtSe_2/SnS_2$ with graphene contacts. Chapter 6 extends our 2D heterostructure study to the field of magnetic proximity effect. By sandwiching graphene with magnetic layers, the spin-orbit splitting is induced into graphene. In the last, Chapter 7 summarizes key findings of this dissertation.

Chapter 2

Theoretical Methods

In this chapter, we focus on the introduction of the methods used for the calculations. The first section is the general introduction to density functional theory (DFT) and van der Waals correction of DFT. The second section of this chapter focuses on the introduction of LDA+U method. The hybrid functional is introduced in the last section. The differences among the regular DFT, LDA+U and the hybrid functional are mentioned along with the introductions.

DFT is one of the widely used computational quantum mechanical modelling methods in condensed matter physics, chemistry and materials science. DFT has been applied to study electronic, mechanical and magnetic properties of complex material systems. The DFT computation method is based on the quantum mechanical modelling of many-electron systems. For a system of electrons and nuclei, the Hamiltonian is written as:

$$H = T + V_{ext} + V_{int} + E_{nn} \tag{2.1}$$

where T is the electronic kinetic energy, V_{ext} is the potential due to the electron-nuclei interactions, V_{int} is the potential due to electron-electron interactions, and E_{nn} refers to the interaction between nuclei.

The basis of DFT is the Hohenberg-Kohn (HK) theorems. [24] From the first HK theorem, the ground-state of many-electron systems can be determined by the electron density of the system. The second HK theory gives the total ground-state energy. The total energy functional can be written as:

$$E[n] = T[n] + \int d^3r V_{ext}(r)n(r) + E_{int}[n] + E_{nn} \tag{2.2}$$

T[n] is the kinetic energy, E_{int} is the energy between electrons, V_{ext} is the external potential acting on the electrons from nuclei.

From the HK theorem, an approximation method is developed for treating an inhomogeneous system of interaction electrons. This method is called Kohn-Sham method. [25] Within the framework of Kohn-Sham DFT, the problem transfers from an intractable many-body problem to a tractable problem of non-interacting electrons moving in an effective potential. The effective Kohn-Sham Hamiltonian of the non-interacting particles is:

$$V_{KS}(r) = V_{ext}(r) + V_H(r) + V_{XC}(r) \tag{2.3}$$

V_H is the Hartree potential. V_{XC} is the exchange-correlation potential which includes the electron-electron interaction beyond the Hartree potential.

The exact functional for the exchange-correlation term is unknown. Two common approaches to approximate exchange-correlation potential are the local density approximation (LDA) and the generalized gradient approximation (GGA). Both LDA and GGA can give accurate description the properties of materials which resemble a homogeneous electron gas. At the same time, both approximations are unable to describe van der Waals interactions resulting from dynamical correlations between fluctuating charge distributions correctly. A practical way to solve this problem is to add a correction term to the conventional Kohn-Sham DFT energy. The new expression of the energy can be written as [26]:

$$E_{DFT-vdW} = E_{KS} + E_{vdW}, \tag{2.4}$$

where E_{KS} is the original energy from Kohn-Sham equation; E_{vdW} is the correction term which is computed by using DFT-D2 approximation method [26] as:

$$E_{vdW} = -s_6 \sum_{i=1}^{N_{at}-1} \sum_{j=i+1}^{N_{at}} \frac{C_6^{ij}}{R_{ij}^6} f_{dmp}(R_{ij}), \tag{2.5}$$

N_{at} is the number of atoms in the system, C_6^{ij} denotes the dispersion coefficient for atom pair i, j, s_6 is a global scaling factor which is 0.25 in our calculations, and R_{ij} is an interatomic distance. f_{dmp} is the damping function whose role is to scale the force field such that the contributions from interactions within typical bonding distances are minimized.

There are two types of problems of LDA and GGA calculations. The first problem is the LDA and GGA calculations fail to describe the electronic structure of the material where some the ions contain partly filled valence d or f shells. As shown in Ref. [27], many

transition metal oxides, such as MnO and NiO, have been predicted by LDA and GGA calculations to have metallic ground state instead of experimentally observed insulating state. The origin of this failure is associated with an inadequante description of the strong Coulomb repulsion between $3d$ or $4f$ electrons in the metal ions. [28] To fix the problem, the effective Hubbard U is introduced to characterize on-site Coulomb repulsion, and this method is called LDA+U. [29] The U correction to the energy can be expressed as [29]:

$$E_{LDA/GGA+U} = E_{LDA/GGA} + \frac{U-J}{2}\sum_{\sigma}(n_{m,\sigma} - n_{m,\sigma}^2). \tag{2.6}$$

$n_{m,\sigma}$ is the occupation number of the mth d or f state. m in the equation represents the projections of the orbital momentum; σ is the spin. The total number of electron can be expressed as $\sum_m n_{m,\sigma}$. U and J are the spherically averaged matrix elements of the screened Coulomb electron-electron interaction. The LDA+U method can be understood as adding a penalty functional to the original LDA and GGA energy expression. In Chapter 6, we used this LDA+U functional to describe the electronic structure of EuO.

The second problem of LDA and GGA calculations is that the bandgap of semiconductor or insulator is always underestimated. For example, the bandgap of bilayer MoS_2 is 1.64 eV [30] from experimental studies. The GGA calculations predict the bilayer bandgap of MoS_2 to be 1.25 eV [30]. To solve this problem, the hybrid functional named the Heyd-Scuseria-Ernzerhof (HSE) functional is used. [31] The basic idea for HSE is to mix the GGA implemented by a Perdew-Burke and Ernzerhof (PBE) [32–34] with an orbital dependent Hartree-Fock calculation. The Hartree-Fock calculation provides the short range Fock exchange; while the GGA calculation preserves the accuracy while avoiding the cost

and pathologies [35] of long-range Fock exchange. The method used to perform this mix is called the error function screened Coulomb potential, which can be expressed as:

$$E_{xc}^{PBEh} = aE_x^{HF,SR}(\mu) + (1-a)E_x^{PBE,SR}(\mu) + E_x^{PBE,LR}(\mu) + E_c^{PBE}, \tag{2.7}$$

where a is the mixing parameter and each of the terms above is related to an adjustable parameter, a common value used for a is 0.25. μ is the range-separation at which the short-range interactions become negligible. When we adjust μ to 0, it reduces to the PBE functional. SR and LR are the labels representing short-ranged and long-ranged part of the electron-electron interaction. $E_x^{HF,SR}$ is the short range Hartree-Fock exact exchange functional, $E_x^{PBE,SR}$ and $E_x^{PBE,LR}$ are the short and long range components of PBE exchange functional, E_c^{PBE} is the PBE correlation functional. The calculated bandgap for bilayer MoS_2 using the HSE functional mentioned above is 1.64 eV which is in very good agreement with the experimental result. [30] Although the HSE functional provides more reliable electronic band structures, it is also more expensive in terms of computation. We take the trade-off between accuracy and computational resources by using PBE-DFT method to show the influence of both electric field and mechanical strain, while using HSE give the accurate prediction of electronic structure.

Chapter 3

Electric Field Effect in Transition Metal Dichalcogenides

3.1 Introduction

Layered TMDCs have a chemical formula, MX_2, where M is transition metal (e.g. Ti, Hf, Mo), and X is the chalcogen atom (e.g. S, Se, and Te). Each layer of TMDCs is composed of one layer of transition metal atoms sandwiched by two layers of chalcogen atoms. TMDCs offer a broad range of electronic properties. [16] Most of TiX_2, ZrX_2, MoX_2, WX_2 combinations show either insulating or semiconducting electronic properties; while VX_2, NbX_2 and TaX_2 are most likely metallic or semi-metallic. The difference in electronic structure is due to the progressive filling of the non-bonding d bands of the transition metal atoms. [16]

TMDCs are usually found in three polytypes: 1T, 2H and 3R. The numbers in the polytype names indicate the number of layers in the unit cell, and the capital letters refer to the symmetry (e.g. T: trigonal; H: hexagonal; R: rhombohedral). [36] The schematic view of these polytypes are shown in Fig. 3.1. TiX_2, ZrX_2, HfX_2, and VX_2 all belong to 1T phase TMDCs. As shown in Fig. 3.1(a), metal atoms in the 1T structure are sitting right on top of the metal atoms, and are sandwiched by chalcogen atoms in an octahedral coordination. This 1T polytype belongs to the $P\bar{3}m1$ symmorphic space group. [36] The MoX_2 family and WS_2, WSe_2 all fall into 2H polytype. 2H polytypes can have different stacking symmetries: $2H_a$ (M atoms sit right on top of each other, the X atoms from the two layers sit on the opposite side of M atoms), $2H_b$ (there is a sliding of the in-plane distance between X and M atoms between the two layers) and $2H_c$ (as shown in Fig. 3.1). Among three phases under category of 2H, we focus on $2H_c$ since this is the polytype of MoX_2 family. $2H_c$ belongs to nonsymmorphic hexagonal space group $P6_3/mmc$. [36] The primitive unit cell is as shown in Fig. 3.1 with 6 atoms. Unlike 1T, the symmetry of 2H phase material depends on the number of layers, e.g. odd or even. MoS_2 naturally is 2H phase, however, under high pressure and temperature, MoS_2 becomes 3R phase. [36] 3R phase, as shown in Fig. 3.1, is found only in bulk compounds and relaxed to the 2H phase upon mild heating. [37]

In this section, We will focus only on semiconducting TMDCs. Semiconducting TMDCs have shown promising electronic, [38–43] optical, [43] mechanical [44] and spintronic [45] properties. Due to the weak interlayer coupling, it is very easy to mechanically exfoliate monolayer and few-layer crystals.

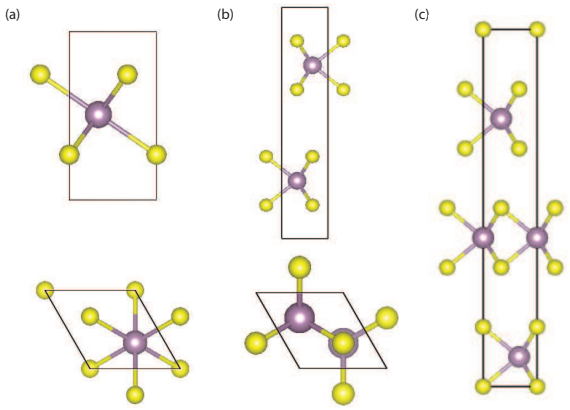

Figure 3.1: The schematic structures of three polytypes of TMDCs. (a) Side and top views of 1T structure; (b) Side and top views of 2H structure; (c) 3R structure.

Monolayer TMDCs like MoS_2, $MoSe_2$ and WSe_2 have direct bandgaps, while the multilayers have indirect bandgaps. Unlike graphene, semiconducting TMDCs with finite bandgaps are promising for the applications in electronic and photonic devices with an on/off ratio exceeding 10^8. [46] Devices built from TMDCs can extend Si electronics into the area of flexible electronics, optoelectronics, and spintronics. The TMDCs can also be integrated onto a conventional Si CMOS chip to provide added functionality and performance.

In this chapter, we studied $WSe_2/MoSe_2$ heterostructures from two different aspects, the thickness dependence and the influence of electric field. Section 3.3.1 discusses the changes of the electronic structures of monolayer $MoSe_2$ with monolayer WSe_2 under different electric fields. A different thickness of the $WSe_2/MoSe_2$ heterostructure (bilayer WSe_2 with monolayer $MoSe_2$) is studied in Section 3.3.2.

3.2 Methods

The band dispersions of TMDCs heterostructures are calculated using the Vienna ab initio simulation package (VASP) [47–49] in the projected-augmented-wave method [50]. The generalized gradient approximation (GGA) of the Perdew-Burke-Ernzerhof (PBE) form [32–34] is used for the exchange correlation energy. The van der Waals interaction between the layers is taken into consideration by using DFT-D2 method of Grimme [51]. The energy cutoff of the plane wave basis is 500 eV for all calculations. All the calculations in this chapter are considered with spin-orbit coupling (SOC) due to the heavy metal element in $WSe_2/MoSe_2$. We also used Heyd-Scuseria-Ernzerhof (HSE) functional [31] to give a more accurate prediction of the bandgaps and electronic structure of $WSe_2/MoSe_2$. The HSE calculations incorporate 25% short-range Hartree-Fock exchange. The screening parameter μ is set to 0.2 $Å^{-1}$. During all structural relaxations, the convergence tolerance on the Hellmann-Feynman forces is less than 0.01 eV/Å. An $8 \times 8 \times 1$ Monkhorst-Pack k-point mesh is used for the 2D films. A vacuum buffer spacing 20 Å is used for all heterostructures calculations.

3.3 Electric Field Effect in $WSe_2/MoSe_2$

The lattice constant of $MoSe_2$ is 3.3247 Å, and the lattice constant of WSe_2 is 3.326 Å. The lattice mismatch between the two materials is less than 1%. The lattice constant of $WSe_2/MoSe_2$ heterostructure is 3.325 Å. Though there are several possible stacking structures, previous studies suggest the most energy-stable structure is the 2H structure [52].

3.3.1 Monolayer WSe_2 with Monolayer $MoSe_2$

The 2H stacking of two monolayers is shown in Fig. 3.2. The top layer is $MoSe_2$ and the bottom layer is WSe_2 The electric field is applied perpendicular to the bilayer plane, and the positive direction of the field is pointing from WSe_2 layer to $MoSe_2$ layer as shown in Fig. 3.2.

The band structure of $MoSe_2/WSe_2$ calculated with SOC by using PBE functional is shown in Fig. 3.3. The heterostructure has direct bandgap which is 1.0173 eV. The conduction band minimum (CBM) is localized on $MoSe_2$ layer with an orbital composition from the *d* orbital of Mo, while the valence band maximum (VBM) is localized on WSe_2 layer with an orbital composition from the *d* orbital of W. Therefore, the monolayer/monolayer heterostructure forms intrinsic type II heterojunction. Both CBM and VBM are at **K**. The SOC splitting of WSe_2 of valence band at **K** is 485.1 meV, while the splitting for the conduction band at **K** is 37.9 meV. The splitting gap of $MoSe_2$ of valence band at **K** is 204.7 meV, and the conduction band splitting is 20.4 meV. The SOC splitting and

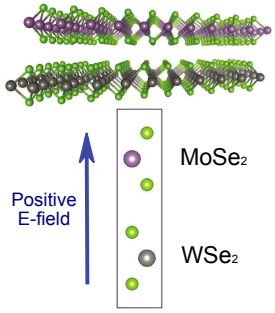

Figure 3.2: The structure of heterostructure. The top figure is the superlattice of the heterostructure. The bottom figure shows the side view of the monolayer WSe_2/ monolayer $MoSe_2$ heterostructure. The top layer is $MoSe_2$ and bottom layer is WSe_2. The arrow on the left side refers the positive direction of the electric field. The vacuum space is not shown in the figure.

bandgap for each layer as shown in Table. 3.1 remain the same as the one for the monolayer TMDCs. [53, 54] Therefore, we know that the SOC splitting gaps are not affected by the interlayer coupling between WSe_2 and $MoSe_2$. The conduction offset between the two layers is 218.0 meV, while the valence offset between the two layers is 299.7 meV. The bandgap of $MoSe_2$ in the heterostructure is obtained as 1.317 eV, while the bandgap of WSe_2 is obtained as 1.235 eV. Our calculated bandgaps are consistent with the previous calculated results [55] for the monolayer TMDCs with SOC .

The bandgap and band offsets of $WSe_2/MoSe_2$ under different electric fields are listed in the Table 3.1. A plot of the resulting bandgap versus the electric field is shown in Fig. 3.4 in blue. The trend of bandgaps shows a clear asymmetric shape. Under a positive electric field, the bandgap of the heterostructure decreases monotonically. The bandgap stays direct at **K** point, which can be found from Table 3.1. The band offsets in conduction and valence bands between WSe_2 and $MoSe_2$ increase with each increment of the positive electric field. Together with Fig. 3.5, it is clear that the closing of the gap is the result of the comparative band shift of WSe_2 and $MoSe_2$. Due to the shift of the bands, the $\mathbf{\Gamma}$ and $\mathbf{\Lambda}$ points share the same composition as **K** point for valence and conduction bands under a positive electric field. From Table 3.1, it is also clear that the SOC splitting at **K** remain the same throughout all applied electric fields.

A direct bandgap to indirect bandgap transition can be observed as shown in Table 3.1. Until -0.1 eV/Å, the bandgap stays direct; when the electric field reaches -0.2 eV/Å, the bandgap becomes indirect. Table 3.1 shows the band offsets between $MoSe_2$ and WSe_2 in both conduction bands and valence bands with a negative sign when the electric

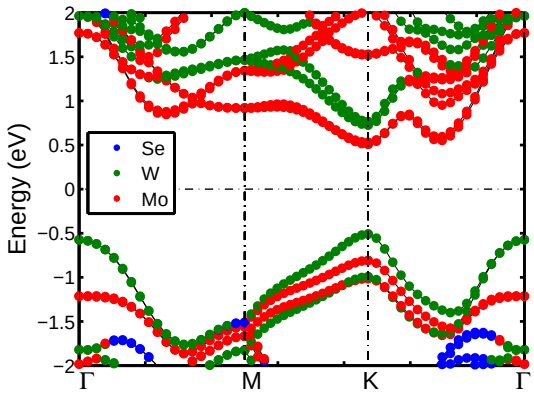

Figure 3.3: SOC band structure of $MoSe_2/WSe_2$ with ionic composition.

field reaches -0.2 eV/Å. Therefore, together with the direct bandgap to indirect bandgap transition, there is a band edge switching between $MoSe_2$ and WSe_2. After passing -0.2 eV/Å, the CBM is localized on WSe_2, and VBM is localized on $MoSe_2$. From both the Table 3.1 and Fig. 3.4, a saturation of the bandgap can be found at -0.2 eV/Å. Similar to the positive electric field, the SOC splitting gaps for both $MoSe_2$ and WSe_2 remain unchanged throughout the negative electric field. The gap between $\mathbf{\Lambda}$ and $\mathbf{K}$ first increases, before decreasing to a very low value. The $\Delta E_{\Lambda-K}$ is about the same level of the conduction band SOC gap level. The same trend also happens to the gap between $\mathbf{\Gamma}$ and $\mathbf{K}$.

The effective masses of the heterostructure under different electric fields are listed in Table 3.2. The masses remain almost the same from 0 eV/Å to 0.4 eV/Å. Under -0.2 eV/Å, the effective masses at $\mathbf{K}$ remain the same as the values under 0 electric field. This is due to the constant of the band compositions of the heterostructure as shown in Fig. 3.5. As expected, under -0.4 eV/Å, the effective masses change a lot at $\mathbf{K}$, the conduction

Table 3.1: The gaps of heterostructure under positive electric field. $\mathcal{E}$ refers to the electric field applied to the heterostructure, the unit is eV/Å. E_G is the bandgap of the heterostructure. $\Delta E^{cond}_{\Lambda-K}$ shows the gap between $\mathbf{\Lambda}$ and $\mathbf{K}$ valley at conduction band when CBM is not at $\mathbf{K}$. $\Delta E^{val}_{\Gamma-K}$ shows the gap between $\mathbf{\Gamma}$ and $\mathbf{K}$ valley at valence band when VBM is not at $\mathbf{K}$. K^{cond}_{Mo} is the SOC splitting gap of $MoSe_2$ conduction band at K valley, K^{val}_{Mo} is the SOC splitting gap of $MoSe_2$ valence band at K valley. K^{cond}_{W} is the SOC splitting gap of WSe_2 conduction band at K valley, K^{val}_{W} is the SOC splitting gap of WSe_2 valence band at K valley. ΔE^{cond} is the band offset between WSe_2 and $MoSe_2$ in the conduction bands, ΔE^{val} is the band offset between WSe_2 and $MoSe_2$ in the valence bands. ΔE^{cond} and ΔE^{val} are positive when CBM and VBM of WSe_2 are above CBM and VBM of $MoSe_2$ in energy; otherwise, the sign of the two gaps turns to negative. The values are all in units of meV.

$\mathcal{E}$	E_G	$\Delta E^{cond}_{\Lambda-K}$	$\Delta E^{val}_{\Gamma-K}$	K^{cond}_{Mo}	K^{val}_{Mo}	K^{cond}_{W}	K^{val}_{W}	ΔE^{cond}	ΔE^{val}
0.0	1017.3 ($\mathbf{K}-\mathbf{K}$)	43.4	65.3	20.4	204.7	37.9	485.1	218	299.7
0.1	933.0 ($\mathbf{K}-\mathbf{K}$)	73.0	94.9	20.5	215.6	38.2	495.7	302.9	372.2
0.2	848.8 ($\mathbf{K}-\mathbf{K}$)	94.8	120.7	20.5	144.1	38.6	424.1	387.5	515.5
0.3	765.0 ($\mathbf{K}-\mathbf{K}$)	110.1	142.9	20.5	165.9	39.2	445.8	471.5	588.9
0.4	686.0 ($\mathbf{K}-\mathbf{K}$)	120.0	161.0	20.5	173.5	39.8	453.2	550.6	660.1
0.5	599.6 ($\mathbf{K}-\mathbf{K}$)	127.7	178.3	20.6	177.2	40.8	456.6	636.6	742.5
-0.1	1102 ($\mathbf{K}-\mathbf{K}$)	5.2	31.5	20.4	201	37.7	481.4	132.1	219.7
-0.2	1138.2 ($\mathbf{\Gamma}-\mathbf{\Lambda}$)	41.3	6.4	20.6	200.2	37.7	480.8	-41.3	-6.4
-0.3	1125.0 ($\mathbf{\Gamma}-\mathbf{\Lambda}$)	57.2	47.5	14.6	201.6	31.5	482.3	-99.8	-47.5
-0.4	1098.6 ($\mathbf{\Gamma}-\mathbf{\Lambda}$)	31.8	67.6	19.5	206.7	36.3	487.5	-127.2	-93.1
-0.5	1065.2 ($\mathbf{\Gamma}-\mathbf{\Lambda}$)	14.7	38.1	19.7	218.9	36.4	499.7	-225.1	-131.0
-0.6	1022.0 ($\mathbf{\Gamma}-\mathbf{\Lambda}$)	1	11.3	19.6	142.3	36.3	423.1	-294.8	-264.2

Table 3.2: The effective masses of heterostructure under different electric field. mT represents the transverse effective mass, and mL represents the longitudinal effective mass.

Electric field (eV/Å)	mL_K^{con} (m_0)	mT_K^{con} (m_0)	mL_K^{val} (m_0)	mT_K^{val} (m_0)	mL_Λ^{con} (m_0)	mT_Λ^{con} (m_0)	mL_Γ^{val} (m_0)	mT_Γ^{val} (m_0)
-0.4	0.399	0.399	0.588	0.588	0.502	0.614	1.324	1.335
-0.2	0.503	0.503	0.356	0.356	0.525	0.639	1.139	1.138
0.0	0.498	0.498	0.373	0.373	0.561	0.695	1.208	1.204
0.2	0.497	0.498	0.353	0.354	0.611	0.782	1.326	1.318
0.4	0.497	0.497	0.354	0.354	0.623	0.829	1.357	1.349

band at **K** changes to WSe_2, and the valence band edge changes to $MoSe_2$. The electron effective mass at **Λ** is increasing as a function of electric field.

To have a more accurate prediction of the bandgaps, HSE functional calculations are performed for the heterostructure. The HSE bandgaps under five different electric fields are listed in Table 3.3. The trend of HSE bandgap is shown in Fig. 3.6 in red. The HSE bandgap shows similar trend as the PBE results. The main difference between the two lines is the value of the gap. The HSE bandgap remains as direct until -0.2 eV/Å. The gap between **K** and **Λ**, **K** and **Γ** decreases as a function of the electric field monotonically. Fig.3.6 shows the comparison between the PBE band structure and the HSE band structure.

Table 3.3: The gaps of heterostructure under negative electric field. $\Delta E_{\Lambda-K}^{cond}$ shows the gap between **Λ** and **K** valley at conduction band when CBM is not at **K**. $\Delta E_{\Gamma-K}^{val}$ shows the gap between **Γ** and **K** valley at valence band when VBM is not at **K**.

Electric field (eV/Å)	E_G	K_G	$\Delta E_{\Lambda-K}^{cond}$	$\Delta E_{\Gamma-K}^{val}$
-0.4	1581.619 ($\mathbf{K}-\mathbf{\Lambda}$)	1587.4	5.7	8.3
-0.2	1519.289 ($\mathbf{K}-\mathbf{K}$)	1519.289	15.0	105.4
0.0	1327.550 ($\mathbf{K}-\mathbf{K}$)	1327.550	121.5	182.5
0.2	1135.322 ($\mathbf{K}-\mathbf{K}$)	1135.322	180.7	240.4
0.4	944.5 ($\mathbf{K}-\mathbf{K}$)	944.5	202.8	282.8

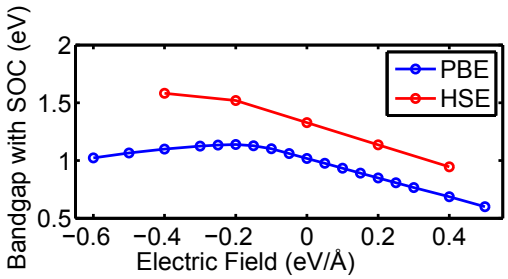

Figure 3.4: The bandgap changing as a function of the applied electric field. Blue line and red line correspond to PBE and HSE results, respectively.

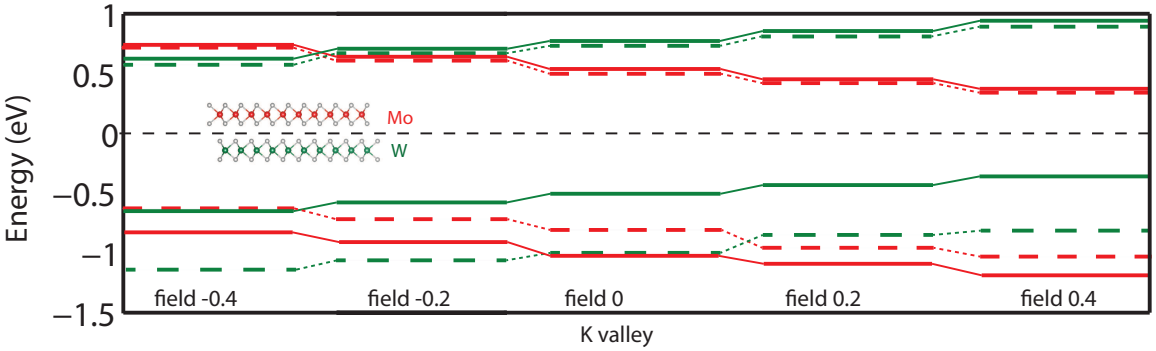

Figure 3.5: The band edges of WSe_2 and $MoSe_2$ under five different electric fields at **K** point. From left to right, it shows closing of gaps under positive electric field, while the bands are getting closer of the two materials under a negative electric field. The dash line in the figure represent the spin-down bands. Green lines are WSe_2, while red lines are $MoSe_2$.

The shape of the band structures for the two different calculation methods shows similar features.

3.3.2 Monolayer $MoSe_2$ with Bilayer WSe_2

In this part, we will study the monolayer $MoSe_2$/bilayer WSe_2 under electric fields. Given the results of monolayer/monolayer heterostructure, it is clear that the PBE results can show almost the same trend and band structure shape as HSE, therefore, in this section, we will calculate all results based on PBE only since we only care for the trend of band edges. The schematic view of the trilayer system is shown in Fig. 3.7. The stacking order of the trilayer system follows the 2H stacking.

The direction of the applied field is shown as an arrow in the Fig. 3.7. The bandgap as a function of the electric field is shown in Fig. 3.8. The corresponding band alignment under different electric fields is shown in Fig. 3.9. From Fig. 3.8, we can know that the trilayer system has indirect bandgap which is 0.94 eV. As show in Fig. 3.9(b), the CBM is localized on $MoSe_2$ at **K**, while the VBM is localized on WSe_2 at $\mathbf{\Gamma}$. Therefore, similar to the monolayer/monolayer heterostructure, the bilayer/monolayer forms intrinsic type II heterojunction.

Throughout negative electric fields, there is a clear difference between the bandgap and the gap at **K** in Fig. 3.8, which means that the bandgap of the trilayer system stays indirect. The band alignment of the trilayer heterostructure under -0.2 eV/Å is shown in Fig. 3.9(c). The CBM switches to WSe_2 layer under this configuration which means it

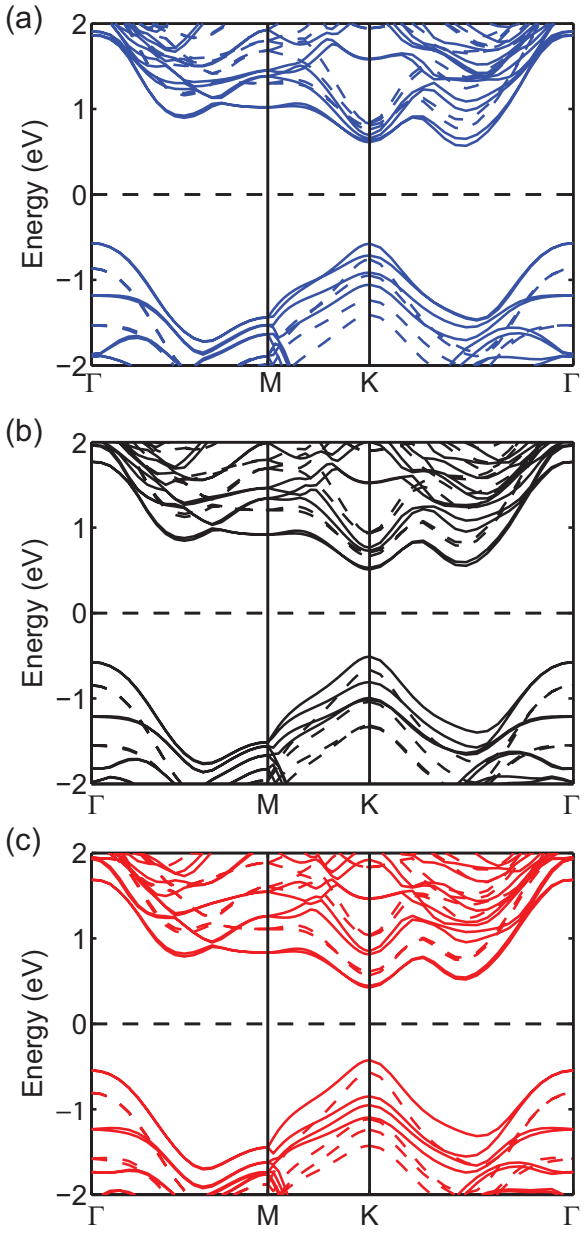

Figure 3.6: The band structures with SOC under different electric fields. (a)Band structure with -0.2 eV/Å; (b) band structure with no electric field; (c) band structure with 0.2eV/Å. The solid lines show the PBE results with SOC; while the dash lines show the results calculated by using HSE functional with SOC.

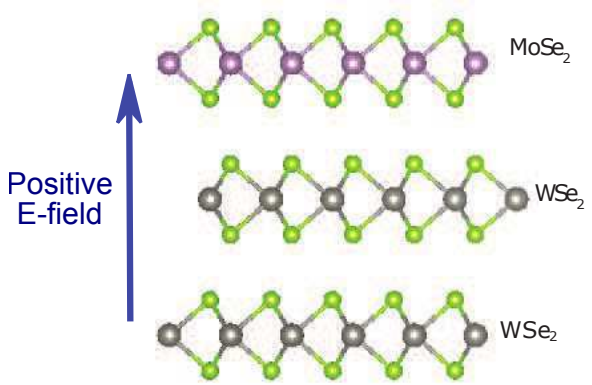

Figure 3.7: Schematic structure of heterostructure composed of monolayer $MoSe_2$ and bilayer WSe_2. The arrow on the left refers to the positive direction of applied electric field.

becomes type I heterojunction. This change of heterojunction type is different from the behavior of the monolayer/monolayer heterostructure.

The transition from indirect bandgap to direct bandgap of the trilayer system happens under 0.2 eV/Å. With a positive electric field larger than 0.2 eV/Å, the bandgap switches to direct with both CBM and VBM at **K** valley. The CBM and VBM remain localize on $MoSe_2$ and WSe_2 layer as the behavior of heterostructure under zero electric field. The bandgap decreases to be 0.73 eV under 0.2 eV/Å, and it will further decrease with larger positive electric field to 0.35 eV. In the same time, due to the comparative movement of band edges of the two materials, the band offsets between $MoSe_2$ and WSe_2 increase.

3.4 Conclusion

We have studied two different thicknesses of $WSe_2/MoSe_2$ heterostructure, monolayer WSe_2 with monolayer $MoSe_2$ and bilayer WSe_2 with monolayer $MoSe_2$, with spin-orbit

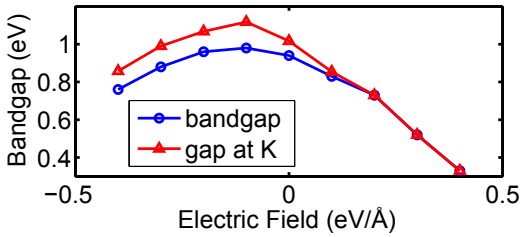

Figure 3.8: The bandgap and direct gap at **K** as a function of applied electric field. The unit of electric field is eV/Å. Blue line and dots represent the bandgap at each system. Red line and dots give the value of gap at **K** valley.

coupling by using fist principle calculations. Both heterostructures show intrinsic type-II band alignment with CBM at $MoSe_2$ and VBM at WSe_2 under zero electric field. The monolayer/monolayer heterostructure has direct bandgap, and remains as direct bandgap throughout all positive electric fields. A direct bandgap to indirect bandgap switching occurs under -0.2 eV/Å. Together with the bandgap transition, a band edge shift for both CBM and VBM also happens. Through out all applied electric fields, the heterostructure remains as type II heterojunction. The PBE functional results give the similar features as the HSE functional results.

The monolayer/bilayer heterostructure has indirect bandgap. The bandgap remains indirect through out all negative electric fields. A transition from indirect bandgap to direct bandgap happens at 0.2 eV/Å. Unlike monolayer/monolayer heterostructure, under -0.2 eV/Å, the heterostructure becomes type I heterojunction.

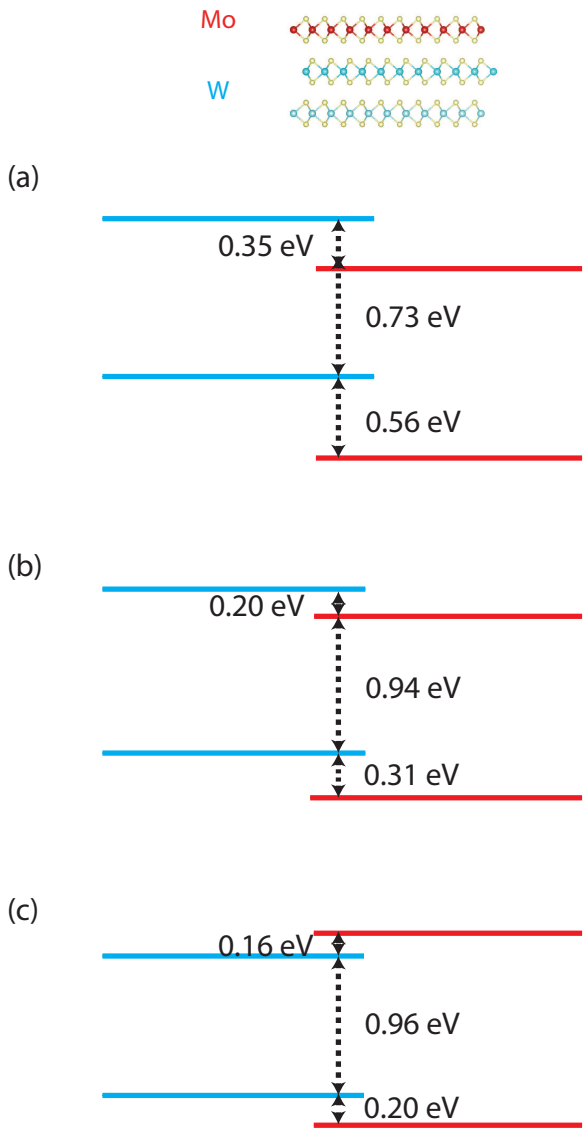

Figure 3.9: Band alignment of WSe_2 and $MoSe_2$ in trilayer system under (a) 0.2 eV/Å, (b) zero electric field and (c) -0.2 eV/Å. The layers with colors can be found as the small figure in (a).

Chapter 4

Graphene Contacts to A $HfSe_2/SnS_2$ Heterostructure

4.1 Introduction

Heterostructures of two-dimensional (2D) van der Waals (vdW) materials are being extensively investigated. [56–62] Recent studies of vdW heterostructures have shown that it is possible to build type II heterojunctions and nearly broken gap heterojunctions. [15, 63–66, 66, 67] In type II heterojunctions, the electron-hole pair is separated both spatially and energetically enabling efficient photovoltaics and photodetection. [64,65] A few heterostructures composed of 2H transition metal dichalcogenides, such as $WSe_2/MoSe_2$, remain direct gap with the conduction and valence bands at **K**. The majority of heterostructures, such as, for example, black phosphorus/MoS_2 [15, 63] are indirect gap, with, in this particular case, the valence band at $\mathbf{\Gamma}$ and the conduction band at **K**. For elec-

tronic applications, multi-layer stacks of 2D materials such as black phosphorus/$SnSe_2$, [68] $WSe_2/SnSe_2$, [66, 67] graphene/BN/graphene [69] and graphene/WS_2 [70] are being exploited for tunnel devices and tunneling field-effect transistors (TFETs). There is also interest in using graphene to create direct bandgaps in multilayer heterostructures, [71–73] using graphene to contact or tune other 2D materials, [74–82] and to tune the workfunction to enhance cold cathode emission [83].

In the last application, [83] placing graphene on SnS_2 significantly reduced the workfunction from that of SnS_2 alone, and the charge transfer between the two materials resulted in p-type graphene and n-type SnS_2. The Fermi level of the composite aligned above the conduction band minimum of the SnS_2. From an electrical contact point of view, such an energetic alignment is a negative Schottky barrier contact, and it is highly desirable, since it gives a low contact resistance. [84]

Although there is no energetic barrier, the inter-layer current flow is limited by the inter-layer coupling between the two layers. This coupling will depend on the orbital composition of the bands and their positions in k-space. [85] This coupling is relatively weak between graphene and SnS_2 near the Fermi level. To increase the coupling while maintaining a negative Schottky barrier, we investigate the use of a third material, $HfSe_2$, that serves as a 'matrix element matching' layer between the SnS_2 and the graphene, since it has strong coupling to both the SnS_2 and the graphene.

In this paper, we analyze a multi-layer structure composed of monolayer $HfSe_2$, SnS_2, graphene, and BN. $HfSe_2$ and SnS_2 are both hexagonal, 2D materials with indirect band gaps of 1.1 eV [86] and 2.4 eV, [87] respectively, and the 1T polytype is energetically

stable for both materials. [56, 87–89] In monolayer form, their conduction bands are at **M**.Stacking the two layers together creates an indirect-gap heterojunction that has type II qualities, but it does not fall cleanly into any one of the categories used to classify heterostructures of three-dimensional semiconductors, i.e. type I, type II, or type III, since the conduction bands strongly couple, and the wavefunction is distributed across both layers. An electric field applied to the heterostructure causes a shift in weight of the conduction band wavefunction from the $HfSe_2$ layer to the SnS_2 layer such that the band alignment takes on a type I quality. A commensurate stacking on graphene or BN using a 2×2 supercell of the $HfSe_2$ / SnS_2 and a 3×3 supercell of the graphene or BN zone-folds the **M** point of the $HfSe_2$ / SnS_2 back to $\mathbf{\Gamma}$, and it zone-folds the **K** point of the graphene or BN back to $\mathbf{\Gamma}$ resulting in a direct-bandgap heterostructure. The strain between the two systems is low, 1.7% for the BN and 0.1% for the graphene. The charge transfer from the graphene to the $HfSe_2$ / SnS_2 results in a negative Schottky barrier contact to the conduction band.

This paper is organized as follows. Sec. 4.2 describes the methods based on density functional theory. In Sec. 4.3, AA and AB stacked heterostructures of $HfSe_2$ / SnS_2 are first analyzed, and the effect of an applied vertical electric field is described. Then a third layer of either graphene or BN is added, and the tri-layer structures are analyzed and discussed. Conclusions are presented in Sec. 4.4.

4.2 Method

Density functional theory calculations are performed with the Vienna *ab initio* simulation package (VASP) [47–49] in the projected-augmented-wave method [50]. The

generalized gradient approximation (GGA) of the Perdew-Burke-Ernzerhof form [32–34] (PBE) is used for the exchange correlation energy. The vdW interactions are included with the DFT-D2 method of Grimme [51]. The kinetic energy cutoff is 500 eV for all calculations. The first Brillouin zone is sampled with a $8 \times 8 \times 1$ $\mathbf{\Gamma}$-centered Monkhorst-Pack grid. During all structural relaxations, the convergence tolerance on the Hellmann-Feynman forces is less than 0.01 eV/ Å. A vacuum layer larger than 25 Å is used for heterostructures to eliminate the interaction between adjacent images in the vertical direction.

The optimized lattice constant of SnS_2 is 3.69 Å, and the optimized lattice constant of $HfSe_2$ is 3.72 Å. The lattice mismatch between SnS_2 and $HfSe_2$ is less than 1%. The lattice constant of the heterostructure is set to the average value of 3.70 Å. The interlayer separation distances Δd, illustrated in Fig. 4.1(a), for the relaxed heterostructures are 2.89 Å for AA stacking and 2.99 Å for AB stacking. As a check of the sensitivity of the electronic bandstructure to the lattice constant, we considered the two extreme cases resulting from exchanging the lattice constants of $HfSe_2$ and SnS_2 and re-calculating the bandstructures of the individual layers. We found that the bandstructures of the individual material remained almost the same.

To determine more accurate values for bandgaps, electronic structure calculations are also performed with the hybrid Heyd-Scuseria-Ernzerhof (HSE) functional. [31] The HSE calculations incorporate 25% short-range Hartree-Fock exchange. The screening parameter μ is set to 0.2 Å^{-1}.

4.3 Results and Discussion

As shown in Fig. 4.1(a) and (b), we consider AA and AB stacking of $HfSe_2$ on SnS_2. Both 1T bulk $HfSe_2$ and SnS_2 stack in AA order in which the metal atoms of one layer align with the metal atoms of the other. Sliding one layer with respect to the other such that the metal atoms of one layer align with the chalcogenide atoms of the other gives AB stacking. AA and AB stacking correspond to the two most stable stacking geometries. The binding energy, E_b, is negative for both stacking arrangements. It is defined as $E_b = E_{\text{bilayer}} - (E_{HfSe_2} + E_{SnS_2})$, where E_{bilayer} is the total energy of the AA or AB stacked heterostructure, and E_{HfSe_2} and E_{SnS_2} are the total energies of the isolated $HfSe_2$ and SnS_2 layers, respectively. For the AA stacked heterostructure $E_b = -0.244$ eV/UC, and for the AB stacked heterostructure $E_b = -0.226$ eV/UC, where UC is the unit cell consisting of 6 atoms (one metal and two chalcogens from each layer). The binding energy for AA stacking is 18 meV/UC more negative than for AB stacking indicating that AA stacking is the most stable structure. Charge transfers from the $HfSe_2$ to the SnS_2 as the two layers are brought together, and the calculated Bader charge [90] transfer is 0.0075/UC (6.3×10^{12} cm^{-2}) for AA stacking and 0.0080/UC (6.7×10^{12} cm^{-2}) for AB stacking.

In k-space, both stacking arrangements have an indirect band gap with the conduction band minimum (CBM) at the **M** point and the valence band maximum (VBM) at $\mathbf{\Gamma}$. In real-space, the CBM is more heavily weighted on the SnS_2 layer, and the VBM is localized on the $HfSe_2$ layer. The colors of the electronic bands in Fig. 4.1(c,d) indicate the layer on which the wavefunction is most heavily weighted as indicated in the legend. The PBE indirect bandgaps are 237 meV and 224 meV for the AA and AB structures,

respectively. There are two conduction bands close to each other in energy at the **M** point, and they originate from the conduction bands of the two individual layers. The energy gap between the two lowest conduction bands is 316.5 meV and 285.3 meV for AA and AB stacking, respectively.

A more accurate determination of the energy spacings is obtained by calculating the electronic structure shown in Fig. 4.2 using the HSE hybrid functional. Qualitatively, the orbital composition and the order of the bands remain the same and the primary difference is that the conduction-valence bandgaps increase. The bandgaps increase to 0.88 eV and 0.89 eV for the AA and AB structures, respectively. However, the energy separation between the two conduction bands at **M** remains essentially unchanged with energies of 317.6 meV and 281.4 meV for AA and AB structures, respectively. This energy spacing between the two conduction bands is the critical energy that governs the crossing of the two conduction bands under an applied electric field. Since both the HSE and PBE calculations predict the same energy separation, we use the computationally less expensive PBE functional to predict the behavior of the heterostructure under applied cross-plane (vertical) electric fields. Furthermore, since the VBM remains strongly localized in the $HfSe_2$ for all electric fields and multi-layer structures, the focus of the rest of the paper will be on the two lowest conduction bands and their evolution with electric field and in contact with graphene or BN.

When the two monolayers are brought together, the orbitals of the CBM in each layer will couple and push apart in energy. To understand the evolution of the bands as the two materials are brought together, we perform a DFT calculation of the AA structure

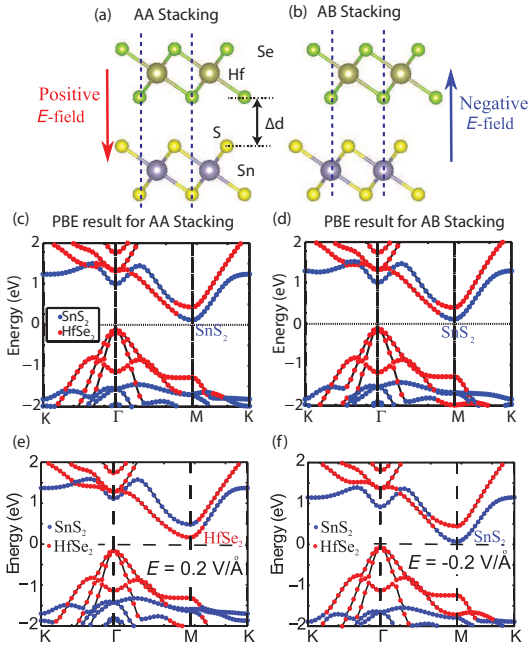

Figure 4.1: Atomic structure of (a) AA stacking and (b) AB stacking. (c) AA electronic structure and (d) AB electronic structure under zero electric field calculated by PBE. Bandstructure of the AA heterostructure under (e) positive electric field ($\mathcal{E} = 0.2$ V/Å) and (f) negative electric field ($\mathcal{E} = -0.2$ V/Å). The arrows in (a) and (b) showing the direction of the applied electric field ($\mathcal{E}$) for the energy wavevector plots in (e) and (f). Δd refers to the interlayer separation between Se atom in $HfSe_2$ and S atom in SnS_2.

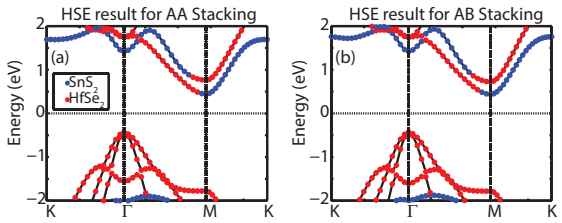

Figure 4.2: Electronic structure calculated with the HSE hybrid functional under zero electric field for (a) AA and (b) AB stacking.

with the two layers separated by 2 nm. This is sufficiently far apart that the bands do not interact, but a common Fermi level is enforced giving the band lineup of the well-separated, equilibrated, but non-interacting layers. The conduction band alignment of the separated system is shown in Fig. 4.3. When the layers are well-separated spatially, the energy separation of the two conduction bands is 0.25 eV. When the two layers are brought together to form the heterostructure, the two conduction bands push further apart by 40 meV for AB stacking and 70 meV for AA stacking. This increase in energy separation is related to the coupling between the two bands, and the larger splitting in the AA structure indicates stronger coupling between the two conduction bands in that stacking arrangement.

For the spatially separated structure, the two conduction bands are 100% localized on the individual layers. The lower conduction band is localized on the SnS_2, and the upper conduction band is localized on the $HfSe_2$. In the SnS_2, the conduction band wavefunction is weighted 54% on the Sn, with 89% of that contribution from the s orbital, and 45% on the S, with 83% of that contribution from the p_x and p_y orbitals. In $HfSe_2$, the conduction band wavefunction is weighted 79% on the Hf. 96% of that comes from the d orbitals with the heaviest weight of 35% coming from d_{z^2}. The 21% contribution from Se is 61% from the p_z orbital, 22% from the d orbitals, and 9% from the s orbital.

When the two layers are brought together to form the AA heterostructure, the magnitude squared of the CBM wavefunction no longer remains localized on the SnS_2, but becomes distributed across both layers. It is weighted approximately 60% on the SnS_2 and 40% on the $HfSe_2$. For the AB heterostructure, the wavefunction is weighted slightly more heavily on the SnS_2, with a weight of 67% on the SnS_2 and 33% on the $HfSe_2$. The fact that

the CBM wavefunction is weighted more heavily on the SnS_2 layer is consistent with the weaker coupling inferred from the smaller splitting of the bands in the AB structure. The orbital compositions of the individual layers remain qualitatively the same as those of the isolated layers. The VBM always remains localized in the $HfSe_2$ with an orbital composition from the p_x and p_y orbitals of the Se.

For both stacking arrangements, there is strong hybridization of the conduction band wavefunctions of the two individual layers, and the conventional spatially resolved band picture illustrated in Fig. 4.4(a) does not provide a good representation of the physics, at least for the conduction band. Instead, for the conduction band, the picture of bonding and anti-bonding molecular orbitals is more faithful to the underlying physics. In this picture the lower and upper conduction band at the M point are the bonding and anti-bonding combination of the isolated conduction bands of the individual layers. As the two layers are brought together, the bands couple and push apart resulting in two levels with the bonding orbital more heavily weighted on the SnS_2. However, there is no energy barrier for an electron to move between the two layers, since the CBM wavefunction is a coherent superposition of the orbitals on both layers, and the probability of finding an electron on the SnS_2 layer is at most a factor of 2 larger than on the $HfSe_2$ layer.

By applying an electric field, the relative weights on each layer of the first conduction band can be altered and even reversed. As illustrated in Fig. 4.1(a) and (b), a positive electric field corresponds to a positive voltage applied to the $HfSe_2$ layer, which means that the energy levels of the $HfSe_2$ layer are lowered with respect to those in the SnS_2 layer. Figs. 4.1(e) and (f) show the AA electronic structure under forward and reverse bias,

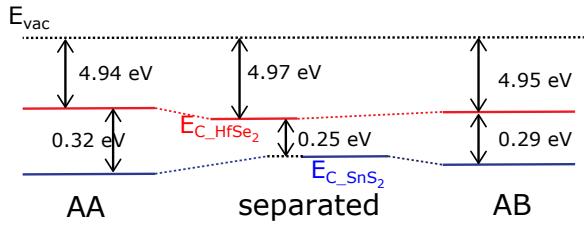

Figure 4.3: The two lowest conduction band edges of the spatially separated $HfSe_2/SnS_2$ system (center), the AA stacked heterostructure (left), and AB stacked heterostructure (right). E_{vac} is the energy level of vacuum. In the well-separated case, the blue line is the conduction band edge of SnS_2, and the red line is the conduction band edge of $HfSe_2$. For the AA and AB heterostructures, the red and blue lines indicate on which layer the conduction band edge wavefunction is most heavily weighted.

respectively. Under forward bias, the majority of the spectral weight of the CBM switches from the SnS_2 to the $HfSe_2$. The bandstructures with band compositions under ± 0.4 V/Å, ± 0.3 V/Å, and ± 0.1 V/Åelectric field for both heterostructures can be found in Appendix A.

The orbital compositions of the CBMs are illustrated in Fig. 4.4 for three different electric fields, -0.4 V/Å, 0 V/Å, and 0.4 V/Å, corresponding to the left, middle, and right columns, respectively. Fig. 4.4(a) illustrates the band alignments with the usual band picture used for bulk semiconductor heterojunctions for the 3 different electric fields. The left side of each band diagram represents the $HfSe_2$ layer and the right side represents the SnS_2 layer. The energy level of the CBM only indicates on which layer it is more heavily weighted.

As the electric field is ramped from negative to positive, the spectral weight of the conduction band minimum gradually shifts from the SnS_2 layer to the $HfSe_2$ layer. This shift of the wavefunction is illustrated in Fig. 4.5 for the AA and AB heterostructures. Fig. 4.5 shows the energies of the two lowest CBMs with the energy reference taken as the middle

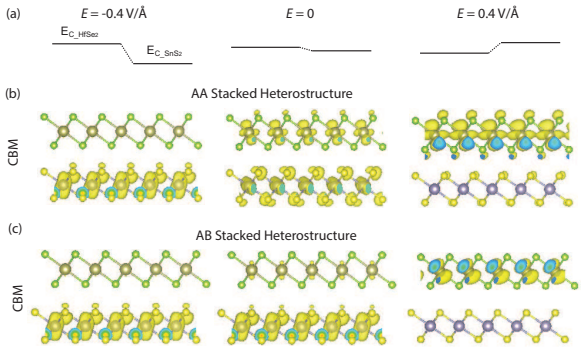

Figure 4.4: (a) Schematic view of band alignments under -0.4 V/Å, 0 V/Å, and 0.4 V/Å. (b) Isosurfaces of the orbital resolved wave-functions of the CBM of the AA stacked heterostructure under applied electric fields of -0.4, 0, and 0.4 V/Å. (c) Isosurfaces of band resolved wave-functions of the CBM andof the AB stacked heterostructure under applied electric fields of -0.4, 0, and 0.4 V/Å.

of the PBE bandgap. The spectral weight of the wavefunction on the $HfSe_2$ layer (red) and the SnS_2 layer (blue) are shown for each CBM and each electric field. Since the wavefunction is normalized, for each band and each electric field, the sum of the two weights is 1.0. The color of the lines and datapoints indicate the layer corresponding to the majority weight of the wavefunction. The trends and quantitative values for the AA and the AB stacked heterostructures are very similar. At zero field, the CBM is weighted towards the SnS_2 as previously discussed. At negative fields, the CBM wavefunction becomes more localized on the SnS_2 layer. A shift in the CBM weight from the SnS_2 to the $HfSe_2$ layer occurs between positive fields of 0.1 and 0.2 V/Å. As the field becomes more positive the CBM wavefunction becomes more localized on the $HfSe_2$. As the field is swept from negative to positive, the electronic structure transitions from a type II heterostructure to type I heterostructure as indicated in Fig. 4.5.

Two dimensional materials will be in contact with other materials as contacts, substrate, or encapsulation to prevent oxidation. All-2D systems are very attractive since

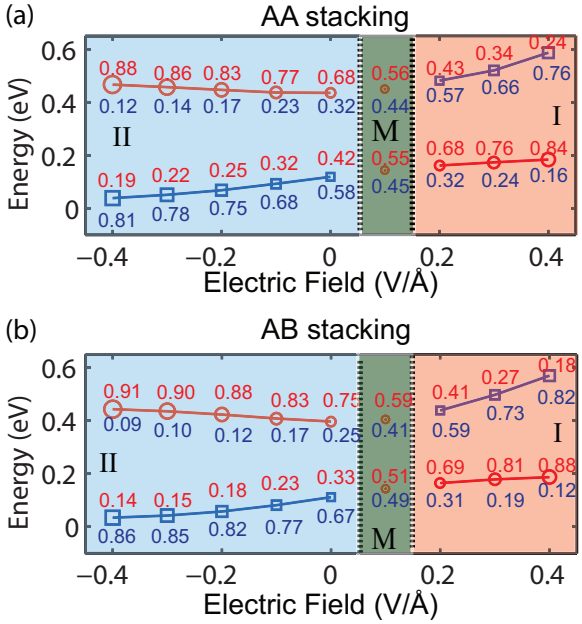

Figure 4.5: (a) Evolution of the two lowest conduction band edges as a function of electric field for the (a) AA and (b) AB heterostructures. $E = 0$ corresponds to the middle of the PBE calculated bandgap. The colors of the lines and the datapoints indicate the layer corresponding to the majority weight of the wavefunction, blue for SnS_2 and red for $HfSe_2$. The shape and size of the datapoints indicate the relative weight of the wavefunction on the majority layer, blue squares for SnS_2 and red circles for $HfSe_2$. The numerical weights of the wavefunction on the $HfSe_2$ and SnS_2 layers for each band are given above (red) and below (blue) each datapoint, respectively. The two weights add up to be 1.0.

the interfaces are self-passivated and devoid of dangling bonds. BN is a good insulator, and has recently been demonstrated to protect highly reactive black phosphorous from oxidation [91]. Graphene, a good conductor, is closely lattice matched to BN. A 3×3 supercell of graphene or BN is also very closely lattice matched to a 2×2 supercell of $HfSe_2/SnS_2$. The lattice constants of BN and graphene are 2.51 Å, and 2.47 Å, respectively. The lattice mismatches between the BN or graphene 3×3 supercells and the $HfSe_2/SnS_2$ 2×2 supercell are 1.7% and 0.1%, respectively. The lattice constant of the supercell is fixed to be the lattice constant of the $HfSe_2/SnS_2$ heterostructure, so that the the $HfSe_2/SnS_2$ heterostructure remains unstrained. The average interlayer distances between BN and the $HfSe_2$ layer of the $HfSe_2/SnS_2$ AA or AB heterostructures are 3.26 Å and 3.25 Å, respectively. For graphene on either side of the $HfSe_2/SnS_2$ AA stacked structure, the average interlayer distances of graphene/$HfSe_2$ and graphene/SnS_2 are 3.34 Å and 3.36 Å, respectively. For graphene on either side of the AB stacked structure, the average interlayer distances of graphene/$HfSe_2$ and graphene/SnS_2 are 3.35 Å and 3.36 Å, respectively.

The tri-layer systems are stable. The binding energy between graphene or BN on the $HfSe_2/SnS_2$ heterostructure is defined as $E_b = [E_{\text{trilayer}} - (E_{\text{AA/AB}} + E_{\text{graphene/BN}})]/N$ where E_{trilayer} is the total energy of the trilayer system, $E_{\text{AA/AB}}$ is the total energy of AA or AB heterostructure, $E_{\text{graphene/BN}}$ is the total energy of the isolated graphene or BN system, and N is the number of atoms (18) in the graphene or BN unit cell. The binding energies are negative, and they are listed below in units of meV per atom of the BN or graphene. For BN on $HfSe_2/SnS_2$ as shown in Fig. 4.6, the binding energy is -44 meV. The binding energies for graphene on the $HfSe_2$ side or the SnS_2 side of the AA stacked heterostructure

shown in Fig. 4.7 are -116 meV and -93 meV, respectively. The binding energies for graphene on the $HfSe_2$ side or the SnS_2 side of the AB stacked heterostructure are very similar, and they are -120 meV and -97 meV, respectively. Therefore, the trilayer systems are stable, and the graphene tri-layer structure with graphene on the $HfSe_2$ is most stable.

Fig. 4.6(a) shows the structure and supercell of a BN monolayer on the $HfSe_2$ layer of the $HfSe_2/SnS_2$ heterostructure. The electronic bandstructures for the AA and AB heterostructures with BN on the $HfSe_2$ layer are shown in Figs. 4.6(b) and (c), respectively. The bands of the $HfSe_2/SnS_2$ layers show no noticable change due to the proximity of the BN. The BN bands are far from the Fermi energy and are buried deep in the valence and conduction bands of the $HfSe_2/SnS_2$ as one would expect for a wide bandgap insulator. Only the BN valence band can be seen on this energy scale. What is most notable about this energy-momentum plot is that all of the band edges now occur at $\mathbf{\Gamma}$. This is a result of zone-folding. The 2×2 supercell of the $HfSe_2/SnS_2$ folds the $\mathbf{M}$ points back to $\mathbf{\Gamma}$, and the 3×3 supercell of the BN folds the $\mathbf{K}$ points back to $\mathbf{\Gamma}$. Thus, the system becomes direct gap. The zone-folding of the different Brillouin zones is illustrated in Fig. 4.6(a).

Placing graphene on either the $HfSe_2$ layer or the SnS_2 layer of the AA or AB stacked heterostructures results in charge transfer from the graphene to the $HfSe_2/SnS_2$ heterostructure such that the graphene becomes p-type, the $HfSe_2/SnS_2$ becomes n-type, and the Fermi level aligns above the CBM of the $HfSe_2/SnS_2$. The structures and energy-momentum relations are shown in Figs. 4.7(a-d) and 4.8(a-d) for graphene on the top or bottom of the AA or AB heterostructures, respectively. The charge transfer n_s can be estimated by integrating the low-energy graphene density of states [92], $N(E) = \frac{2}{\pi(\hbar v)^2}|E -$

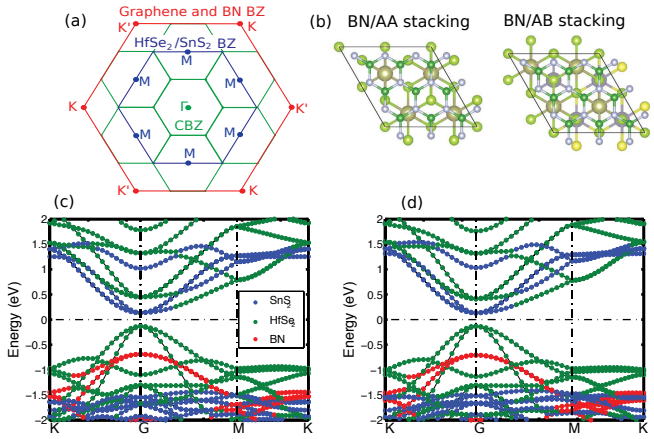

Figure 4.6: BN on $HfSe_2/SnS_2$. (a) Brillouin zone folding resulting from the 2×2 unit cell of the $HfSe_2/SnS_2$ and the 3×3 unit cell of the BN or graphene. The outer Brillouin zone (BZ) in red is the BZ of the graphene or BN. The BZ in blue is the BZ of the $HfSe_2/SnS_2$. The innermost BZ in green is the commensurate BZ (CBZ) of the supercell. The CBZ is tiled over the entire k-space region to show that the **M** point of the blue BZ lies at the $\mathbf{\Gamma}$ point of the first repeated CBZ, and the **K** point of the red BZ lies at the $\mathbf{\Gamma}$ point of the second repeated CBZ. (b) Atomistic structures for BN on AA and AB stacked $HfSe_2/SnS_2$. (c) Electronic bandstructure for AA stacking. (d) Electronic bandstructure for AB stacking. In (c) and (d), the color indicates on which layer the wavefunction is most heavily weighted.

$E_D|$, from the Fermi level E_F to the Dirac point E_D giving $n_s = \frac{1}{\pi(\hbar v)^2}(E_D - E_F)^2$ with $v = 0.81 \times 10^6$ m/s. For the AA stacked $HfSe_2/SnS_2$ heterostructure shown in Fig. 4.7(a-d), with graphene on the $HfSe_2$, $E_D - E_F = 0.335$ eV, and $n_s = 1.26 \times 10^{13}$ cm^{-2}. With graphene on SnS_2, $E_D - E_F = 0.430$ eV, and $n_s = 2.07 \times 10^{13}$ cm^{-2}. By electronic device standards, this sheet charge density transferred from the graphene into the $HfSe_2/SnS_2$ is large. These estimates are close to the Bader charge transfer [90] calculated from VASP. With graphene on the $HfSe_2$ layer of the AA heterostructure, the Bader charge calculation gives a charge transfer from the graphene into the $HfSe_2/SnS_2$ bilayer of $n_s = 1.13 \times 10^{13}$ cm^{-2}, which is distributed between the $HfSe_2$ and the SnS_2 layers as 7.35×10^{12} cm^{-2} on the $HfSe_2$ and 3.93×10^{12} cm^{-2} on the SnS_2. With graphene on the SnS_2 layer, the Bader charge calculation gives a charge transfer from the graphene into the $HfSe_2/SnS_2$ of

$n_s = 1.33 \times 10^{13}$ cm^{-2}, which is distributed between the $HfSe_2$ and SnS_2 layers as 3.31×10^{12} cm^{-2} on the $HfSe_2$ and 1.00×10^{13} cm^{-2} on the SnS_2.

For the AB stacked heterostructure shown in Fig. 4.8(a-d), with graphene on $HfSe_2$, $E_D - E_F = 0.319$ eV gives the estimate $n_s = 1.14 \times 10^{13}$ cm^{-2}. With graphene on SnS_2, $E_D - E_F = 0.452$ eV corresponds to $n_s = 2.29 \times 10^{13}$ cm^{-2}. For graphene on $HfSe_2$, the Bader charge calculation gives a charge transfer from the graphene into the $HfSe_2/SnS_2$ bilayer of $n_s = 1.07 \times 10^{13}$ cm^{-2}, which is distributed between the $HfSe_2$ and the SnS_2 layers as 5.71×10^{12} cm^{-2} on the $HfSe_2$ and 5.00×10^{12} cm^{-2} on the SnS_2. With graphene on SnS_2 the Bader charge calculation gives a charge transfer from the graphene into the $HfSe_2/SnS_2$ bilayer of $n_s = 1.24 \times 10^{13}$ cm^{-2}, which is distributed between the $HfSe_2$ and the SnS_2 layers as 2.44×10^{12} cm^{-2} on the $HfSe_2$ and 1.00×10^{13} cm^{-2} on the SnS_2.

The electron transfer from the graphene to the $HfSe_2/SnS_2$ is accompanied by a lowering of the potential of the layer in contact with the graphene. The region of the electronic bands around the Fermi level near $\mathbf{\Gamma}$ is shown in Figs. 4.7(e-f) and 4.8(e-f). In all cases, the lowest conduction band wavefunction is weighted more heavily towards the layer in contact with the graphene. This results in a negative Schottky barrier between the graphene and the conduction band of $HfSe_2/SnS_2$ for contact to either side of the heterostructure.

For a good contact, energy level alignment is critical, but there should also be coupling between the graphene and the $HfSe_2/SnS_2$ layers for electrons to transfer easily between the two layers. This coupling or interaction appears in the energy-momentum plots as an anti-crossing of the graphene and $HfSe_2/SnS_2$ bands. The anti-crossing of

the graphene band and the $HfSe_2/SnS_2$ conduction band is shown in Figs. 4.7(e,f) and 4.8(e,f). The color coding of the bands is the same as in Figs. 4.7(c,d) and 4.8(c,d). In this commensurate Brillouin zone, the conduction band of the $HfSe_2/SnS_2$ is 3-fold degenerate (excluding spin), since the 6 **M** points of the original $HfSe_2/SnS_2$ Brillouin zone are folded to $\mathbf{\Gamma}$. The Dirac cone of the graphene is two-fold degenerate, since the **K** and $\mathbf{K}'$ points of the original graphene Brillouin zone are folded to $\mathbf{\Gamma}$. Where the bands anti-cross shown in the region of the vertical ellipses, the interaction between the graphene and the $HfSe_2$ breaks the degeneracy, so that the 2 Dirac cones and 3 conduction bands from the $HfSe_2/SnS_2$ can be clearly seen in Figs. 4.7(e) and 4.8(e). In Figs. 4.7(e) and 4.8(e), the Dirac cone of the graphene anti-crosses with the conduction bands of the $HfSe_2/SnS_2$ with an energy splitting Δ on the order of 100 meV. A value for the coupling t can be estimated from the energy splitting Δ of the splitting of bands at the crossing points. Setting $\Delta = 2t$, gives $t \approx 50$ meV. In the energy-momentum region where the bands anti-cross indicated by the vertical ellipses, the wavefunction composition is a mix of orbitals from the graphene and the $HfSe_2/SnS_2$. The composition of the three bands circled by the left ellipse in Fig. 4.7(e) are, from lowest energy to highest energy: (1) 26% SnS_2, 44% $HfSe_2$, and 29% of graphene; (2) 22% SnS_2, 38% $HfSe_2$, and 40% graphene; and (3) 48% SnS_2, 47% $HfSe_2$, and 4% graphene. The orbital composition of the bands circled by the right ellipse along the line from $\mathbf{\Gamma}$ to **M** are very similar. Thus, both the energetic splitting and the orbital mixing indicate that there is significant coupling between the graphene and the $HfSe_2$ layer that should allow easy charge transfer between the layers under applied bias.

The interaction of graphene with $HfSe_2$ is larger than with SnS_2, and this is consistent with the orbital composition of the conduction bands of $HfSe_2$ and SnS_2. The conduction band of $HfSe_2$ has large Hf d_{z^2} and Se p_z components, and the conduction band of SnS_2 has large Sn s and S p_x, p_y components. In comparison to the SnS_2 s and $p_{x,y}$ orbitals, the out-of-plane d_{z^2} and p_z orbitals of the $HfSe_2$ would be expected to couple more stongly across the van der Waals gap to the C p_z orbitals of the graphene due to their increased spatial overlap. When the graphene is placed on the SnS_2 layer, the bands near the Fermi level shown in Fig. 4.7(f) look qualitatively different compared to the bands with graphene on the $HfSe_2$ layer. At $\mathbf{\Gamma}$, the 3 conduction bands of the $HfSe_2/SnS_2$ remain degenerate. All 3 of the conduction bands now lie 0.03 eV below the Fermi level, so that the Schottky barrier becomes more negative. This is consistent with the fact that, as shown in Fig. 4.3, the conduction band of the SnS_2 is energetically lower than that of $HfSe_2$, and the conduction band wavefunction of the isolated $HfSe_2/SnS_2$ heterostructure is more heavily weighted towards the SnS_2 layer as shown in Fig. 4.1. The energy alignment is more favorable for electrical contact, however the coupling between the graphene and the SnS_2 is considerably weaker. Now, the maximum energy splitting is ≈ 10 meV giving an estimate for the coupling of $t \approx 5$ meV.

The difference in coupling can also be seen in the composition of the conduction band wavefunctions at the $\mathbf{\Gamma}$ point. For graphene on $HfSe_2$, at the $\mathbf{\Gamma}$ point, the compositions of the three conduction bands nearest the Fermi energy, from lowest to highest energy are: (1) 40% SnS_2, 54% $HfSe_2$, and 5% graphene; (2) 40% SnS_2, 55% $HfSe_2$, and 5% of graphene; and (3) 48% of SnS_2, 52% of $HfSe_2$, and 0% graphene. The highest split-off conduction band

has its weight shifted more towards the SnS_2 layer compared to the lower two conduction bands, and it has no graphene contribution. With graphene on the SnS_2, the compositions of the three conduction bands nearest the Fermi energy at the $\mathbf{\Gamma}$ point, are all the same, and they are 65% SnS_2, 35% $HfSe_2$, and 0% graphene.

The trends for graphene on the AB stacked structure are qualitatively the same as for graphene on the AA structure. As discussed with respect to Fig. 4.3, the interlayer coupling between the SnS_2 and $HfSe_2$ is weaker in the AB stacking arrangement compared to that with AA stacking. Therefore, the wavefunction of the conduction band edge is more heavily weighted towards the SnS_2 in the isolated heterostructure. In the AB structure, placing the graphene on the $HfSe_2$, reverses the weight of the bottom two conduction bands in Fig. 4.8, so that their compositions become (1) 43% SnS_2, 51% $HfSe_2$, and 5% graphene; and (2) 43% SnS_2, 52% $HfSe_2$, and 5% graphene. The spectral weight of the highest band is 52% SnS_2, 48% $HfSe_2$, and 0% graphene. The only qualitative difference between this structure and the AA structure is the slight shift in orbital weight of the conduction band wavefunction towards the SnS_2.

The values of the interlayer couplings t can be used in a tunneling Hamiltonian expression to estimate the interlayer conductance between the graphene and the $HfSe_2/SnS_2$ heterostructure when graphene is placed on either the SnS_2 layer or the $HfSe_2$ layer. The interlayer conductivity can be written as,

$$\sigma_c = \frac{g_s g_G g_H e^2}{\mathcal{A}h} \sum_{\mathbf{k}} \int dE A_G(\mathbf{k}; E) A_H(\mathbf{k}; E) |t|^2 \frac{-\partial f(E - E_f)}{\partial E}, \tag{4.1}$$

where $A_G(\mathbf{k};E)$ and $A_H(\mathbf{k};E)$ are spectral functions of the graphene layer and the semiconductor heterostructure, respectively, $g_s = 2$ is the spin degeneracy, $g_G = 2$ is the graphene band degeneracy, $g_H = 3$ is the $HfSe_2/SnS_2$ band degeneracy, $\mathcal{A}$ is the cross-sectional area, $f(E - E_f)$ is the Fermi-Dirac factor, E_f is the Fermi level, and t is the interlayer coupling. The spectral functions are $A_G(\mathbf{k};E) = \frac{\gamma}{(E+\hbar v_F k-\varepsilon_D)^2+\gamma^2/4}$, $A_H(\mathbf{k};E) = \frac{\gamma}{(E-\frac{\hbar^2k^2}{2m^*}-\varepsilon_H)^2+\gamma^2/4}$, where γ is the lifetime broadening, $m^* = 0.4m_0$ is the effective mass obtained from the DFT bandstructures in Fig. 4.7(c)-(d), $v_F = 0.81 \times 10^6$ m/s is the Fermi velocity of graphene, ε_D is the energy of the Dirac point, and ε_H is the energy of the conduction band minimum of the $HfSe_2/SnS_2$ heterostructure. For a given transverse $\mathbf{k}$, the quantity $T(E,\mathbf{k}) = A_G(\mathbf{k};E)A_H(\mathbf{k};E)|t|^2$ is the transmission coefficient, and, as such, its value must lie between 0 and 1. [85] The values of ε_D and ε_H are chosen such that the lower Dirac cone of the graphene and the parabolic conduction band of the $HfSe_2/SnS_2$ intersect at the Fermi wavevector k_F, $(E_F + \hbar v_F k_F - \varepsilon_D) = (E_F - \frac{\hbar^2 k_F^2}{2m^*} - \varepsilon_H) = 0$, giving a maximum value for $T(E,\mathbf{k})$ of $16|t|^2/\gamma^2 \leq 1$. This, sets a lower limit on on the value for γ of $\gamma \geq 4|t|$. For graphene on $HfSe_2$, t is large, ≈ 50 meV, which pushes the limit of validity of the tunneling Hamiltonian expression (4.1), and it requires a large value for γ of 200 meV. The contact resistance is $R_C = 1/\sigma_c$, and the resulting value for the contact resistance of graphene on $HfSe_2$ as shown in Fig. 4.7(a) is 1 $\text{m}\Omega \cdot \mu\text{m}^2$. With graphene on SnS_2, $t \approx 5$ meV, and the contact resistance is 100 $\text{m}\Omega \cdot \mu\text{m}^2$. The resistances scale as $|t|^2$, which accounts for the factor of 100 difference in the contact resistances. Decreasing the value of γ monotonically decreases R_C by approximately a factor of 5 as γ is decreased from 200 meV to 20 meV. These resistance values should be viewed as order-of-magnitude estimates. Both of

these values are excellent in terms of the state-of-the art contact resistance to 2D materials [93], and the lowest value is competitive with the best that has been achieved in the well-developed semiconductors such as InGaAs [94].

4.4 Summary and Conclusions

Monolayer $HfSe_2$ and SnS_2 are closely lattice matched with a strain of less than 1%. When the two materials are well-separated, but with a common Fermi level, the $HfSe_2$ conduction band is 0.25 eV above the SnS_2 conduction band, and the valence band of the $HfSe_2$ is more than 1 eV above the valence band of the SnS_2. Such a band lineup in traditional three dimensional semiconductors leads to a type II heterostructure in which the conduction band is on one layer and the valence band is on the other. However, when the $HfSe_2$ and the SnS_2 are brought together to form a heterostructure, the conduction band minimum at **M** becomes a coherent superposition of the of the conduction band wavefunctions of the individual layers. The conduction band wavefunction is weighted 60% on the SnS_2 and 40% on the $HfSe_2$ for AA stacking and 67% on the SnS_2 and 33% on the $HfSe_2$ for AB stacking. There is no energy barrier for an electron to move between the two layers, since the conduction band wavefunction is a coherent superposition of the orbitals of both layers. A vertical electric field of 0.2 V/Å pointing from the $HfSe_2$ layer to the SnS_2 layer reverses the weights of the conduction band wavefunction to approximately 70% $HfSe_2$ and 30% SnS_2. In the SnS_2, the primary orbital contributions to the conduction band come from the s-orbital of the Sn and the $p_{x,y}$ orbitals of the S. In the $HfSe_2$, the primary orbital

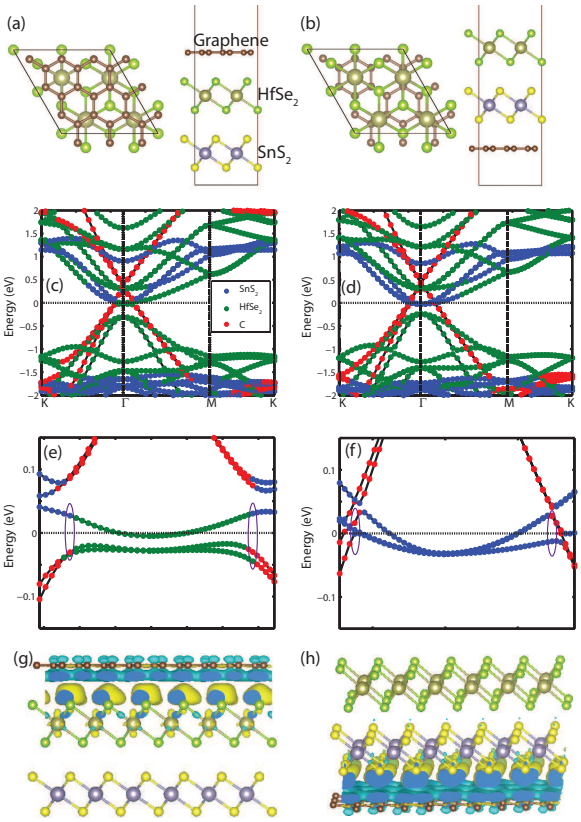

Figure 4.7: Trilayer of graphene and AA stacked $HfSe_2/SnS_2$. (a) Atomic structure of graphene on the $HfSe_2$ layer. (c) and (e) are the corresponding electronic structure plots. (e) focuses on the small energy range near the Fermi level. (g) shows the charge transfer at the interface. (b) Atomic structure of graphene on the SnS_2 layer. (d) and (f) are the corresponding electronic structure plots. (f) focuses on the small energy range near the Fermi level. (h) shows the charge transfer at the interface. In (g) and (h), the charge accumulation and depletion is denoted by the yellow and blue color, respectively. The Fermi level is at $E = 0$. The purple circles in (e) and (f) indicate the anti-crossing of the graphene hole band and the $HfSe_2/SnS_2$ conduction band.

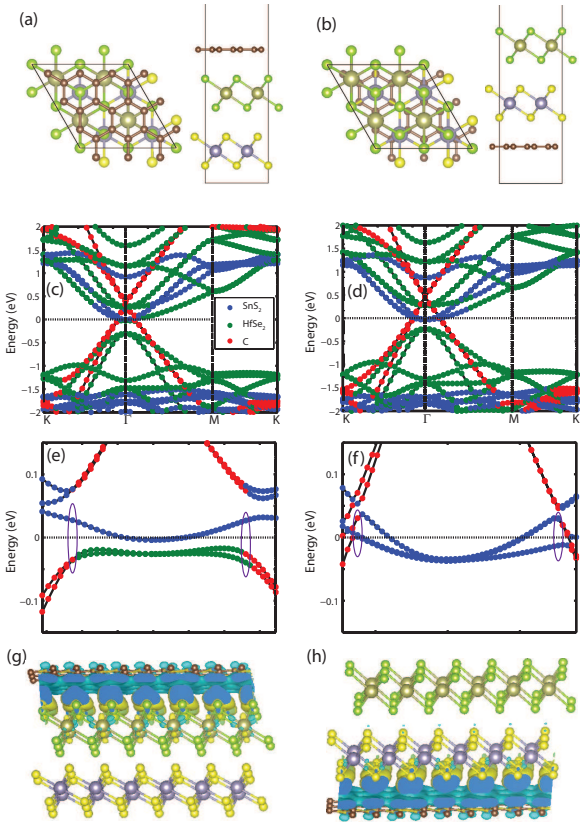

Figure 4.8: Trilayer of graphene and AB stacked $HfSe_2/SnS_2$. (a) Atomic structure of graphene on the $HfSe_2$ layer. (c) and (e) are the corresponding electronic structure plots. (e) focuses on the small energy range near the Fermi level. (g) shows the charge transfer at the interface. (b) Atomic structure of graphene on the SnS_2 layer. (d) and (f) are the corresponding electronic structure plots. (f) focuses on the small energy range near the Fermi level. (h) shows the charge transfer at the interface. In (g) and (h), the charge accumulation and depletion is denoted by the yellow and blue color, respectively. The Fermi level is at $E = 0$. The purple circles in (e) and (f) indicate the anti-crossing of the graphene hole band and the $HfSe_2/SnS_2$ conduction band.

contributions come from the d_{z^2} orbital of the Hf and the p_z orbital of the Se. The valence band maximum at $\mathbf{\Gamma}$ is localized on the $HfSe_2$ layer, and its dominant orbital contributions come from the p_x and p_y orbitals of the Se. The calculated HSE bandgap of the AA and AB heterostructures are 0.88 eV and 0.89 eV, respectively.

A 3×3 supercell of graphene is almost perfectly lattice matched to a 2×2 supercell of $HfSe_2/SnS_2$ with a lattice mismatch of 0.1%. The trilayer heterostructure is stable with negative binding energies, and the binding energy with graphene on the $HfSe_2$ is approximately 23 meV / C atom more negative than with graphene on the SnS_2. This indicates a stronger interaction of the graphene with the $HfSe_2$, which is consistent with the results from the electronic structure calculations. A charge density on the order of $10^{13}/\text{cm}^2$ transfers from the graphene to the $HfSe_2/SnS_2$ resulting in a Fermi level that aligns within the conduction band of the the $HfSe_2/SnS_2$ and a negative Schottky barrier contact for electron injection into the conduction band. The coupling of the graphene to the $HfSe_2$ is approximately 10 times larger than the coupling of the graphene to the SnS_2, and this is consistent with the d_{z^2} and p_z orbital composition of the $HfSe_2$ conduction band compared to the s and $p_{x,y}$ composition of the SnS_2 conduction band. A tunneling Hamiltonian estimate for the contact resistance of graphene on the $HfSe_2$ layer versus graphene on the SnS_2 layer gives contact resistances of 1 $\text{m}\Omega \cdot \mu\text{m}^2$ and 100 $\text{m}\Omega \cdot \mu\text{m}^2$, respectively. Both values would be considered exceptional for 2D materials, and the lowest value is competitive with lowest contact resistances measured in 3D semiconductors such as InGaAs.

Chapter 5

Strain Effect and Electric Field Effect in $PtSe_2/SnS_2$

5.1 Introduction

Layered two-dimensional (2D) materials have been studied extensively. They have unique dangling bond free surfaces, due to interlayer van der Waals (vdW) interaction. Vertical heterostructure composed of 2D materials can integrate interesting properties of each individual material into one structure. Due to the variety of numerous layered 2D materials, it is possible to design vertical heterostructures with a wide range of bandgap and material properties. For example, vertical heterostructures composed of black-phosphorene and graphene can be used for making contacts. [95] $SnSe_2$/black phosphorene has nearly broken-gap band alignment, and can be used as a channel for tunneling Field Effect Transistors (TFETs). [96]

In this draft, *ab-initio* density functional theory calculations are used to simulate the electronic structures of a vertical heterostructure composed of monolayer SnS_2 and monolayer $PtSe_2$. The band alignment of the heterostructure is studied under three applied conditions, strain, electric field, and with graphene contact. Our study indicates that $PtSe_2/SnS_2$ forms an intrinsic type II heterojunction with a Mexican hat at $\mathbf{\Gamma}$ point. Under in-plane biaxial compressive strains, a semiconducting to metal transition can be observed; while under in-plane tensile strains, the height of Mexican hat increases to over six times of the value under 0 % of strain. As vertical electric field is ramped from negative to positive, the bandgap of the heterostructures increases monotonically. Putting graphene contact on $PtSe_2/SnS_2$ heterostructures forms p-type graphene with n-type $PtSe_2/SnS_2$ heterostructures. The heterostructure with graphene on contact with SnS_2 forms negative Schottky barrier which is the desired case for building field effect transistors.

5.2 Method

The Vienna ab initio simulation package (VASP) [47–49] in the projected-augmented-wave method [50] is implemented to calculate the band structures in Fig. 5.1. The generalized gradient approximation (GGA) of the Perdew-Burke-Ernzerhof (PBE) form [32–34] is used for the exchange-correlation energy. The vdW interactions in SnS_2 and $PtSe_2$ are accounted for by using the DFT-D2 method of Grimme [51] for both the bulk and the heterostructure. The kinetic energy cutoff is set to a converged value of 500 eV for all calculations. During all structural relaxations, the convergence tolerance on the Hellmann-Feynman forces is less than 1×10^{-3} eV/Å. A converged $8 \times 8 \times 1$ Monkhorst-Pack k-point

mesh is used for the calculation of 2D films. A vacuum layer larger than 25 Å is used for all heterostructures. All electronic structures of the heterostructures in this chapter are calculated using PBE functional.

5.3 Results and Discussion

Both $PtSe_2$ and SnS_2 are stable under 1T polytype. [56, 87–89, 97] The calculated lattice constant of SnS_2 is 3.69 Å, and the lattice constant of $PtSe_2$ is 3.73 Å. The lattice mismatch between these two materials is less than 1%. A vertical heterostructure composed of the SnS_2 and $PtSe_2$ is built with a lattice constant of 3.707 Å. Different stacking orders for $PtSe_2/SnS_2$ heterostructures are considered as shown in Fig. 5.1. From our study it shows that AA and AB stacking orders shown in Fig. 5.1 are the most favorable, energy-wise. The in-plane positions of the two layers in AA stacked heterostructure are the same. The chalcogen atom is on top of the chalcogen atom, while the metal atom is on top of metal atom. AB stacked heterostructure is shown in Fig. 5.1 (b). Compared to the bottom layer, the top layer slides about 2.14 Å such that the chalcogen atom is right on top of the metal atom.

The spin-orbit coupling (SOC) is crucial for $PtSe_2/SnS_2$ as there is significant band splitting in the valence bands due to Se element. Hence the SOC is considered in the calculations analyzing the $PtSe_2/SnS_2$ heterostructure under influence of strain and electric field.

The band structures of AA and AB stacked heterostructures under zero external fields are shown in Fig. 5.2. AA and AB stacked heterostructures have indirect bandgap

of 234 meV and 311 meV, respectively. As shown in Fig. 5.2, the lowest conduction band and highest valence band have been marked in red. The conduction band minimum (CBM) for both structures is at **M** point of Brillouin zone (BZ) and the valence band maximum (VBM) is at the point between the **Γ**-**K** of BZ which has been marked in Fig. 5.2 with the cross sign. Fig. 5.2(c-d) show that the CBM is more heavily weighted on Sn and the VBM is more heavily weighted on Se. Around **Γ** the VBM is composed of in-plane σ-bonds whereas the bands far from **Γ** are composed of out-of-plane π-bonds. The heterostructure forms an intrinsic type II heterojunction. Band splitting due to SOC at CBM for both AA and AB stacked heterostructures is negligible, each is less than 1 meV. The SOC splitting at VBM is very large, and the value is 170 meV for Fig. 5.1(a) and 141.8 meV for Fig. 5.1(b). The feature around **Γ** forms a Mexican hat in the valence bands for both AA and AB stacked heterostructures. The height of Mexican hat for AA heterostructure is 95.8 meV, and for AB heterostructure is 33.7 meV which is about $\frac{1}{3}$ of the value of the AA heterostructure.

The remaining parts are arranged as follows: in the first section, we will discuss the strain effect in the heterostructure; the second section will focus on the influence

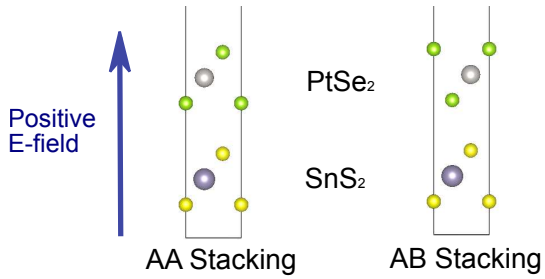

Figure 5.1: Schematic views of AA and AB stacked heterostructures. The top layer is $PtSe_2$ and the bottom layer is SnS_2. The positive direction of the applied electric field is shown as an arrow.

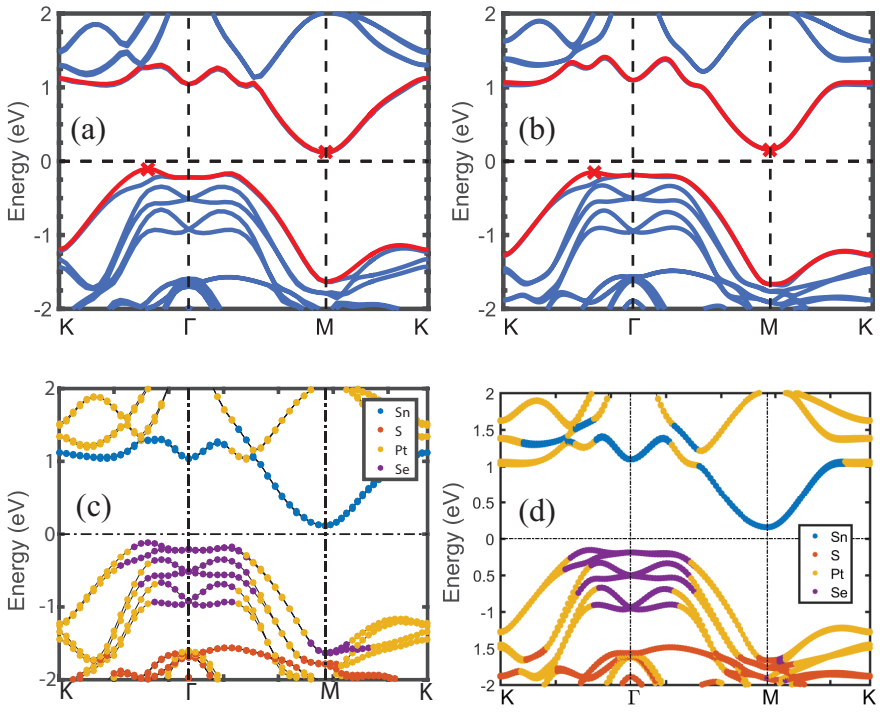

Figure 5.2: Band structure of heterostructure composed of monolayer SnS_2 and monolayer $PtSe_2$ with SOC. (a) AA stacked heterostructure with CBM and VBM marked with red; (b) AB stacked heterostructure with CBM and VBM marked with red; (c) ionic composition of AA stacked band structure; (d) ionic composition of AB stacked band structure.

from the electric field; the last section investigates the graphene contacts to $PtSe_2/SnS_2$ heterostructure.

5.4 Strain Effect

Due to the unique features of the van der Waals (vdW) materials, there are two different types of strains to be considered, an in-plane biaxial strain along each monolayer plane, and a vertical strain with changing the value of vdW gap between the two monolayer planes. Fig. 5.3 shows the band structures of AA stacked heterostructures under different vertical strains. The strain under this category is considered as the vdW gap deviation from the equilibrium state (zero strain configuration). Negative and positive signs refer to the vdW gap as less or more than the vdW gap at the equilibrium state. The unit of the changing of vdW gap is Å. These results in Fig. 5.3 show that changes to the vdW gaps have almost no influence on the electronic structures of heterostructure. The compositions of CBM and VBM remain the same as the one shown in Fig. 5.2. The results of AB stacked heterostructure are also similar to the one in Fig. 5.2.

On the contrary, the in-plane strain can significantly tune the band structures of $PtSe_2/SnS_2$. A transition from semiconducting to metallic is observed under the in-plane strain. The band structures for AA and AB stacked heterostructures under in-plane strains are shown in Fig. 5.5 and Fig. 5.6 respectively. For both AA and AB stacked heterostructures, large compressive strain can result in metallic configurations, as shown in Fig. 5.5(c) and Fig. 5.6(c). The other significant change of band structures under

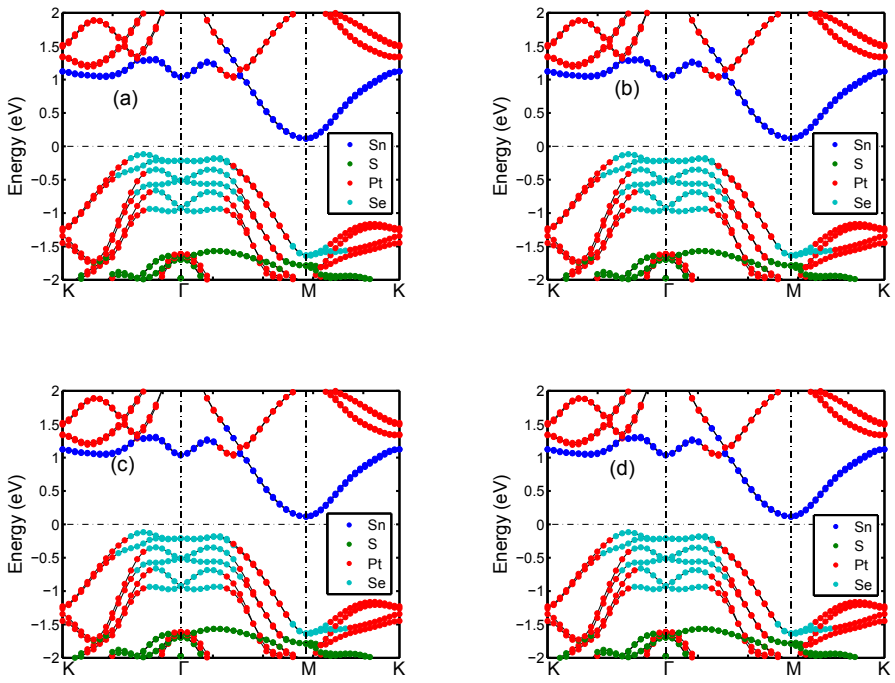

Figure 5.3: Band structure of AA stacked heterostructure under vdW strain. (a)0.4 Å; (b) 0.8 Å; (c) -0.4 Å; (d) -0.8 Å. The values represents the difference between the current vdW gap and the one in equilibrium state.

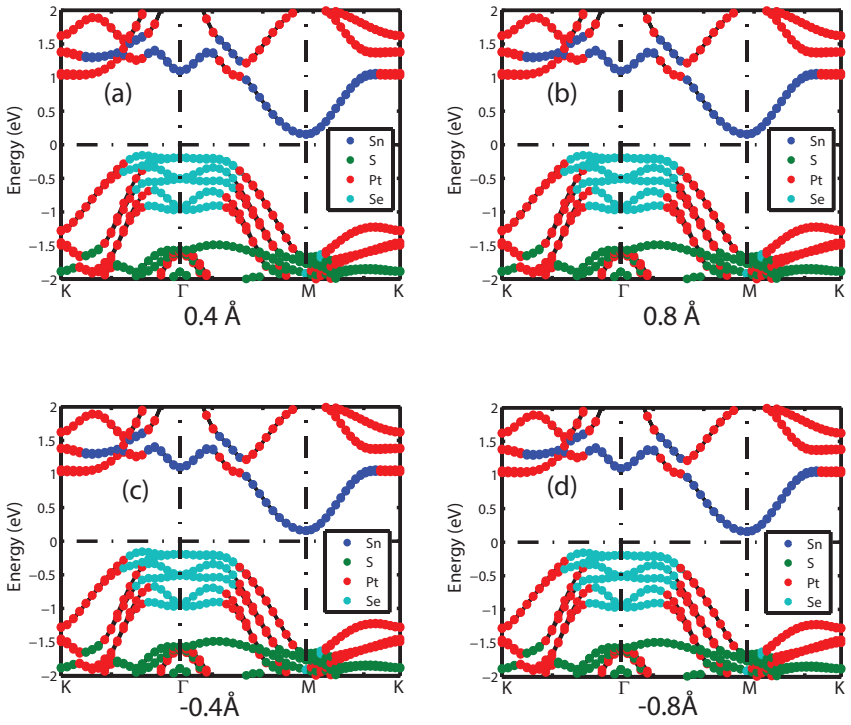

Figure 5.4: Band structure of AB stacked heterostructure under vdW strain. (a)0.4 Å; (b) 0.8 Å; (c) -0.4 Å; (d) -0.8 Å. The values represents the difference between the current vdW gap and the one in equilibrium state.

compressive strain is that the VBM is moved to **Γ** as shown in the figures; the CBM gradually moves from **M** to the point between **K** and **Γ**. The compositions of VBM for band structure shown in Fig. 5.5 and Fig. 5.6 remain localized on Se atoms which is the same as those without strain. In the conduction bands, the band composition gradually changes from Sn to Pt as a result of the movement of CBM. Under tensile strains, the height of Mexican hat in the valence bands increases to 590 meV for AA stacked heterostructure shown in Fig. 5.5 (d), and 331 meV for AB stacked heterostructure shown in Fig. 5.6 (d). Both values are over six times of the values without strain. The VBM of band structures for both heterostructures under tensile strain remains at the position of VBM under 0 strain; the change of CBM in AA stacked heterostructure is different from the one in AB stacked heterostructure. As shown in Fig. 5.5, the conduction band at **Γ** is no longer parabolic, but shows some small peaks. With the increment of tensile strain, the CBM moves from **M** to the point along **Γ**-**M**; the band composition also changes from Sn to S. The conduction band of AB stacked heterostructure remains as parabolic at **Γ**, and with the increment of tensile strain, the CBM moves from **M** to **Γ**. Similar to AA stacked structure under tensile strain, the band composition of AB stacked structure at CBM also changes from Sn to S.

From our study, it is evident that the bandgap can be significantly tuned by the in-plane biaxial strain. A semiconducting to metallic transition can be observed under large compressive strains in both AA and AB stacked structures; the compressive strain can move the VBM to **Γ** point. The tensile strain results in a more prominent Mexican hat at **Γ** point and moves CBM for **M** to either **Γ** or the point along **Γ**-**M**. On the contrary,

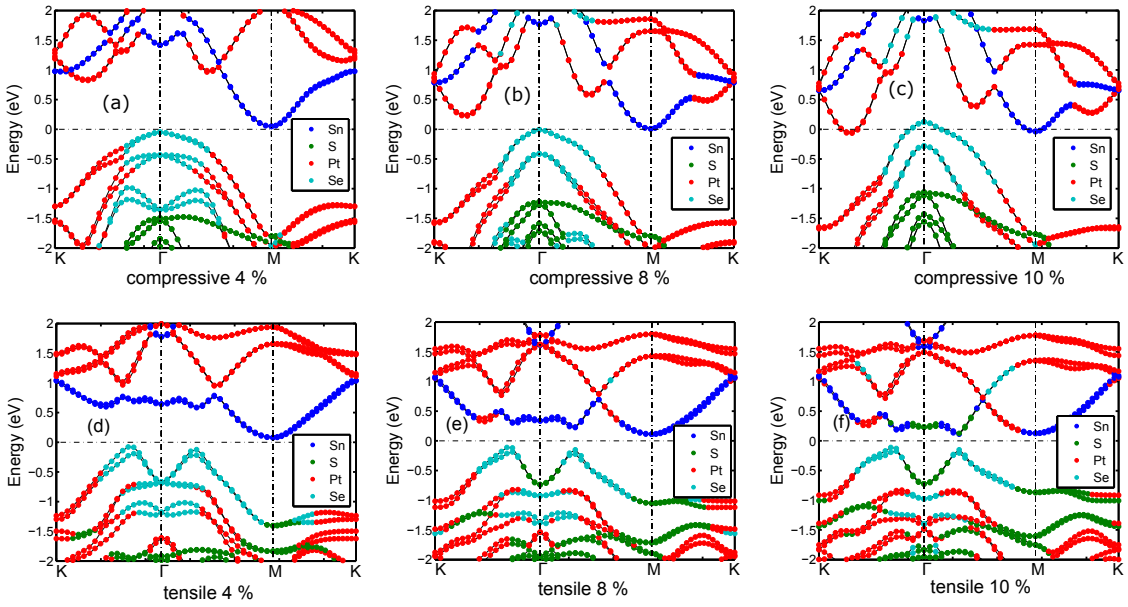

Figure 5.5: Band structure of AA stacked heterostructure resulted from in-plane compression and tensile strains. (a) Compressive 4 % strain; (b) compressive 8 % strain; (c) compressive 10 % strain; (d) tensile 4 % strain; (e) tensile 8 % strain; (f) tensile 10 % strain.

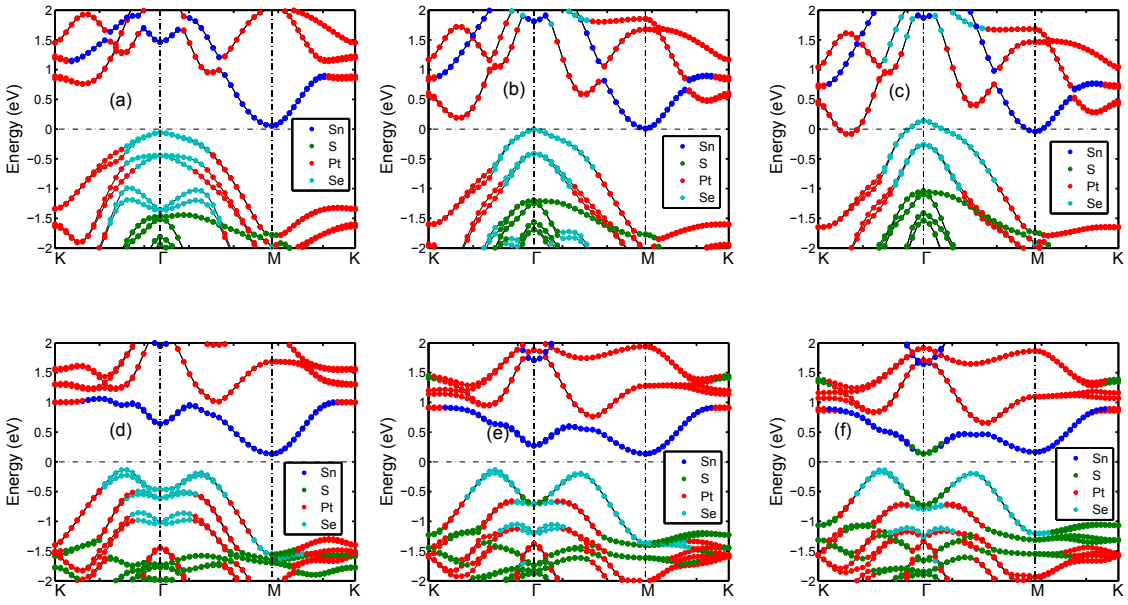

Figure 5.6: Band structure of AB stacked heterostructure resulted from in-plane compression and tensile strains. (a) Compressive 4 % strain; (b) compressive 8 % strain; (c) compressive 10 % strain; (d) tensile 4 % strain; (e) tensile 8 % strain; (f) tensile 10 % strain.

the change of vdW gap for both AA and AB stacked heterostructures will not change the band composition and the shape of the band structures.

5.5 Electric Field Effect

This section discusses the influence of the applied electric field on $PtSe_2/SnS_2$ heterostructures. The change of bandgap as a function of the electric field is shown in Fig. 5.7. For both AA and AB stackings, the change is asymmetric to the applied field. As the electric field is ramped from negative to positive, bandgap of heterostructure increases monotonically. For both heterostructures, under negative applied electric field, bandgap closes, in the meantime, the band offsets increases. From the band structures of AA and AB stacked heterostructures shown in Fig. 5.8 and Fig. 5.9, we can see that the compositions at CBM and VBM remain the same as they would under zero electric field. For AA stacking, it shows that the positive electric field can lead to a larger valley between VBM and $\mathbf{\Gamma}$, while the negative electric field can finally result in a flat band at $\mathbf{\Gamma}$ point. Under positive electric field, the height of Mexican hat shown in Fig. 5.8 is about 142.2 meV under 0.5 eV/Å which is about twice of the one without electric field. For the SOC splitting, comparing the band structure with electric field to the band structure without electric field, the SOC induced splitting gap remains about the same value of about 160 meV. For AB stacked heterostructure, 106.7 meV and 584.4 meV are the bandgap values under -0.5 eV/Å and 0.5 eV/Å respectively. The changing of height of Mexican hat for AB stacked heterostructure is quite similar to the AA stacked heterostructure. From -0.1 eV/Å to

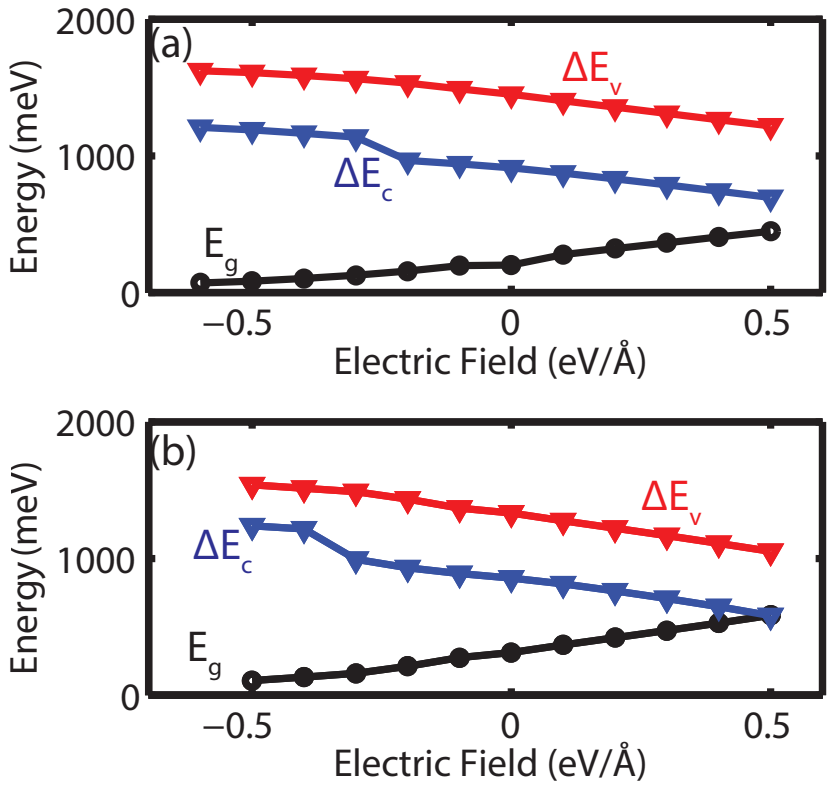

Figure 5.7: Evolution of bandgap and band offsets of $PtSe_2/SnS_2$ heterostructure as a function of applied electric field. (a) AA stacking heterostructure, (b) AB stacking heterostructure. E_g refers to the bandgap, ΔE_c is the offset for conduction bands between the two materials; ΔE_v is the offset of valence bands.

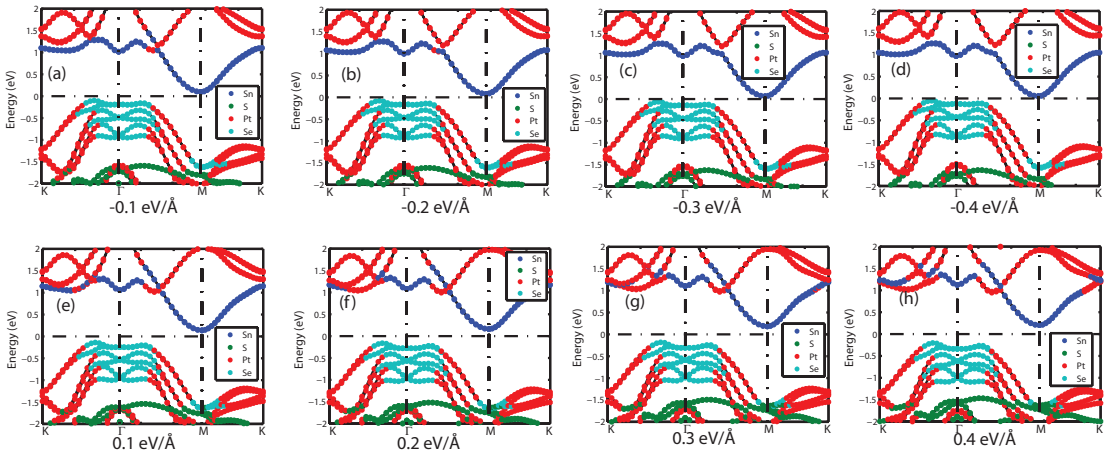

Figure 5.8: Band structures of AA stacked heterostructure under different electric field. (a) -0.1 eV/Å, (b) -0.2 eV/Å, (c) -0.3 eV/Å, (d) -0.4 eV/Å, (e) 0.1 eV/Å, (f) 0.2 eV/Å, (g) 0.3 eV/Å, (h) 0.4 eV/Å. The Fermi level is set as the middle of the gap.

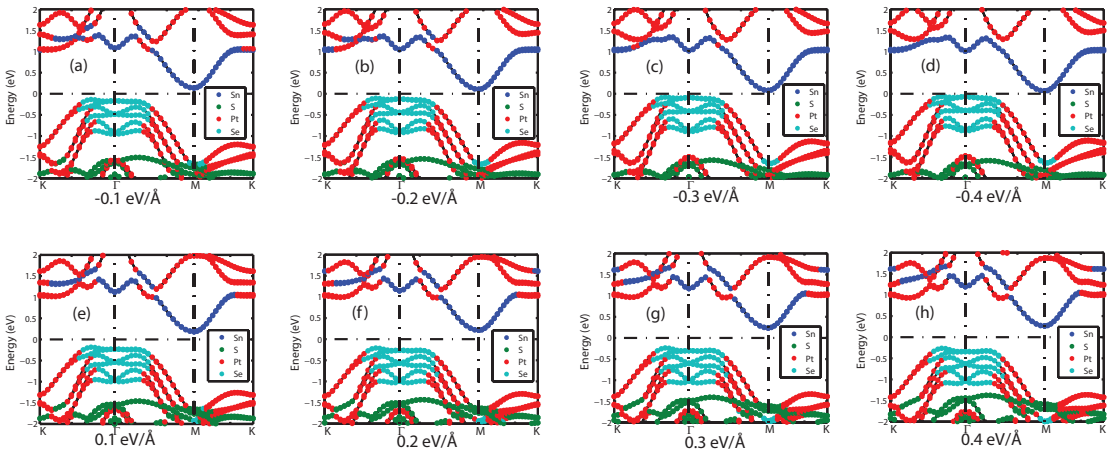

Figure 5.9: Band structures of AB stacked heterostructure under different electric field. (a) -0.1 eV/Å, (b) -0.2 eV/Å, (c) -0.3 eV/Å, (d) -0.4 eV/Å, (e) 0.1 eV/Å, (f) 0.2 eV/Å, (g) 0.3 eV/Å, (h) 0.4 eV/Å. The Fermi level is set as the middle of the gap.

-0.4 eV/Å, the VBM is gradually switching from the point between **K** and **Γ** to **Γ** point as shown in Fig. 5.9. By applying an electric field, we not only change the bandgap but the position of VBM as well.

5.6 Graphene Contacts

In this section, the electronic structures of the heterostructure with graphene contact are studied. Graphene has exceptional electrical properties. [98] A 3×3 supercell of graphene is closely lattice matched with the 2×2 supercell of $PtSe_2/SnS_2$. The lattice constant of $PtSe_2/SnS_2$ heterostructure is 3.707 Å, while the lattice constant of graphene is 2.47 Å. The lattice mismatch between graphene supercell and heterostructure supercell is less than 1%. The lattice constant of the trilayer system is fixed to the lattice constant of $PtSe_2/SnS_2$ supercell which makes the heterostructures unstrained. To apply graphene contact, there are two different stackings for each of the $PtSe_2/SnS_2$ heterostructures, graphene in contact with $PtSe_2$ or graphene in contact with SnS_2. All calculations in this part are performed with PBE without SOC since we will focus on the analyze of the conduction bands, while the SOC contributes to conduction bands are negligible.

In Fig. 5.10, it is clear that for both different stackings, the Dirac cone of graphene goes inside the conduction bands of $PtSe_2/SnS_2$. Both Dirac cone and CBM are folded to **Γ** point. This zone folding is similar to the one shown in Fig. 4.6(a). In Fig. 5.8, the Dirac cone is 159.9 meV above the Fermi level for graphene in contact with $PtSe_2$, and 363.0 meV for graphene in contact with SnS_2. The CBM is 0.2 meV above the Fermi level for graphene

in contact with $PtSe_2$, and 19.4 meV below the Fermi level for graphene in contact with SnS_2.

The results of trilayer systems with graphene as contacts for AB stacked heterostructure are shown in Fig. 5.9. It has similar band structures, the Dirac cone is 103.4 meV above the Fermi level of the heterostructure with graphene contact on $PtSe_2$; while the energy difference between Dirac cone and Fermi level in the heterostructure with graphene on SnS_2 is 390.9 meV which is over four times of 103.4 meV. The energy difference between the CBM and the Fermi level is 12.3 meV for graphene on contact with $PtSe_2$ configuration, and -24.2 meV (negative sign refers to the CBM below the Fermi level) for graphene on contact with SnS_2.

Both AA and AB stacked heterostructure with graphene on either the $PtSe_2$ layer or the SnS_2 layer result in charge transfer from graphene to the $PtSe_2/SnS_2$ heterostructure such that the graphene becomes p-type, the $PtSe_2/SnS_2$ becomes n-type. The Fermi level aligns above the CBM of the graphene on contact with SnS_2 configuration for both AA and AB stacked heterostructures, which forms negative Schottky barrier. The charge transfer n_s can be estimated by integrating the low-energy graphene density of states [92], $N(E) = \frac{2}{\pi(\hbar v)^2}|E-E_D|$, from the Fermi level E_F to the Dirac point E_D giving $n_s = \frac{1}{\pi(\hbar v)^2}(E_D-E_F)^2$ with $v = 0.81\times10^6$ m/s. E_D-E_F refers to the value of the energy difference between Dirac cone and the Fermi level. Therefore, for the AA stacked $PtSe_2/SnS_2$ heterostructure shown in Fig. 5.10(a) with graphene on the $PtSe_2$ layer, $n_s = 2.87\times10^{12}$ cm^{-2}. With graphene on the SnS_2 layer (Fig. 5.10(b)), $n_s = 1.48\times10^{13}$ cm^{-2}.

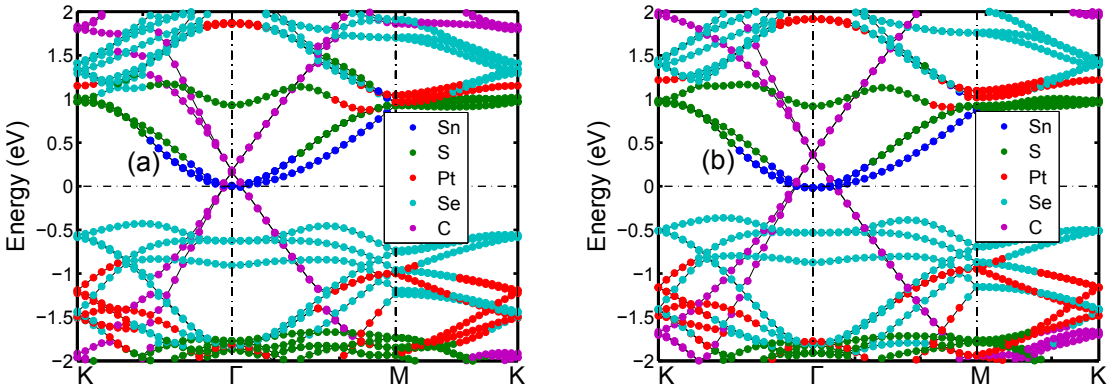

Figure 5.10: Band structures of AA stacked heterostructure with graphene as contact. (a) Graphene in contact with $PtSe_2$; (b) graphene in contact with SnS_2.

For the AB stacked heterostructure shown in Fig. 5.6, with graphene on the $PtSe_2$ layer, $n_s = 1.20 \times 10^{12}$ cm^{-2}. With graphene on the SnS_2 layer, $n_s = 1.72 \times 10^{13}$ cm^{-2}.

5.7 Conclusion

From our study of $PtSe_2/SnS_2$ heterostructures, we know that AA and AB stackings are the two preferred stacking orders, energy-wise. The in-plane strain can significantly change the band structures; under compressive strains, there is a semiconducting to metal transition, the VBM move to **Γ**, and the CBM shifts to localize on Pt element along **Γ**-**K**; under tensile strain, the height of Mexican hat increases to over six times of the value without strain. The bandgaps of $PtSe_2/SnS_2$ heterostructures can be changed with applied electric fields, but the band edge compositions remain the same as the composition without applied electric field. Putting graphene on $PtSe_2/SnS_2$ results in n-type $PtSe_2/SnS_2$ and p-type graphene. The Fermi level aligns above the CBM for the configuration of graphene on contact with SnS_2, which forms negative Schottky barrier. Due to the large energy dif-

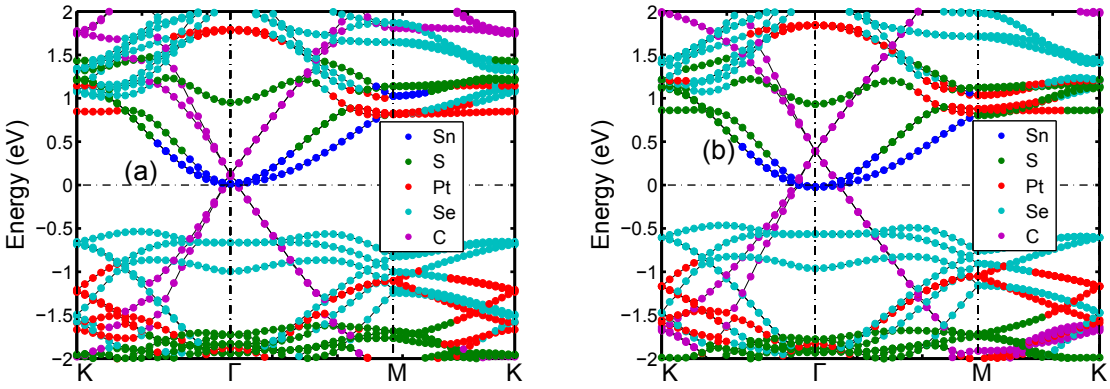

Figure 5.11: Band structures of AB stacked heterostructure with graphene as contact. (a) Graphene in contact with $PtSe_2$; (b) graphene in contact with SnS_2.

ference between Dirac cone and the Fermi level for the configuration of graphene on contact with SnS_2, its charge transfer is one magnitude larger than the configuration of graphene on contact with $PtSe_2$.

Chapter 6

The Effect of Intervalley Interaction on the Band Topology of Commensurate Graphene/EuO Heterostructures

6.1 Introduction

Ever since the classification of the integer quantum Hall effect (IQHE) in terms of topological invariants, [99] significant theoretical effort has gone towards realizing IQHE phenomenology at vanishing external magnetic fields. Haldane [100] proposed that in the presence of an intrinsic spin-orbit coupling, spinless electrons hopping on a two-dimensional honeycomb lattice are topologically non-trivial, and this can result in one-dimensional chi-

ral gapless excitations along the edges of a gapped graphene system. Owing to the chiral nature of these edge modes, the gapless edge states are dissipationless and exhibit a Hall conductance $\sigma_{xy} = e^2/h$. This Hall conductance is a consequence of the Berry curvature associated with the Bloch bands in momentum space, and it is quantized only when the Fermi energy lies in the bulk bandgap of the material. A number of other proposals have been made for realizing the quantum anomalous Hall (QAH) effect in mercury-based quantum wells, [101] optical lattices, [102] disorder induced Anderson insulators, [103] magnetic topological insulators, [104,105] and ferromagnetic graphene. [106,107] The robust nature of charge transport which identifies the QAH effect at vanishing magnetic fields might enable design of novel quantum devices for low-power electronics applications.

To realize the QAH state in realistic materials two conditions are necessary, (i) broken time reversal symmetry and (ii) topologically non-trivial bands. Since topological insulators (TIs) possess a large spin-orbit coupling, [108] a route towards realizing the QAH effect is to introduce ferromagnetic ordering in TIs. Immediately following recent successes in synthesizing magnetic TIs (MTIs), transport measurements in MTIs verified the predicted e^2/h Hall conductance. [104, 109] Another approach is to engineer the QAH state in ferromagnetic graphene in the presence of Rashba spin-orbit coupling. [106,107] Recently, graphene was successfully deposited on an atomically thin-film insulating ferrimagnet, yttrium iron garnet (YIG), and the transport measurements revealed an unquantized anomalous Hall effect due to proximity induced ferromagnetism. [110] Several other magnetic material/van der Waals (vdW) materials combinations (for example graphene/EuO, graphene/$BiFeO_3$ and $MoTe_2$/EuO [106,111–113]) have been proposed for possible spintron-

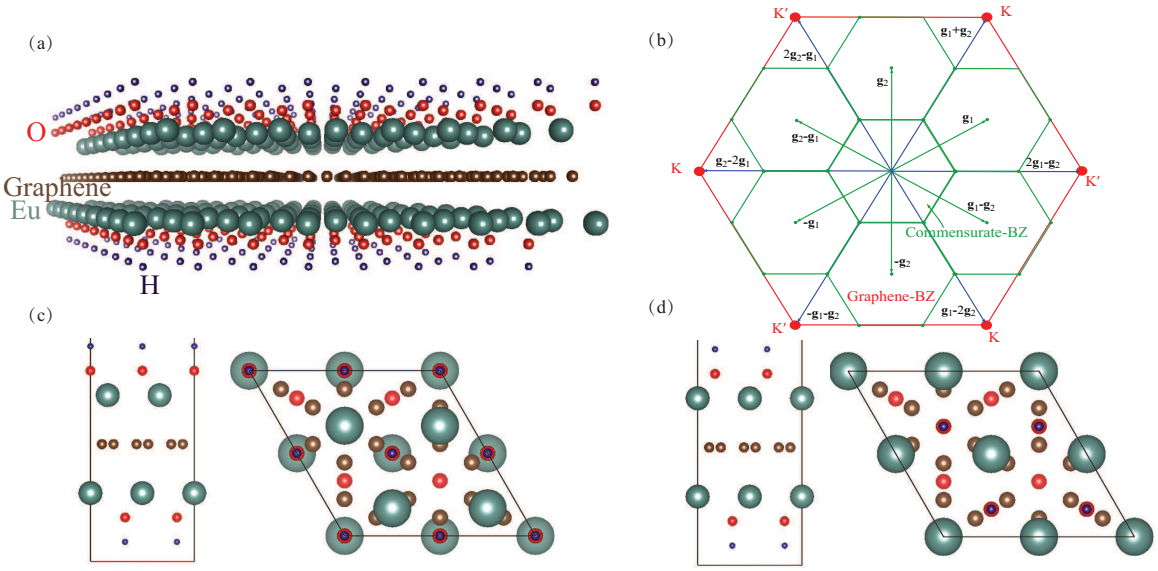

Figure 6.1: (Color online) (a) Schematic view of a heterostructure with graphene between two EuO layers. The O layers are terminated with H atoms, and the surfaces abutting the graphene are the Eu (111) planes. (b) The reciprocal lattice corresponding to the unit cells shown in (c) and (d) maps the $\mathbf{K}$ and $\mathbf{K}'$ points of the hexagonal graphene Brillouin Zone (BZ) indicated by the outer red hexagon to the $\mathbf{\Gamma}$ point of the commensurate BZ of the graphene/EuO unit cell indicated by the central green hexagon. The $\mathbf{g_i}$'s are the reciprocal lattice vectors of the heterostructure unit cells in (c) and (d). Elevation and plan views of the unit cells corresponding to the two graphene/EuO geometries are shown in (c) for the Eu-misaligned structure and (d) for the Eu-aligned structure.

ics [111, 112] and valleytronics [113] applications. In these systems, ferromagnetic ordering is induced by a proximity effect. Additionally, proximity induced magnetism by a magnetic insulator allows for control of the electron and hole densities by gating. Previous theoretical studies have reported an exchange splitting gap of 36 meV in graphene/EuO heterostructures. [112]

In this paper, we construct a model Hamiltonian to analyze the effect of commensurability and the resulting zone-folding and inter-valley interaction on the topological properties of commensurate graphene/EuO heterostructures. Such heterostructures can be constructed by placing graphene on the (111) surface of EuO, and our model Hamiltonian is applicable to any commensurate graphene/EuO heterostructure. For commensurate graphene/EuO heterostructures the low-energy graphene bands at the $\mathbf{K}$ and $\mathbf{K}'$ are folded to the $\mathbf{\Gamma}$ point, which is due to the $3N \times 3N$ super-lattice of the commensurate graphene-EuO stacking. This zone-folding is accompanied by two distinct types of inter-valley interactions, determined by the position of the Eu atoms that can sit on either the bridge site or the hollow site of the graphene lattice (see Fig. 6.1). Our model Hamiltonian is constructed to account for the inter-valley interactions induced by the Eu atoms, along with the magnetic exchange interactions and Rashba spin-orbit coupling. The parameters for the model Hamiltonian such as the strength of the inter-valley interactions, exchange splitting and spin-orbit coupling are determined by fitting to *ab initio* calculations. The low-energy band dispersion of the graphene/EuO heterostructure depends on the strength of the inter-valley interaction terms. The position of the bridge Eu atom reduces the graphene lattice symmetry from $C_{3v} \rightarrow C_{2v}$ and results in shifting the Dirac cones from $\mathbf{\Gamma}$ to new points in the

super-lattice Brilloun zone (BZ), whereas the Eu atoms on the hollow site open an energy gap at $\mathbf{\Gamma}$. This is a topologically trivial gap that is detrimental to achieving a QAH state. We analyze the band dispersion and the topological properties of the model graphene/EuO Hamiltonian and determine conditions under which the graphene-EuO heterostructure can acquire a non-zero Chern number.

The rest of the paper is organized as follows. In section 6.2, we describe the two types of commensurate graphene/EuO heterostructures and their super-lattice symmetries, and we discuss how these symmetries influence the band structure. In section 6.3, we develop the model Hamiltonian that captures the low-energy band dispersion of the graphene/EuO heterostructures with and without spin-orbit coupling. In section 6.4, calculations of the Chern numbers identify the conditions which yield topologically non-trivial bands and the QAH effect. Section 6.5 describes *ab initio* calculations from which we extract parameters for the model Hamiltonian such as exchange splitting, spin-orbit coupling, and the values of inter-valley scattering and mass terms. Section 6.6, concludes with a discussion of the possibility of proximity induced exchange and the observation of QAH effect in other graphene/ferromagnetic heterostructures.

6.2 Graphene/EuO Heterostructures

EuO is a ferromagnetic insulator with a Curie temperature of T_c $69K$ with a saturation magnetization of $7\mu_B$. It has a rock salt structure with the space group $Fm\bar{3}m$. Graphene is a honeycomb lattice of carbon atoms with a lattice constant 2.47 Å with the space group $P6_3mc$. In the graphene-EuO heterostructure, the graphene lies on the Eu

terminated (111) EuO surface. Each (111) layer of EuO contains 4 Eu atoms and 4 O atoms, and the Eu-layer and O-layers are stacked alternatively along the (111) direction. Each EuO layer is displaced $1.22\mathring{A}$ with respect to the adjacent layers. Twice of the lattice constant of EuO along the (111) surface is about $7.27\mathring{A}$, and it is commensurate with a 3×3 unit cell of graphene. In the combined hetero-structre the Eu atom sits either in a hollow site at the center of a graphene hexagon or at a bridge site above the center of a C-C bond.

Figs. 6.1(c,d) show the two different heterostructures studied in the paper. They differ by the alignment of the EuO-monolayer on opposite sides of the graphene layer. In both cases, graphene is placed on the (111) surface of EuO. This gives a commensurate heterostructure with a lattice constant 2 times the lattice constant of a EuO unit cell and 3 times that of the graphene unit cell. In the aligned structure, shown in Fig. 6.1(d), the top EuO-monolayer is directly above the bottom EuO-monolayer, whereas in the misaligned structure shown in Fig 6.1(c), the top Eu-monolayer has an in-plane displacement of 1.22 Å with respect to the bottom EuO layer. In both structures the Eu atoms either sit at the center of the hexagonal graphene unit cell or at the bridges of the C-C bonds coinciding with the inversion symmetric points of graphene's honeycomb lattice. Therefore, in-plane inversion symmetry is preserved for both cases. However, as a result of the lateral displacement of the EuO layer in the misaligned heterostructure, inversion symmetry perpendicular to the graphene sheet is broken in contrast to the aligned heterostructure where this symmetry is preserved. These symmetries play an important role in determining the band dispersion and the model Hamiltonian of the graphene/EuO heterostructure.

The lattice constants of the graphene-EuO unit cell are three times those of the graphene unit cell. Hence, the reciprocal lattice constant of the commensurate BZ is $\frac{1}{3}$ that of graphene's BZ as shown Fig. 6.1(b). The outer hexagon (red - online) is the BZ of the graphene primitive cell, and the central hexagon (green - online) is the BZ of the heterostructure unit cell. Fig. 6.1(b) shows that the **K** and **K**' points of the graphene BZ lie at equivalent **Γ** points in the extended zone of the heterostructure BZ. This results in zone folding of graphene's **K** and **K**$'$ points to **Γ**. This band folding leads to important changes in the band dispersion of the graphene-EuO heterostructure, when compared to the graphene band structure (see Section VI). We address this next as we construct the model Hamiltonian to describe the band dispersions of the two graphene/EuO heterostructures.

6.3 Low-Energy Effective Hamiltonian

In graphene, the gapless Dirac cones at **K** and **K'** are protected by time-reversal and inversion symmetry. Since these Dirac points are separated in the BZ, small perturbations cannot lift this valley degeneracy. Therefore, the valley index is a good quantum number. In the $3N \times 3N$ unit cell, due to zone folding of graphene's BZ, both valleys **K** and **K**' get mapped to **Γ**. Hence, valley symmetry is no longer preserved and inter-valley interactions can gap the Dirac bands at **Γ** without breaking inversion or time-reversal symmetry. In the graphene/EuO heterostructures, Eu adatoms positioned at the bridge and hollow sites contribute two distinct inter-valley interaction terms that are responsible for the non-linear dispersions obtained from the *ab initio* calculations. In this section, we con-

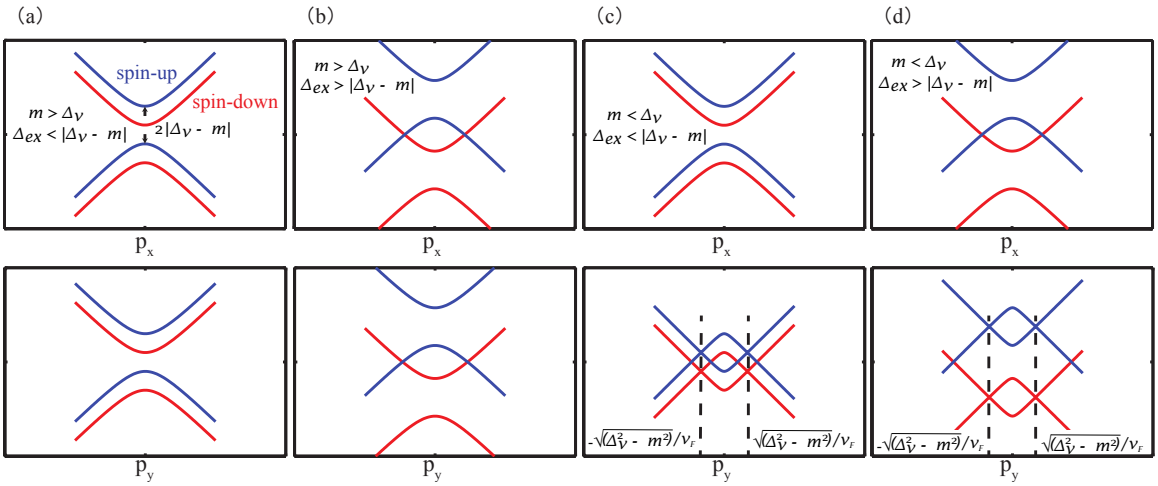

Figure 6.2: (Color online) Band dispersions in the absence of spin-orbit coupling for different values of m, Δ_{ex}, and Δ_v. (a) $m > \Delta_v$ and $\Delta_{ex} < |\Delta_v - m|$, (b) $m > \Delta_v$ and $\Delta_{ex} > |\Delta_v - m|$, (c) $m < \Delta_v$ and $\Delta_{ex} < |\Delta_v - m|$, and (d) $m < \Delta_v$ and $\Delta_{ex} > |\Delta_v - m|$.

Relation between m and Δ_v	value for Δ_{ex}	band dispersion along p_x	band dispersion along p_y
$m > \Delta_v$	$\Delta_{ex} < m - \Delta_v$ in Fig. 6.2(a)	parabolic, spin splitting	parabolic, spin splitting
	$m - \Delta_v < \Delta_{ex}$ in Fig. 6.2(b)	parabolic with an overlap between spin-up and spin-down bands	parabolic with an overlap between spin-up and spin-down bands
$m < \Delta_v$	$\Delta_{ex} < \|m - \Delta_v\|$ in Fig. 6.2(c)	parabolic with spin splitting	two Dirac cones with spin splitting
	$\Delta_{ex} > \|m - \Delta_v\|$ in Fig. 6.2(d)	parabolic with an overlap between spin-up and spin-down bands	a larger overlap between the spin-up and spin-down double Dirac cones

Table 6.1: Description of band dispersions in the absence of spin-orbit coupling for different parameters of Eq. (6.1). Plots of the dispersions corresponding to different relative strengths of the model parameters are shown in Fig. 6.2

struct a model Hamiltonian that captures the effect of these inter-valley interaction terms, and we analyze their effect on the band dispersion.

6.3.1 Inter-Valley Interactions

The following model Hamiltonian that acts on an 8 component spinor is consistent with the lattice symmetries, and it describes the salient features of the band dispersion near the $\mathbf{\Gamma}$ point in the absence of spin-orbit coupling.

$$H_0 = \hbar v_F(\hat{\sigma}_x\hat{\tau}_z p_x + \hat{\sigma}_y p_y) + \Delta_{ex}\hat{s}_z + \Delta_v\hat{\tau}_x + m\hat{\sigma}_x\hat{\tau}_x \tag{6.1}$$

In Eq. (6.1), $\hat{\tau}_i$, $\hat{\sigma}_i$ and $\hat{s}_i$ are the standard Pauli matrices acting on the valley, sublattice, and spin degree of freedom, respectively. The first term is the standard low-energy Hamiltonian describing the linear dispersion of the Dirac bands in graphene at the two valleys $\tau_z = \pm 1$ that are now folded to $\mathbf{\Gamma}$. The second term is the exchange coupling term induced by the magnetic moment of the Eu atom resulting in proximity induced exchange splitting Δ_{ex} between the spins. The last two terms of Eq. (6.1) capture the influence of the Eu atoms on the graphene layer. In both the heterostructures of Fig. 6.1(c,d), Eu atoms can sit on a C-C bond, referred as the bridge site, and in the middle of the hexagon, referred as the hollow site. The position of the bridge Eu atom reduces the graphene lattice symmetry from $C_{3v} \rightarrow C_{2v}$ resulting in the term $\Delta_v\tau_x$ in Eq. (6.1). This term corresponds to a valley pseudospin Zeeman term in x-direction [114] and shifts the Dirac cones from $\mathbf{\Gamma} = (0, 0)$ to $(0, \pm\Delta_v/m)$. The last term, $m\hat{\sigma}_x\hat{\tau}_x$ results from the Eu atom sitting at the hollow site of a graphene hexagon; we refer to it as an inter-valley scattering term. This term opens up

a trivial gap at $\mathbf{\Gamma}$ and works against the topological transition to a non-trivial state. The combined result of these terms, along with the relative strengths of Δ_{ex}, Δ_v, and m, give a rich band dispersion and also account for the differences in the band dispersions of the two heterostructures that we explore next.

The difference in the band dispersions of the two heterostructures is related to the relative magnitudes of Δ_{ex}, Δ_v, and m. The energy dispersion of the model Hamiltonian H_0 is

$$E_{\pm} = \pm\Delta_{ex} \pm \sqrt{m^2 + v_F^2|p|^2 + \Delta_v^2 \pm 2\Delta_v\sqrt{m^2 + v_F^2 p_y^2}}, \tag{6.2}$$

where $|p| = \sqrt{p_x^2 + p_y^2}$. For $\Delta_{ex} = 0$ the band dispersion has two important features, if $m \geq \Delta_v$ the dispersion is elliptical and gapped at $\mathbf{\Gamma}$ ($p_x = p_y = 0$), with an energy gap $2|\Delta_v - m|$. In contrast when $\Delta_v > m$ the Dirac points shift from $\mathbf{\Gamma}$ to $(0, \pm\sqrt{\Delta_v^2 - m^2}/v_F)$ and graphene retains its semi-metallic structure with two Dirac cones at $(0, \pm\sqrt{\Delta_v^2 - m^2}/v_F)$. For $\Delta_{ex} \neq 0$ and $m \geq \Delta_v$, there are three possibilities determined by the relative magnitudes of Δ_{ex} and $|\Delta_v - m|$. When (a) $\Delta_{ex} < |m - \Delta_v|$, there is a clear gap between the spin resolved states in Fig. 6.2(a). For (b) $\Delta_{ex} > |m - \Delta_v|$, the band dispersion exhibits an overlap between spin-up and spin-down bands shown in Fig. 6.2(b). Finally, at the transition point between scenarios (a) and (b) when $\Delta_{ex} = |m - \Delta_v|$, the elliptical bands touch. This indicates that when $m \geq \Delta_v$ there a is critical value of $\Delta_{ex} > |m - \Delta_v|$ at which the spin resolved states intersect. On the other hand, if $\Delta_{ex} \neq 0$ and $\Delta_v > m$, the shifted Dirac points which now appear at $(0, \pm\sqrt{\Delta_v^2 - m^2}/v_F)$ exhibit crossing of spin-resolved bands indicating that spin-resolved bands cross for any value of $\Delta_{ex} \neq 0$. The gap at $\mathbf{\Gamma}$ also depends on the relation between Δ_{ex} and $|\Delta_v - m|$. When $\Delta_{ex} < |\Delta_v - m|$, the band structure is shown

in Fig. 6.2(c), and the case of $\Delta_{ex} > |\Delta_v - m|$ is shown in Fig. 6.2(d). Now that we have established the conditions for the intersection of spin resolved bands, we explore the results of spin-orbit coupling on the graphene/EuO heterostructures.

6.3.2 Spin-Orbit Coupling

Spin-orbit coupling introduces two additional terms consistent with the lattice symmetries,

$$H_{\mathrm{SOC}} = \frac{\lambda_R}{2}(\hat{\sigma}_x \hat{s}_y \hat{\tau}_z - \hat{\sigma}_y \hat{s}_x) + \lambda_I \hat{\sigma}_z \hat{\tau}_z. \tag{6.3}$$

The first term is the Rashba spin-orbit coupling which breaks inversion symmetry in the plane perpendicular to the graphene sheet. Hence, $\lambda_R = 0$ in the aligned structure. The second term is the intrinsic spin-orbit term that breaks time reversal symmetry. Therefore $\lambda_I \neq 0$ for both structures. Since in-plane inversion symmetry is preserved in both structures, we neglect the Dresselhaus spin-orbit coupling. Our calculations indicate that the strength of the spin-orbit coupling represented by λ_R and λ_I is always smaller than m, Δ_V and Δ_{ex}, so we restrict our discussions to this case. For $\lambda_R, \lambda_I < m, \Delta_V, \Delta_{ex}$, the spin-orbit coupling introduces gaps between spin-resolved bands whenever they intersect (for example see Fig. 6.2 (b),(c) and (d)). With the addition of spin-orbit coupling the band dispersion becomes gapped, and the bands are a linear combination of spin-up and spin-down states.

By fitting the band dispersion with spin-orbit coupling obtained from the *ab initio* calculations shown in Fig. 6.7, we determine the best fit parameters for our model Hamiltonian. This gives $\hbar v_F = 3.5$ eV$\cdot$ Å, $\Delta_{ex} = 80$ meV, $m = 48$ meV, $\Delta_v = 17$ meV, $\lambda_R = 5$ meV, and $\lambda_I = 1$ meV. The band dispersion along the path $\mathbf{\Gamma} - \mathbf{K}$ calculated from the model

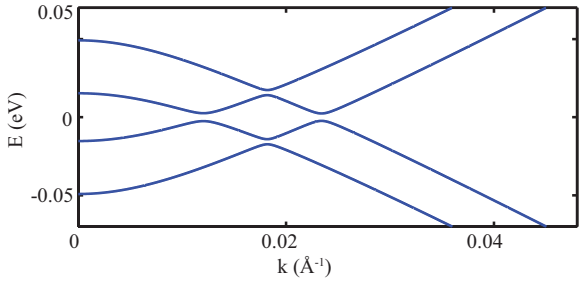

Figure 6.3: Band dispersion with spin-orbit coupling of Eu-misaligned structure calculated from model Hamiltonian H along the path $\mathbf{\Gamma}$ to $\mathbf{K}$ using parameters obtained from *ab initio* calculations. $\hbar v_F = 3.5$ eV$\cdot$ Å, $\Delta_{ex} = 80$ meV, $m = 48$ meV, $\Delta_v = 17$ meV, $\lambda_R = 5$ meV, and $\lambda_I = 1$ meV.

Hamiltonian $H = H_0 + H_{\text{SOC}}$ is shown in Fig. 6.3. The model Hamiltonian captures all four anti-crossing gaps at about the same position in momentum space. Next, we study the topological properties of these bands obtained from H and calculate the Hall conductance for a range of band parameters.

6.4 Quantized Anomalous Hall Effect in Graphene/EuO Heterostructures

In Ref. [106], Qiao et. al. found that ferromagnetic graphene in the presence of Rashba spin-orbit coupling shows the QAH effect with $\sigma_{xy} = 2e^2/h$. First principle calculations also demonstrated that this QAH phase can be engineered by doping with $3d$ or $5d$ transition-metal atoms or the proximity of a layered antiferromagentic insulator. In all cases studies thus far, the low energy bands are at the $\mathbf{K}$ and $\mathbf{K}'$ points of the hexagonal BZ, and the Hall conductance in the gap is quantized $\sigma_{xy} = 2e^2/h$ as long as $\lambda_R \neq 0$ and $\Delta_{ex} \neq 0$. In the graphene/EuO heterostructure, as shown in sections II and III, the low-energy bands are no longer at $\mathbf{K}$ and $\mathbf{K}'$ but at $\mathbf{\Gamma}$, and inter-valley interactions

significantly modify the band dispersion and hence the topological properties of the bands. Therefore, we now analyze the effect of inter-valley interactions on the topological properties of graphene/EuO structures in the presence of in-plane inversion symmetry.

The Hall conductance is calculated from the integral of the Berry curvature over the BZ of the occupied bands and can be expressed as

$$\sigma_{xy} = \frac{e^2}{\hbar} \sum_{\alpha} \int_{BZ} \frac{d^2p}{(2\pi)^2} \Theta(E_F - \epsilon_\alpha(\mathbf{p}))\Omega_\alpha(\mathbf{p}), \tag{6.4}$$

where α corresponds to the band index, E_F denotes the Fermi energy, $\epsilon_\alpha(\mathbf{p})$ is the energy eigenstate, and $\Omega_\alpha(\mathbf{p})$ is the Berry curvature of the α^{th} band. The Berry curvature in terms of the band eigenstates can be expressed as

$$\Omega_\alpha(\mathbf{p}) = \mathrm{Im} \sum_{\beta \neq \alpha} \left[\epsilon_{ij} \frac{\langle u_\alpha | \partial H(\mathbf{p})/\partial p_i | u_\beta \rangle \langle u_\beta | \partial H(\mathbf{p})/\partial p_j | u_\alpha \rangle}{(\epsilon_\beta(\mathbf{p}) - \epsilon_\alpha(\mathbf{p}))^2} \right], \tag{6.5}$$

where the Einstein summation convention is used for the Roman indices i and j, ϵ_{ij} is the anti-symmetric tensor, and $u_\alpha(\mathbf{p})$ is the α^{th} band eigenstate. It is instructive to note that in-plane inversion symmetry dictates $\Omega_\alpha(\mathbf{p}) = \Omega_\alpha(-\mathbf{p})$ and time reversal symmetry imposes $\Omega_\alpha(\mathbf{p}) = -\Omega_\alpha(-\mathbf{p})$. For graphene/EuO heterostructures time reversal symmetry is broken due to exchange splitting caused by the ferromagnetic substrate, however in-plane inversion symmetry is preserved. We take advantage of the in-plane inversion symmetry by calculating the Berry curvature in the upper half-plane $p_y > 0$ and multiplying by a factor of 2 to account for the lower half-plane $p_y < 0$. The Berry curvature is calculated numerically.

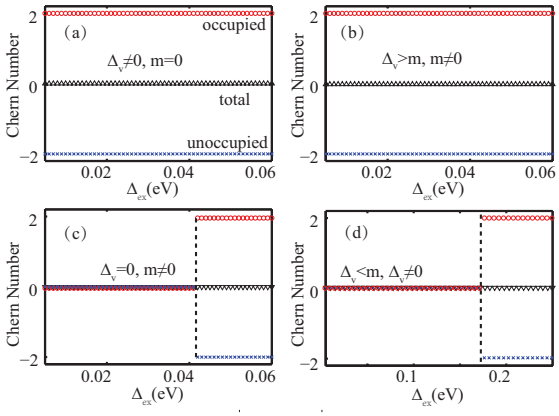

Figure 6.4: (Color online) The Chern number calculated as a function of Δ_{ex} for 4 different cases of Δ_v and m. The red open circles show the Chern number of the occupied bands, the blue 'x' symbols show the Chern number of the unoccupied bands, and the black triangles show the Chern number of the summation of all bands. The Chern number of the occupied bands is 2 for all values satisfying (a) $\Delta_v \neq 0$, $m = 0$ and (b) $\Delta_v > m$, $m \neq 0$. For condition (c), $\Delta_v = 0$, $m \neq 0$, the Chern number of the occupied bands becomes 2 for $\Delta_{ex} \geq m$. For this example, m is chosen to be 0.04 eV. (d) For $\Delta_v \neq 0$ and $m > \Delta_v$, (in this example $\Delta_v = 0.01$ eV and $m = 0.04$ eV) the topological transition is pushed to a higher value of $\Delta_{ex} = 0.165$ eV.

Our calculations satisfy that the sum of the Berry curvatures over all the bands is zero at every $\mathbf{p}$ point in the BZ, as expected from Eq. (6.5).

The model Hamiltonian H only captures the low-energy bands near $\mathbf{\Gamma}$ and may not be valid over the full BZ of the graphene/EuO heterostructure. The Berry curvature calculated using (6.5) falls rapidly away from the $\mathbf{\Gamma}$ point. This allows us to restrict our calculations of the Hall conductance to a neighborhood of $\mathbf{\Gamma}$. It is well known that when the Fermi energy lies in the gap σ_{xy} is quantized and the Hall conductance at zero temperature can be expressed as

$$\sigma_{xy} = \frac{e^2}{h} \sum_{\alpha}{}' C_\alpha, \tag{6.6}$$

where the prime indicates summation over the occupied bands, and C_α is the Chern number of the α^{th} band that we calculate for different parameters of our model Hamiltonian H. We next discuss the Chern numbers at $E_F = 0$ for the occupied and unoccupied bands.

The calculations for the Chern numbers were performed for 4 different cases with fixed values for λ_R, m, and Δ_v (with $\lambda_R < m,\ \Delta_v$) as a function of Δ_{ex}. For this case, λ_I is not considered. The four different cases are depicted in Fig. 6.4(a)-(d). Figs. 6.4(a) and (b) show the results when $\Delta_v > m$. In this case the Chern number is quantized and gives a Hall conductance $\sigma_{xy} = 2e^2/h$ for any value of $\lambda_R \neq 0$. However, when $\Delta_v < m$ and $m \neq 0$, there is a topological transition as a function of Δ_{ex} and the Chern number changes from 0 to 2 as shown in Figs. 6.4(c,d). For $\Delta_v = 0$, the transition occurs when $\Delta_{ex} \geq m$ as shown in Fig. 6.4(c). For $\Delta_v \neq 0$ and $m > \Delta_v$, the transition is pushed to a higher value of Δ_{ex} as shown in Fig. 6.4(d). For both (c) and (d), $m = 0.04$ eV. In (d), $\Delta_v = 0.01$ eV, and the transition occurs at $\Delta_{ex} = 0.165$ eV. Unfortunately, we have been unable to find an

analytical expression for the topological transition for $\Delta_v < m$. From the calculations, we conclude that the Chern number is 2 for the case of $\Delta_v > m$ and that the system undergoes a topological transition for $\Delta_v < m$ as a function of Δ_{ex}.

The results can be summarized in terms of the phase diagram shown in Fig. 6.5. In this calculation, $\lambda_R = 5$ meV, $\Delta_{ex} = 80$ meV and $\lambda_I = 1$ meV are constant, and the behavior of Chern number is calculated as a function of both the magnitude of the valley pseudospin Zeeman term Δ_v and the inter-valley scattering term m. As shown in Fig. 6.5, when $\Delta_v > m$, the Chern number is always 2 giving a Hall conductance $\sigma_{xy} = 2e^2/h$. At small values of Δ_v, a more complicated situation occurs in the region $m > \Delta_v$ of the phase diagram, however, for sufficiently large values of Δ_v, the phase transition occurs at $m > \Delta_v$ for a fixed value of Δ_{ex}. The red triangle shows the values for the band structure from Fig. 6.3 fitted to the *ab initio* calculation shown in Fig. 6.7. Even with EuO placed on both sides of the graphene providing a large proximity exchange coupling of 80 meV, the trivial gapping from the inter-valley scattering term, $m = 48$ meV, prevents the band structure from crossing over to a topologically non-trivial state.

6.5 First Principle Calculations

The band dispersions of the EuO/graphene/EuO heterostructures are calculated using the Vienna *ab initio* simulation package (VASP) [47–49] in the projected-augmented-wave method [50]. The generalized gradient approximation (GGA) of the Perdew-Burke-Ernzerhof form [32–34] is used for the exchange correlation energy, and a Hubbard-U correction is used for the magnetic insulator, EuO. The on-site Coulomb repulsion and exchange

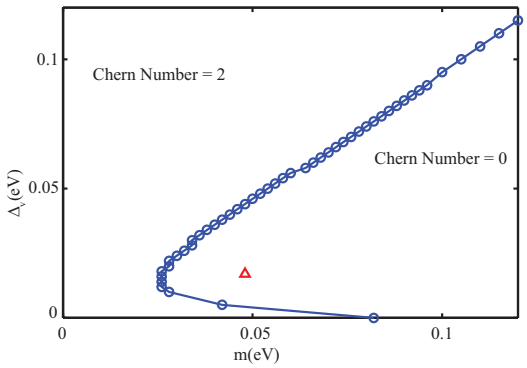

Figure 6.5: Phase diagram as a fucntion of m and Δ_v for fixed values of $\lambda_R = 5$ meV, $\lambda_I = 1$ meV and $\Delta_{ex} = 80$ meV. The red triangle in the figure represents the fitted band structure shown in Fig. 6.3. The curve indicates the phase boundary between a Chern number of 2 on the left side of the curve and 0 on the right side of the curve.

interactions on the Eu atom $4f$ orbital are 8.3 eV and 0.77 eV, respectively, and on the O atom $2p$ orbital, they are 4.6 eV and 1.2 eV, respectively. [115] The kinetic energy cutoff is 520 eV for all calculations. During all structural relaxations, the convergence tolerance on the Hellmann-Feynman forces is less than 0.03 eV Å. An $8 \times 8 \times 8$ Monkhorst-Pack k-point mesh is used for bulk EuO. The calculated bulk lattice constant is 5.186 Å which is very close to the previously published first principle calculations [112] and consistent with the experimental results. The lattice constant a_0 of graphene is 2.46 Å. This results in a lattice mismatch of less than 1% in the $3a_0 \times 3a_0$ unit cells shown in Figs. 6.1(c,d).

The EuO/graphene/EuO structures consist of graphene between the (111) Eu planes of EuO. The heterostructure with graphene on the Eu-terminated surface is more stable than graphene on the O-terminated surface. [112] The relaxation of the 2D heterostructures uses the same level of theory, cutoffs, and tolerances as described in the previous paragraph with a Monkhorst-Pack k-point grid of $4 \times 4 \times 1$. A vacuum buffer space over 25 Å is included to prevent interaction between adjacent slabs and hydrogen atoms

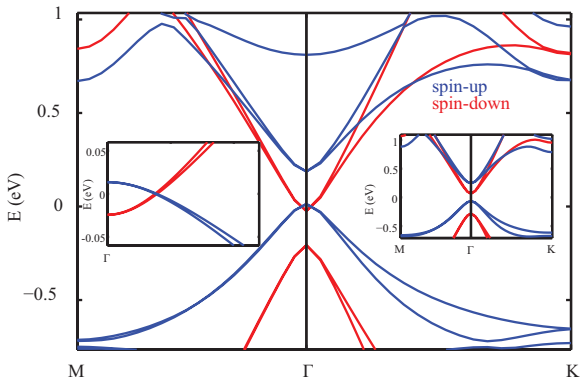

Figure 6.6: (Color online) Band structure of the Eu-misaligned structure without spin-orbit coupling. Left inset: close-up of the low-energy band structure of the misaligned structure near **Γ**. Right inset: Band structure of the Eu-aligned structure.

passivate the outer oxygen layers of the EuO films. The relaxed vertical spacing between the Eu and C layers is 2.517 Å for the misaligned structure of Fig. 6.1(c) and 2.555 Å for the aligned structure of Fig. 6.1(d). These distances are close the value of 2.57 Å found previously for a single-sided heterostructure of graphene on EuO. [112]

6.5.1 Band Dispersion without Spin-Orbit Coupling

Fig. 6.6 shows the calculated band dispersion in the absence of spin-orbit coupling for the misaligned structure of Fig. 6.1(c), and the right inset shows the band dispersion for the aligned structure of Fig 6.1(d). Both band dispersions are calculated

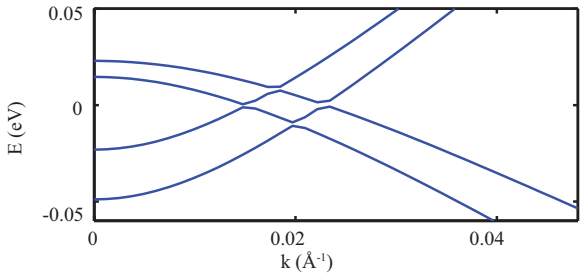

Figure 6.7: (Color online) Band structure with spin-orbit coupling of Eu-misaligned structure calculated along the path **Γ** to **K** where **K** is 0.57 Å^{-1} away from **Γ**.

along the path $\mathbf{M} - \mathbf{\Gamma} - \mathbf{K}$ of the commensurate BZ of the $3N \times 3N$ graphene lattice. $\mathbf{K} = (2\pi/3a, 2\sqrt{3}\pi/3a, 0)$, $\mathbf{M} = (0, \frac{2\pi}{\sqrt{3}a}, 0)$, and $a = 7.38$ Å is the lattice constant of the heterostructure unit cell. The most striking difference in the two band dispersions is the presence of a gap between the spin-resolved bands of the aligned heterostructure, whereas in the misaligned heterostructure the spin-up and spin-down bands intersect. The calculated values of gaps for both heterostructures are tabulated in Table 6.2. The energy bandgap is denoted by E_G. The gap between the spin-up electron band and spin-up hole band is $\Delta_\uparrow$, and the gap between spin-down bands is $\Delta_\downarrow$. The spin-splitting of the electron and hole bands are δ_e and δ_h, respectively. In Table 6.2 and Fig. 6.6, the positive value of $E_G = 127$ meV indicates a bandgap between conduction and valence band, whereas the negative value of $E_G = -38$ meV indicates a spin resolved band overlap. The values of $\Delta_\uparrow$ and $\Delta_\downarrow$ in the misaligned structure are half of their values in the aligned structure. Another striking feature of the calculated band dispersion is that the low-energy bands of the combined heterostructures appear at $\mathbf{\Gamma}$ and have curvature. In contrast, to the *ab initio* studies of a graphene/$BiFeO_3$ heterostructure, [111] the Dirac cones are no longer at the **K** and **K**' points, but at $\mathbf{\Gamma}$, consistent with earlier first principle studies of graphene/EuO heterostructures. [112] This is due to band folding.

Structure	E_G (meV)	$\Delta_\uparrow$ (meV)	$\Delta_\downarrow$ (meV)	δ_e (meV)	δ_h (meV)
Eu aligned	127	309	344	182	217
Eu misaligned	-38	173	182	211	220

Table 6.2: Energy gaps of the EuO-graphene-EuO structures at the Dirac point. E_G is the bandgap of the gapped Dirac cone. $\Delta_\uparrow$ is the spin-up gap, and $\Delta_\downarrow$ is the spin-down gap. The spin-splitting of the electron and hole bands at $\mathbf{\Gamma}$ are δ_e and δ_h, respectively.

6.5.2 Band Dispersion with Spin-Orbit Coupling

Our *ab initio* calculations that include spin-orbit coupling show very different behaviors of the spin resolved bands in the two heterostructures. Since the spin-resolved bands intersect in the misaligned heterostructure, the addition of spin-orbit coupling in this system will be more pronounced than in the aligned heterostructure. In the aligned heterostructure spin-orbit coupling leads to a small splitting of the spin resolved bands and the dispersion remains gapped, therefore, we focus on the effect of spin-orbit coupling in the misaligned heterostructure.

In Fig. 6.7, we plot the band dispersion of the Eu-misaligned heterostructure along path $\mathbf{\Gamma} - \mathbf{K}$. Fig. 6.7 shows that spin-orbit coupling breaks the degeneracy of the bands shown in the left inset of Fig. 6.6 and gaps the bands. The conduction bands and the valence bands split by 8 meV and 26 meV at the $\mathbf{\Gamma}$ point, respectively. There are two local minimum gaps between the conduction band and valence band in the band dispersion near $\mathbf{\Gamma}$ with values of 0.1 and 0.3 meV, respectively. The gap between the two conduction bands is 0.2 meV; while the gap between the two valance bands is 1.2 meV.

6.6 Conclusions and Outlook

Using insights from first principle calculations and lattice symmetries, we constructed a model Hamiltonian to describe commensurate graphene/EuO heterostructures. In commensurate graphene/EuO structures band folding maps the Dirac cones to the $\mathbf{\Gamma}$ point of the hexagonal super-lattice BZ of the combined heterostructures. Apart from inducing proximity exchange splitting in the graphene bands, the Eu atoms also introduce

two distinct types of inter-valley interactions, a valley pseudospin Zeeman term and an inter-valley scattering term, whose strengths are captured by two model parameters Δ_v and m. The combined effect of exchange and inter-valley interactions results in a non-linear dispersion at the $\mathbf{\Gamma}$ point which is captured by the model Hamiltonian. The parameters of the model Hamiltonian are determined by fitting to the band dispersion obtained from the *ab initio* calculations.

Using the model Hamiltonian with Rashba spin-orbit coupling, exchange, and inter-valley interactions we calculate the band dispersion and the topological properties of the commensurate graphene/EuO heterostructures. The inter-valley interactions can significantly influence the topological properties of the bands for non-zero Rashba ($\lambda_R \neq 0$) and exchange splitting ($\Delta_{ex} \neq 0$). For $\Delta_v > m$ with $\lambda_R,\ \Delta_{ex} \neq 0$, the commensurate graphene/EuO heterostructure is a Chern insulator with a Hall conductance $\sigma_{xy} = 2e^2/h$, whereas for small Δ_v with $m > \Delta_v$, the phase diagram becomes more complicated and one needs a large exchange splitting or Rashba spin-orbit coupling to realize the Chern insulating phase. Our calculations indicate that even in the presence of in-plane inversion symmetry, inter-valley interactions can significantly influence the topological properties of graphene/EuO heterostructures.

For a random incommensurate crystallographic stacking of graphene on EuO, the inter-valley coupling will be negligible since the Dirac cones will remain at $\mathbf{K}$ and $\mathbf{K}'$. However, since any incommensurate stacking will break the in-plane inversion symmetry of the graphene layer, the model Hamiltonian H would acquire an additional term $M\hat{\sigma}_z$. [114] In this case the topological properties will depend on the relative strength of M and

$\Delta_{gap} < \min(\lambda_R, \Delta_{ex})$. The system will exhibit a QAH effect with a Chern number 2 only if $M < \Delta_{gap}$.

To observe the QAH effect in graphene/ferromagnet heterostructures, it is important that the disorder induced broadening Σ of the bands be smaller than the topological bandgap Δ_{gap}. The critical temperature required to observe the QAH effect is proportional to the mobility gap defined as $\Delta_{gap} - \Sigma$, which must be positive. In order to increase the topological gap Δ_{gap}, it is important to have a large Rashba spin-orbit coupling λ_R, which is small ~ 7 meV in our calculations. The Rashba spin-orbit coupling can in principle be enhanced by hydrogenation or deposition of heavy adatoms on the graphene surface. [116] Even for negative values of the mobility gap ($\Delta_{gap} - \Sigma < 0$), the graphene/ferromagnetic structures will exhibit an unquantized anomalous Hall effect. However, in this case the anomalous hall effect will be additionally influenced by disorder induced extrinsic effects [117] like side-jump and skew scattering mechanisms which are beyond the scope of this study.

Chapter 7

Conclusions

There is growing interest in the fabrication and characterization of different van der Waals (vdW) materials and vdW heterostructures composed of two-dimensional (2D) materials. The heterostructure composed of 2D materials are very attractive since the interfaces are self-passivated and devoid of dangling bonds. In this dissertation, we studied the electric field, strain and magnetic proximity effect in four different 2D heterostructures, $WSe_2/MoSe_2$, $HfSe_2/SnS_2$, $PtSe_2/SnS_2$ and EuO/graphene/EuO. Chapter 3 discusses the electronic structures of $WSe_2/MoSe_2$ with two different thicknesses, monolayer $MoSe_2$ with monolayer WSe_2, and monolayer $MoSe_2$ with bilayer WSe_2. Both heterostructures are intrinsic type II heterojunctions; the monolayer/monolayer is direct bandgap, and the monolayer/bilayer heterostructure is indirect bandgap. Electric field can be used to tune the electronic structures of both $WSe_2/MoSe_2$ heterostructures from indirect to direct bandgap. It can also tune the monolayer/bilayer heterostructure from type II to type I heterojunction.

Chapter 4 focuses on the study of electronic structures of $HfSe_2/SnS_2$. Monolayer $HfSe_2$ and SnS_2 are closely lattice matched; the heterostructure composed by the two materials shows a coherent superposition of the conduction band wavefunctions of the individual layers at CBM. As the applied electric field is ramped from negative to positive, the heterojunction formed in the heterostructure can be tuned from type II to type I, and the CBM would change from mainly localize on SnS_2 to $HfSe_2$. Graphene on $HfSe_2/SnS_2$ results in n-type $HfSe_2/SnS_2$ and p-type graphene. The Fermi level aligns below the CBM of $HfSe_2/SnS_2$, therefore, graphene on $HfSe_2/SnS_2$ forms negative Schottky barrier and has very low contact resistance.

The electronic structures of $PtSe_2/SnS_2$ are studied in Chapter 5. Monolayer $PtSe_2$ and SnS_2 are closely lattice matched and can form AA and AB stacked heterostructures. The heterostructures formed by the two materials are indirect band gap with CBM at **M** and valence bands showing a Mexican hat. The bands tructures of $PtSe_2/SnS_2$ can be tuned significantly by in-plane biaxial strain. A transition from semiconducting to metallic has been observed under compressive strain, while the VBM moves to $\mathbf{\Gamma}$. The tensile strain enhances the Mexican hat and the height of hat increases to over six times of the value without strain. Graphene on $PtSe_2/SnS_2$ also results in n-type $PtSe_2/SnS_2$ and p-type graphene. Only the configurations of graphene on contact with SnS_2 form negative Schottky barrier.

The magnetic proximity effect in heterostructure composed of graphene is in Chapter 6. Using insights from first principle calculations and lattice symmetries, a model Hamiltonian is created to describe the behavior of graphene sandwiched by two EuO monolayers.

we found that two distinct types of inter-valley interactions, pseudo valley Zeeman term and inter-valley scattering term, can significantly change the topological feature of the system.

Appendix A

Band Structures of $HfSe_2/SnS_2$ under Electric Fields

A.1 Band Structures of AA Stacked Heterostructure under Different Electric Fields

The AA stacked heterostructure can be tuned by applied electric field as shown in Fig. A.1. From Fig. A.1, we can see that from negative electric field to positive electric field, the conduction band minimum (CBM) switching from SnS_2 to $HfSe_2$. In the meantime, the second lowest conduction band, the composition switches from $HfSe_2$ to SnS_2. The weights of the main contributed layer at CBM and the second lowest conduction band are all listed in Fig. A.1.

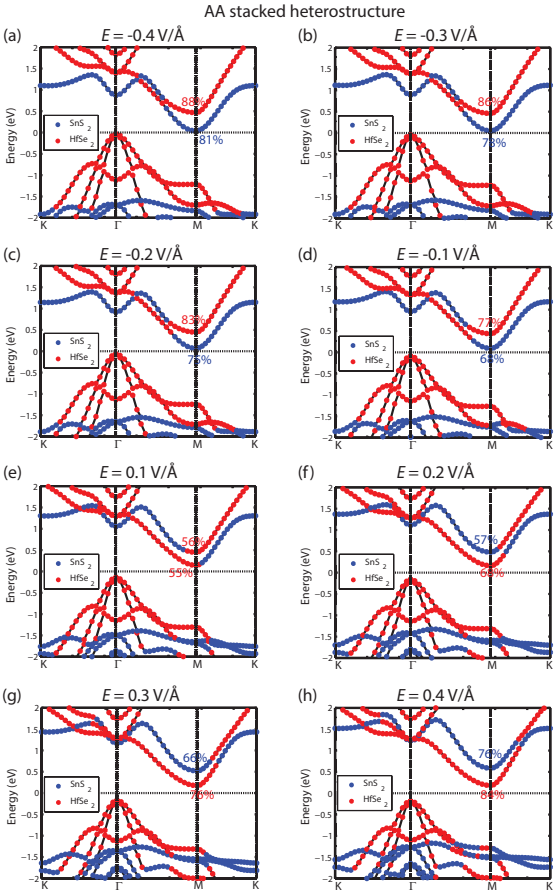

Figure A.1: Band structures of AA stacked heterostructure under different electric fields. (a) -0.4 V/Å, (b) -0.3 V/Å, (c) -0.2 V/Å, (d) -0.1 V/Å, (e) 0.1 V/Å, (f) 0.2 V/Å, (g) 0.3 V/Å, and (h) 0.4 V/Å.

A.2 Band Structures of AB Stacked Heterostructure under Different Electric Fields

Similar to AA stacked heterostructure, AB stacked heterostructure is also sensitive to electric field. The switch of CBM and second lowest conduction band can also be found in AB stacked heterostructure.

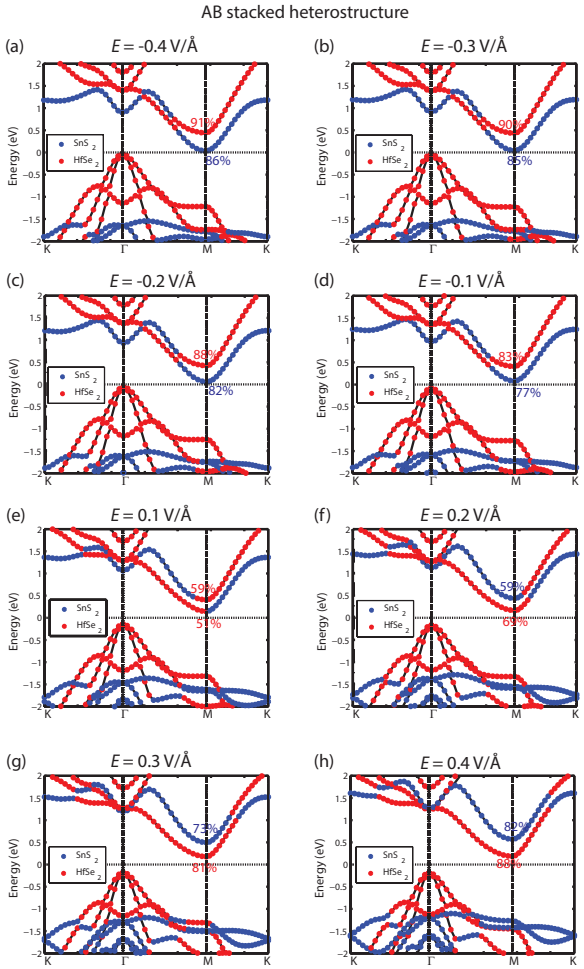

Figure A.2: Band structures of AB stacked heterostructure under different electric fields. (a) -0.4 V/Å, (b) -0.3 V/Å, (c) -0.2 V/Å, (d) -0.1 V/Å, (e) 0.1 V/Å, (f) 0.2 V/Å, (g) 0.3 V/Å, and (h) 0.4 V/Å.

Bibliography

[1] Shanshan Su, Protik Das, Supeng Ge, and Roger K. Lake. Graphene contacts to a hfse2/sns2 heterostructure. *Journal of Chemical Physics*, 146(6):064701, 2017.

[2] Shanshan Su, Yafis Barlas, Junxue Li, Jing Shi, and Roger K. Lake. Effect of intervalley interaction on band topology of commensurate graphene/euo heterostructures. *Phys. Rev. B*, 95:075418, Feb 2017.

[3] Gianluca Fiori, Francesco Bonaccorso, Giuseppe Iannaccone, Tomás Palacios, Daniel Neumaier, Alan Seabaugh, Sanjay K Banerjee, and Luigi Colombo. Electronics based on two-dimensional materials. *Nature nanotechnology*, 9(10):768–779, 2014.

[4] Victor V Zhirnov, Ralph K Cavin, James A Hutchby, and George I Bourianoff. Limits to binary logic switch scaling-a gedanken model. *Proceedings of the IEEE*, 91(11):1934–1939, 2003.

[5] Mingsheng Xu, Tao Liang, Minmin Shi, and Hongzheng Chen. Graphene-like two-dimensional materials. *Chemical reviews*, 113(5):3766–3798, 2013.

[6] Dmitri Golberg, Yoshio Bando, Yang Huang, Takeshi Terao, Masanori Mitome, Chengchun Tang, and Chunyi Zhi. Boron nitride nanotubes and nanosheets. *ACS nano*, 4(6):2979–2993, 2010.

[7] Robert W Keyes. The electrical properties of black phosphorus. *Physical Review*, 92(3):580, 1953.

[8] Darshana Wickramaratne, Ferdows Zahid, and Roger K Lake. Electronic and thermoelectric properties of few-layer transition metal dichalcogenides. *The Journal of chemical physics*, 140(12):124710, 2014.

[9] Darshana Wickramaratne, Ferdows Zahid, and Roger K Lake. Electronic and thermoelectric properties of van der waals materials with ring-shaped valence bands. *Journal of Applied Physics*, 118(7):075101, 2015.

[10] Michael Naguib, Vadym N Mochalin, Michel W Barsoum, and Yury Gogotsi. 25th anniversary article: Mxenes: a new family of two-dimensional materials. *Advanced Materials*, 26(7):992–1005, 2014.

[11] Haijun Zhang, Chao-Xing Liu, Xiao-Liang Qi, Xi Dai, Zhong Fang, and Shou-Cheng Zhang. Topological insulators in bi2se3, bi2te3 and sb2te3 with a single dirac cone on the surface. *Nature physics*, 5(6):438–442, 2009.

[12] Hao Tang, Dong Liang, Richard LJ Qiu, and Xuan PA Gao. Two-dimensional transport-induced linear magneto-resistance in topological insulator bi2se3 nanoribbons. *Acs Nano*, 5(9):7510–7516, 2011.

[13] Haifeng Wang, Yan Gao, and Gang Liu. Anisotropic phonon transport and lattice thermal conductivities in tin dichalcogenides sns 2 and snse 2. *RSC Advances*, 7(14):8098–8105, 2017.

[14] Lina Wang, Ying Ma, Min Yang, and Yanxing Qi. One-pot synthesis of 3d flower-like heterostructured sns 2/mos 2 for enhanced supercapacitor behavior. *Rsc Advances*, 5(108):89069–89075, 2015.

[15] Le Huang, Yan Li, Zhongming Wei, and Jingbo Li. Strain induced piezoelectric effect in black phosphorus and MoS_2 van der waals heterostructure. *Scientific Reports*, 5:16448, 2015.

[16] KS Novoselov, A Mishchenko, A Carvalho, and AH Castro Neto. 2d materials and van der waals heterostructures. *Science*, 353(6298):aac9439, 2016.

[17] Matthew Yankowitz, Jiamin Xue, Daniel Cormode, Javier D Sanchez-Yamagishi, K Watanabe, T Taniguchi, Pablo Jarillo-Herrero, Philippe Jacquod, and Brian J LeRoy. Emergence of superlattice dirac points in graphene on hexagonal boron nitride. *Nature Physics*, 8(5):382–386, 2012.

[18] LA Ponomarenko, RV Gorbachev, GL Yu, DC Elias, R Jalil, AA Patel, A Mishchenko, AS Mayorov, CR Woods, JR Wallbank, et al. Cloning of dirac fermions in graphene superlattices. *Nature*, 497(7451):594–597, 2013.

[19] CR Dean, L Wang, P Maher, C Forsythe, F Ghahari, Y Gao, J Katoch, M Ishigami, P Moon, M Koshino, et al. Hofstadter/'s butterfly and the fractal quantum hall effect in moire superlattices. *Nature*, 497(7451):598–602, 2013.

[20] B Hunt, JD Sanchez-Yamagishi, AF Young, M Yankowitz, Brian J LeRoy, K Watanabe, T Taniguchi, P Moon, M Koshino, P Jarillo-Herrero, et al. Massive dirac fermions and hofstadter butterfly in a van der waals heterostructure. *Science*, 340(6139):1427–1430, 2013.

[21] GL Yu, RV Gorbachev, JS Tu, AV Kretinin, Y Cao, R Jalil, F Withers, LA Ponomarenko, BA Piot, M Potemski, et al. Hierarchy of hofstadter states and replica quantum hall ferromagnetism in graphene superlattices. *Nature physics*, 10(7):525–529, 2014.

[22] A. Avsar, J. Y. Tan, T. Taychatanapat, J. Balakrishnan, G. K. W. Koon, Y. Yeo, J. Lahiri, A. Carvalho, A. S. Rodin, E. C. T. OFarrell, G. Eda, A. H. Castro Neto, and B. zyilmaz. Spinorbit proximity effect in graphene. *Nat Commun*, 5:4875, 2014.

[23] Zhe Wang, Dong-Keun Ki, Hua Chen, Helmuth Berger, Allan H MacDonald, and Alberto F Morpurgo. Strong interface-induced spin-orbit coupling in graphene on WS_2. *Nat Commun*, 6:8339, 2015.

[24] Pierre Hohenberg and Walter Kohn. Inhomogeneous electron gas. *Physical review*, 136(3B):B864, 1964.

[25] Walter Kohn and Lu Jeu Sham. Self-consistent equations including exchange and correlation effects. *Physical review*, 140(4A):A1133, 1965.

[26] Stefan Grimme. Semiempirical gga-type density functional constructed with a long-range dispersion correction. *Journal of computational chemistry*, 27(15):1787–1799, 2006.

[27] Kl Terakura, AR Williams, T Oguchi, and J Kübler. Transition-metal monoxides: band or mott insulators. *Physical review letters*, 52(20):1830, 1984.

[28] SL Dudarev, GA Botton, SY Savrasov, CJ Humphreys, and AP Sutton. Electron-energy-loss spectra and the structural stability of nickel oxide: An lsda+ u study. *Physical Review B*, 57(3):1505, 1998.

[29] AI Liechtenstein, VI Anisimov, and J Zaanen. Density-functional theory and strong interactions: Orbital ordering in mott-hubbard insulators. *Physical Review B*, 52(8):R5467, 1995.

[30] Swastibrata Bhattacharyya and Abhishek K Singh. Semiconductor-metal transition in semiconducting bilayer sheets of transition-metal dichalcogenides. *Physical Review B*, 86(7):075454, 2012.

[31] Jochen Heyd, Gustavo E. Scuseria, and Matthias Ernzerhof. Hybrid functionals based on a screened coulomb potential. *The Journal of Chemical Physics*, 118(18):8207–8215, 2003.

[32] John P. Perdew, J. A. Chevary, S. H. Vosko, Koblar A. Jackson, Mark R. Pederson, D. J. Singh, and Carlos Fiolhais. Atoms, molecules, solids, and surfaces: Applications of the generalized gradient approximation for exchange and correlation. *Phys. Rev. B*, 46(11):6671–6687, 1992.

[33] Yue Wang and John P. Perdew. Correlation hole of the spin-polarized electron gas, with exact small-wave-vector and high-density scaling. *Phys. Rev. B*, 44(24):13298–13307, 1991.

[34] G. Kresse and D. Joubert. From ultrasoft pseudopotentials to the projector augmented-wave method. *Phys. Rev. B*, 59(3):1758–1775, 1999.

[35] Joachim Paier, Martijn Marsman, and Georg Kresse. Why does the b3lyp hybrid functional fail for metals? *The Journal of chemical physics*, 127(2):024103, 2007.

[36] Alexander V Kolobov and Junji Tominaga. *Two-Dimensional Transition-Metal Dichalcogenides*, volume 239. Springer, 2016.

[37] B Schönfeld, JJ Huang, and SC Moss. Anisotropic mean-square displacements (msd) in single-crystals of 2h-and 3r-mos2. *Acta Crystallographica Section B: Structural Science*, 39(4):404–407, 1983.

[38] Branimir Radisavljevic, Aleksandra Radenovic, Jacopo Brivio, i V Giacometti, and A Kis. Single-layer mos2 transistors. *Nature nanotechnology*, 6(3):147–150, 2011.

[39] Youngki Yoon, Kartik Ganapathi, and Sayeef Salahuddin. How good can monolayer mos2 transistors be? *Nano letters*, 11(9):3768–3773, 2011.

[40] Hui Fang, Steven Chuang, Ting Chia Chang, Kuniharu Takei, Toshitake Takahashi, and Ali Javey. High-performance single layered wse2 p-fets with chemically doped contacts. *Nano letters*, 12(7):3788–3792, 2012.

[41] Khairul Alam and Roger K Lake. Monolayer mos2 transistors beyond the technology road map. *IEEE transactions on electron devices*, 59(12):3250–3254, 2012.

[42] Han Liu, Adam T Neal, and Peide D Ye. Channel length scaling of mos2 mosfets. *ACS nano*, 6(10):8563–8569, 2012.

[43] Tianshu Li and Giulia Galli. Electronic properties of mos2 nanoparticles. *The Journal of Physical Chemistry C*, 111(44):16192–16196, 2007.

[44] C Ataca, H Sahin, E Akturk, and S Ciraci. Mechanical and electronic properties of mos2 nanoribbons and their defects. *The Journal of Physical Chemistry C*, 115(10):3934–3941, 2011.

[45] Di Xiao, Gui-Bin Liu, Wanxiang Feng, Xiaodong Xu, and Wang Yao. Coupled spin and valley physics in monolayers of mos 2 and other group-vi dichalcogenides. *Physical Review Letters*, 108(19):196802, 2012.

[46] Hiram J Conley, Bin Wang, Jed I Ziegler, Richard F Haglund Jr, Sokrates T Pantelides, and Kirill I Bolotin. Bandgap engineering of strained monolayer and bilayer mos2. *Nano letters*, 13(8):3626–3630, 2013.

[47] Georg Kresse and Jürgen Furthmüller. Efficient iterative schemes for ab initio total-energy calculations using a plane-wave basis set. *Phys. Rev. B*, 54(16):11169–11186, 1996.

[48] Georg Kresse and Jürgen Hafner. Ab initio molecular dynamics for liquid metals. *Phys. Rev. B*, 47(1):558–561, 1993.

[49] Georg Kresse and Jürgen Furthmüller. Efficiency of ab-initio total energy calculations for metals and semiconductors using a plane-wave basis set. *Computational Materials Science*, 6(1):15–50, 1996.

[50] Peter E Blöchl. Projector augmented-wave method. *Phys. Rev. B*, 50(24):17953–17979, 1994.

[51] Judith Harl, Laurids Schimka, and Georg Kresse. Assessing the quality of the random phase approximation for lattice constants and atomization energies of solids. *Phys. Rev. B*, 81(11):115126, 2010.

[52] Ning Lu, Hongyan Guo, Lei Li, Jun Dai, Lu Wang, Wai-Ning Mei, Xiaojun Wu, and Xiao Cheng Zeng. MoS2/MX2 heterobilayers: bandgap engineering via tensile strain or external electrical field. *Nanoscale*, 6(5):2879–2886, 2014.

[53] Gui-Bin Liu, Wen-Yu Shan, Yugui Yao, Wang Yao, and Di Xiao. Three-band tight-binding model for monolayers of group-VIB transition metal dichalcogenides. *Phys. Rev. B*, 88(8):085433, 2013.

[54] Gui-Bin Liu, Di Xiao, Yugui Yao, Xiaodong Xu, and Wang Yao. Electronic structures and theoretical modelling of two-dimensional group-VIB transition metal dichalcogenides. *Chem. Soc. Rev.*, 44(9):2643–2663, 2015.

[55] Filip A. Rasmussen and Kristian S. Thygesen. Computational 2d materials database: Electronic structure of transition-metal dichalcogenides and oxides. *J. Phys. Chem. C*, 119(23):13169–13183, 2015.

[56] Cheng Gong, Hengji Zhang, Weihua Wang, Luigi Colombo, Robert M. Wallace, and Kyeongjae Cho. Band alignment of two-dimensional transition metal dichalcogenides: Application in tunnel field effect transistors. *Applied Physics Letters*, 103(5), 2013.

[57] Jun Kang, Sefaattin Tongay, Jian Zhou, Jingbo Li, and Junqiao Wu. Band offsets and heterostructures of two-dimensional semiconductors. *Applied Physics Letters*, 102(1), 2013.

[58] Lei Fu, Yangyong Sun, Nian Wu, Rafael G. Mendes, Linfeng Chen, Zhen Xu, Tao Zhang, Mark H. Rmmeli, Bernd Rellinghaus, Darius Pohl, Lin Zhuang, and Lei Fu. Direct growth of MoS_2/h-BN heterostructures via a sulfide-resistant alloy. *ACS Nano*, 10(2):2063–2070, 2016.

[59] Gwan-Hyoung Lee, Young-Jun Yu, Xu Cui, Nicholas Petrone, Chul-Ho Lee, Min Sup Choi, Dae-Yeong Lee, Changgu Lee, Won Jong Yoo, Kenji Watanabe, Takashi Taniguchi, Colin Nuckolls, Philip Kim, and James Hone. Flexible and transparent MoS_2 field-effect transistors on hexagonal boron nitride-graphene heterostructures. *ACS nano*, 7(9):7931–7936, 2013.

[60] Chul-Ho Lee, Gwan-Hyoung Lee, Arend M. van der Zande, Wenchao Chen, Yilei Li, Minyong Han, Xu Cui, Ghidewon Arefe, Colin Nuckolls, Tony F. Heinz, Jing Guo, James Hone, and Philip Kim. Atomically thin pn junctions with van der waals heterointerfaces. *Nat Nano*, 9(9):676–681, 2014.

[61] Radhakrishnan Balu, Xiaoliang Zhong, Ravindra Pandey, and Shashi P. Karna. Effect of electric field on the band structure of graphene/boron nitride and boron nitride/boron nitride bilayers. *Applied Physics Letters*, 100(5):052104, 2012.

[62] Jie Su, Li-ping Feng, Hai-xi Pan, Hong-cheng Lu, and Zheng-tang Liu. Modulating the electronic properties of monolayer MoS_2 through heterostructure with monolayer gray arsenic. *Materials & Design*, 96:257–262, 2016.

[63] Le Huang, Nengjie Huo, Yan Li, Hui Chen, Juehan Yang, Zhongming Wei, Jingbo Li, and Shu-Shen Li. Electric-field tunable band offsets in black phosphorus and MoS_2 van der waals p-n heterostructure. *J. Phys. Chem. Lett.*, 6(13):2483–2488, 2015.

[64] Krzysztof Kośmider and Joaquín Fernández-Rossier. Electronic properties of the MoS_2-WS_2 heterojunction. *Phys. Rev. B*, 87(7):075451, 2013.

[65] Marco Bernardi, Maurizia Palummo, and Jeffrey C Grossman. Extraordinary sunlight absorption and one nanometer thick photovoltaics using two-dimensional monolayer materials. *Nano letters*, 13(8):3664–3670, 2013.

[66] M. O. Li, D. Esseni, J. J. Nahas, D. Jena, and H. G. Xing. Two-dimensional heterojunction interlayer tunneling field effect transistors (thin-TFETs). *IEEE Journal of the Electron Devices Society*, 3(3):200–207, 2015.

[67] R Schlaf, O Lang, C Pettenkofer, and W Jaegermann. Band lineup of layered semiconductor heterointerfaces prepared by van der waals epitaxy: Charge transfer correction term for the electron affinity rule. *Journal of applied physics*, 85(5):2732–2753, 1999.

[68] Rusen Yan, Sara Fathipour, Yimo Han, Bo Song, Shudong Xiao, Mingda Li, Nan Ma, Vladimir Protasenko, David A Muller, Debdeep Jena, et al. Esaki diodes in van der waals heterojunctions with broken-gap energy band alignment. *Nano letters*, 15(9):5791–5798, 2015.

[69] L Britnell, RV Gorbachev, R Jalil, BD Belle, F Schedin, A Mishchenko, T Georgiou, MI Katsnelson, L Eaves, SV Morozov, et al. Field-effect tunneling transistor based on vertical graphene heterostructures. *Science*, 335(6071):947–950, 2012.

[70] Thanasis Georgiou, Rashid Jalil, Branson D Belle, Liam Britnell, Roman V Gorbachev, Sergey V Morozov, Yong-Jin Kim, Ali Gholinia, Sarah J Haigh, Oleg Makarovsky, et al. Vertical field-effect transistor based on graphene-WS_2 heterostructures for flexible and transparent electronics. *Nature nanotechnology*, 8(2):100–103, 2013.

[71] Humberto Terrones, Florentino López-Urías, and Mauricio Terrones. Novel heterolayered materials with tunable direct band gaps by sandwiching different metal disulfides and diselenides. *Scientific reports*, 3, 2013.

[72] Mahdi Ghorbani-Asl, Paul D Bristowe, K Koziol, Thomas Heine, and Agnieszka Kuc. Effect of compression on the electronic, optical and transport properties of MoS_2/graphene-based junctions. *2D Materials*, 3(2):025018, 2016.

[73] Wei Hu, Tian Wang, Ruiqi Zhang, and Jinlong Yang. Effects of interlayer coupling and electric fields on the electronic structures of graphene and MoS_2 heterobilayers. *Journal of Materials Chemistry C*, 4(9):1776–1781, 2016.

[74] Lili Yu, Yi-Hsien Lee, Xi Ling, Elton J. G. Santos, Yong Cheol Shin, Yuxuan Lin, Madan Dubey, Efthimios Kaxiras, Jing Kong, Han Wang, and Toms Palacios. Graphene/MoS_2 hybrid technology for large-scale two-dimensional electronics. *Nano Letters*, 14(6):3055–3063, 2014.

[75] Tribhuwan Pandey, Avinash P Nayak, Jin Liu, Samuel T Moran, Joon-Seok Kim, Lain-Jong Li, Jung-Fu Lin, Deji Akinwande, and Abhishek K Singh. Pressure-induced charge transfer doping of monolayer graphene/MoS_2 heterostructure. *Small*, 12(30):4063–4069, 2016.

[76] Wencan Jin, Po-Chun Yeh, Nader Zaki, Daniel Chenet, Ghidewon Arefe, Yufeng Hao, Alessandro Sala, Tevfik Onur Mentes, Jerry I Dadap, Andrea Locatelli, et al. Tuning the electronic structure of monolayer graphene/MoS_2 van der waals heterostructures via interlayer twist. *Physical Review B*, 92(20):201409, 2015.

[77] Jianping Shi, Mengxi Liu, Jinxiu Wen, Xibiao Ren, Xiebo Zhou, Qingqing Ji, Donglin Ma, Yu Zhang, Chuanhong Jin, Huanjun Chen, et al. All chemical vapor deposition synthesis and intrinsic bandgap observation of MoS_2/graphene heterostructures. *Advanced Materials*, 27(44):7086–7092, 2015.

[78] Abbas Ebnonnasir, Badri Narayanan, Suneel Kodambaka, and Cristian V Ciobanu. Tunable MoS_2 bandgap in MoS_2-graphene heterostructures. *Applied Physics Letters*, 105(3):031603, 2014.

[79] Xingen Liu and Zhongyao Li. Electric field and strain effect on graphene-MoS_2 hybrid structure: Ab initio calculations. *The Journal of Physical Chemistry Letters*, 6(16):3269–3275, 2015.

[80] Yu-Chuan Lin, Jun Li, Sergio C. de la Barrera, Sarah M. Eichfeld, Yifan Nie, Rafik Addou, Patrick C. Mende, Robert M. Wallace, Kyeongjae Cho, Randall M. Feenstra, and Joshua A. Robinson. Tuning electronic transport in epitaxial graphene-based van der waals heterostructures. *Nanoscale*, 8:8947–8954, 2016.

[81] Yuan Liu, Hao Wu, Hung-Chieh Cheng, Sen Yang, Enbo Zhu, Qiyuan He, Mengning Ding, Dehui Li, Jian Guo, Nathan O. Weiss, Yu Huang, and Xiangfeng Duan. Toward barrier free contact to molybdenum disulfide using graphene electrodes. *Nano Letters*, 15(5):3030–3034, 2015.

[82] Dongri Qiu and Eun Kyu Kim. Electrically Tunable and Negative Schottky Barriers in Multi-layered Graphene/MoS_2 Heterostructured Transistors. *Scientific Reports*, 5:13743, sep 2015.

[83] Chandra Sekhar Rout, Padmashree D. Joshi, Ranjit V. Kashid, Dilip S. Joag, Mahendra A. More, Adam J. Simbeck, Morris Washington, Saroj K. Nayak, and Dattatray J. Late. Enhanced field emission properties of doped graphene nanosheets with layered SnS_2. *Applied Physics Letters*, 105(4), 2014.

[84] Adrien Allain, Jiahao Kang, Kaustav Banerjee, and Andras Kis. Electrical contacts to two-dimensional semiconductors. *Nat Mater*, 14(12):1195–1205, dec 2015.

[85] K. Zhou, D. Wickramaratne, S. Ge, S. Su, A. De, and R. K. Lake. Interlayer resistance of misoriented MoS_2. *arXiv*, 2016.

[86] Christof Gaiser, Thorsten Zandt, Alica Krapf, Ralf Serverin, Christoph Janowitz, and Recardo Manzke. Band-gap engineering with HfS_xSe_{2-x}. *Physical Review B*, 69(7):075205, 2004.

[87] Daniel S Koda, Friedhelm Bechstedt, Marcelo Marques, and Lara K Teles. Coincidence lattices of 2d crystals: Heterostructure predictions and applications. *The Journal of Physical Chemistry C*, 120(20):10895–10908, 2016.

[88] Ruoyu Yue, Adam T Barton, Hui Zhu, Angelica Azcatl, Luis F Pena, Jian Wang, Xin Peng, Ning Lu, Lanxia Cheng, Rafik Addou, et al. $HfSe_2$ thin films: 2d transition metal dichalcogenides grown by molecular beam epitaxy. *ACS nano*, 9(1):474–480, 2014.

[89] Shijie Wen, Hui Pan, and Yuebing Zheng. Electronic properties of tin dichalcogenide monolayers and effects of hydrogenation and tension. *Journal of Materials Chemistry C*, 3(15):3714–3721, 2015.

[90] Graeme Henkelman, Andri Arnaldsson, and Hannes Jónsson. A fast and robust algorithm for bader decomposition of charge density. *Computational Materials Science*, 36(3):354–360, 2006.

[91] Nathaniel Gillgren, Darshana Wickramaratne, Yanmeng Shi, Tim Espiritu, Jiawei Yang, Jin Hu, Jiang Wei, Xue Liu, Zhiqiang Mao, Kenji Watanabe, Takashi Taniguchi, Marc Bockrath, Yafis Barlas, Roger K Lake, and Chun Ning Lau. Gate tunable quantum oscillations in air-stable and high mobility few-layer phosphorene heterostructures. *2D Materials*, 2(1):011001, 2015.

[92] A. H. Castro Neto, F. Guinea, N. M. R. Peres, K. S. Novoselov, and A. K. Geim. The electronic properties of graphene. *Rev. Mod. Phys.*, 81:109–162, Jan 2009.

[93] Rajesh Kappera, Damien Voiry, Sibel Ebru Yalcin, Brittany Branch, Gautam Gupta, Aditya D Mohite, and Manish Chhowalla. Phase-engineered low-resistance contacts for ultrathin MoS_2 transistors. *Nature materials*, 13(12):1128–1134, 2014.

[94] J. C. Lin, S. Y. Yu, and S. E. Mohney. Characterization of low-resistance ohmic contacts to n- and p-type InGaAs. *Journal of Applied Physics*, 114(4), 2013.

[95] JE Padilha, A Fazzio, and Antônio JR da Silva. van der waals heterostructure of phosphorene and graphene: tuning the schottky barrier and doping by electrostatic gating. *Physical review letters*, 114(6):066803, 2015.

[96] Yeqing Lu, Guangle Zhou, Rui Li, Qingmin Liu, Qin Zhang, Timothy Vasen, Soo Doo Chae, Thomas Kosel, Mark Wistey, Huili Xing, et al. Performance of algasb/inas tfets with gate electric field and tunneling direction aligned. *IEEE Electron Device Letters*, 33(5):655–657, 2012.

[97] Houlong L Zhuang and Richard G Hennig. Computational search for single-layer transition-metal dichalcogenide photocatalysts. *The Journal of Physical Chemistry C*, 117(40):20440–20445, 2013.

[98] Yu-Ming Lin, Damon B Farmer, Keith A Jenkins, Yanqing Wu, Joseph L Tedesco, Rachael L Myers-Ward, Charles R Eddy, D Kurt Gaskill, Christos Dimitrakopoulos, and Phaedon Avouris. Enhanced performance in epitaxial graphene fets with optimized channel morphology. *IEEE Electron Device Letters*, 32(10):1343–1345, 2011.

[99] D. J. Thouless, M. Kohmoto, M. P. Nightingale, and M. den Nijs. Quantized hall conductance in a two-dimensional periodic potential. *Phys. Rev. Lett.*, 49:405–408, Aug 1982.

[100] F. D. M. Haldane. Model for a quantum hall effect without landau levels: Condensed-matter realization of the "parity anomaly". *Phys. Rev. Lett.*, 61:2015–2018, Oct 1988.

[101] Chao-Xing Liu, Xiao-Liang Qi, Xi Dai, Zhong Fang, and Shou-Cheng Zhang. Quantum anomalous hall effect in $hg_{1-y}mn_yTe$ quantum wells. *Phys. Rev. Lett.*, 101:146802, Oct 2008.

[102] Congjun Wu. Orbital analogue of the quantum anomalous hall effect in p-band systems. *Phys. Rev. Lett.*, 101:186807, Oct 2008.

[103] Masaru Onoda and Naoto Nagaosa. Quantized anomalous hall effect in two-dimensional ferromagnets: quantum hall effect in metals. *Physical review letters*, 90(20):206601, 2003.

[104] Rui Yu, Wei Zhang, Hai-Jun Zhang, Shou-Cheng Zhang, Xi Dai, and Zhong Fang. Quantized anomalous hall effect in magnetic topological insulators. *Science*, 329(5987):61–64, 2010.

[105] Hua Jiang, Zhenhua Qiao, Haiwen Liu, and Qian Niu. Quantum anomalous hall effect with tunable chern number in magnetic topological insulator film. *Phys. Rev. B*, 85(4):045445, 2012.

[106] Zhenhua Qiao, Shengyuan A. Yang, Wanxiang Feng, Wang-Kong Tse, Jun Ding, Yugui Yao, Jian Wang, and Qian Niu. Quantum anomalous hall effect in graphene from rashba and exchange effects. *Phys. Rev. B*, 82(16):161414, 2010.

[107] Zhenhua Qiao, Hua Jiang, Xiao Li, Yugui Yao, and Qian Niu. Microscopic theory of quantum anomalous hall effect in graphene. *Phys. Rev. B*, 85:115439, Mar 2012.

[108] M. Z. Hasan and C. L. Kane. *Colloquium* : Topological insulators. *Rev. Mod. Phys.*, 82:3045–3067, Nov 2010.

[109] Xufeng Kou, Shih-Ting Guo, Yabin Fan, Lei Pan, Murong Lang, Ying Jiang, Qiming Shao, Tianxiao Nie, Koichi Murata, Jianshi Tang, Yong Wang, Liang He, Ting-Kuo Lee, Wei-Li Lee, and Kang L. Wang. Scale-invariant quantum anomalous hall effect in magnetic topological insulators beyond the two-dimensional limit. *Phys. Rev. Lett.*, 113(13):137201, 2014.

[110] Zhiyong Wang, Chi Tang, Raymond Sachs, Yafis Barlas, and Jing Shi. Proximity-induced ferromagnetism in graphene revealed by the anomalous hall effect. *Phys. Rev. Lett.*, 114:016603, Jan 2015.

[111] Zhenhua Qiao, Wei Ren, Hua Chen, L. Bellaiche, Zhenyu Zhang, A.H. MacDonald, and Qian Niu. Quantum anomalous hall effect in graphene proximity coupled to an antiferromagnetic insulator. *Phys. Rev. Lett.*, 112(11):116404, 2014.

[112] H. X. Yang, A. Hallal, D. Terrade, X. Waintal, S. Roche, and M. Chshiev. Proximity effects induced in graphene by magnetic insulators: First-principles calculations on spin filtering and exchange-splitting gaps. *Phys. Rev. Lett.*, 110(4):046603, 2013.

[113] Jingshan Qi, Xiao Li, Qian Niu, and Ji Feng. Giant and tunable valley degeneracy splitting in MoTe2. *arXiv:1504.04434 [cond-mat]*, 2015.

[114] Yafei Ren, Xinzhou Deng, Changsheng Li, Jeil Jung, Changgan Zeng, Zhenyu Zhang, Qian Niu, and Zhenhua Qiao. Single-valley engineering in graphene superlattices. *arXiv:1501.05553 [cond-mat]*, 2015.

[115] N. J. C. Ingle and I. S. Elfimov. Influence of epitaxial strain on the ferromagnetic semiconductor EuO: First-principles calculations. *Phys. Rev. B*, 77(12):121202, 2008.

[116] Jayakumar Balakrishnan, Gavin Kok Wai Koon, Manu Jaiswal, A. H. Castro Neto, and Barbaros zyilmaz. Colossal enhancement of spin-orbit coupling in weakly hydrogenated graphene. *Nat Phys*, 9(5):284–287, 2013.

[117] Naoto Nagaosa, Jairo Sinova, Shigeki Onoda, A. H. MacDonald, and N. P. Ong. Anomalous hall effect. *Rev. Mod. Phys.*, 82(2):1539–1592, 2010.